

ELETTRA HIGHLIGHTS > 04 - 05

2010-10-15







E L E T T R A H I G H L I G H T S > 0 4 - 0 5

2010-1015



ELETTRA HIGHLIGHTS 2004-2005
EDITORIAL COMMITTEE

- > Fulvio Billè
- > Daniele Bulfone
- > Silvia Di Fonzo
- > Stefano Deiuri
- > Andrea Goldoni
- > Adriana Pertosi
- > Letizia Pierandrei
- > Regina Rochow

Cover Picture:

Researchers Marco Matteucci (left) and Filippo Romanato (right)
working in the LILIT clean room - picture by M. Marin

Graphic Design:

Studio Link (www.studio-link.it)

Print:

Graphart s.n.c.

This past year has seen a radical improvement in the future outlook of ELETTRA, with the funding of the new FEL source FERMI@ELETTRA and the full funding of the basic recurrent costs for the time being.

These improvements are due to the recognized quality of the service offered by ELETTRA to the international community, which has, in turn, convinced our national and regional Governments of the opportunity to continue and strengthen our contribution to the growth of the European Research Area.

The visits by Minister Letizia Moratti and EU Commissioner Potočnik as well as the previous visit of commissioner Busquin have allowed us to describe in detail how a national initiative can be of international relevance, like ELETTRA, which has been started with the specific mission to open bridges and networks with researchers of other Countries. And how this is accomplished by continuously aiming at the best quality involving our Advisory bodies. These elements have also been at the base of the interest by the European Investment Bank in supporting FERMI. Another strong base for the visibility of ELETTRA at European level is the management of the “I3” access program of the EU in all Synchrotron and FEL facilities in Europe and its participation in several EU funded projects also in the field of e-Science and ICT.

The new perspective opens new commitments: the detailed design and construction of FERMI must be even more open to the contributions of the potential users from Europe and other Countries, the management of ELETTRA must be capable of increasing the support of the growth of Research in Italy as well as in the other Partner Countries, and an increased capability is required in service and technology transfer to industry. The positive results of our Industrial Liaison Office, with the rapid increase of sales of scientific services and scientific instruments, are very encouraging in this respect.

ELETTRA has undergone a strong change of perspective also in its outlook and outreach to Society in general, and we are integrating the traditional scientific and financial accounting with more extended social-returns accounting. This is the base for a more extended and ambitious action, which is taking place within the European Forum for Research Infrastructures, to develop an overall European infrastructure for Research, spanning from Physics to Human Sciences, of which ELETTRA could be a strong example.

And back to the main challenge: build a Europe where Research is recognized and supported for its intrinsic cultural value.

Carlo Rizzuto
President

RESEARCH HIGHLIGHTS	11
Magnetic Properties and Electronic Structures	13
> The Co ligand field: A key parameter in photomagnetic CoFe Prussian blue derivatives	14
> Interface magnetism probed by X-ray magnetometry of marker impurities: Fe/GaAs(001)-4x6	17
> Spin-flop ordering from frustrated ferro- and antiferromagnetic interactions: a combined theoretical and experimental study of a Mn/Fe(100) monolayer	20
> Observation of the spin-orbit activated interchannel coupling in the 3d photoionization of cesium atoms	23
> Emission-depth-selective Auger photoelectron coincidence spectroscopy	27
Surface and Interface Science	31
> Selectivity of Auger decays to the local surface environment	32
> Tuning surface reactivity via quantum electron confinement	35
> Self-assembly of peptide nucleic acids on gold surfaces and its use as DNA affinity biosensors	38
Nanostructures	43
> Transition from 1D to 3D behavior induced by lithium doping in single wall carbon nanotubes	44
> Bottom-up fabrication of carbon-rich silicon carbide nanowires by manipulation of nanometer-size ethanol menisci	48
> Nanografting as a tool for the fabrication of nano-biosensors and the study of biomolecules in constrained geometries	51
Material Science	55
> Fibrillar deformation in mineralized tendon	56
> Self-assembled highly-ordered mesostructured hybrid films	60
> Periodically ordered mesoporous films composed of nanocrystalline multimetallic oxides	64
Structural Biology	69
> X-ray structure of the C-terminal domain of human insulin-like growth factor binding protein-1	70
> The structure of carbonoxy neuroglobin: a novel mechanism for control in ligand affinity	73
> Crystal structure of the complex between pectin methylesterase and its inhibitor protein	76
> N ² -substituted-0 ⁶ -cyclohexylmethylguanine derivatives: potent inhibitors of CDKs 1 and 2	79

MACHINE AND PHOTON SOURCE DEVELOPMENTS

83

- > ELETTRA status and prospects 84
- > Longitudinal beam dynamics with microbunching instability in the Fermi linac 88
- > The Radio Frequency (RF) upgrade project 92
- > Towards the stabilization of the ELETTRA storage-ring free-electron laser 95

INSTRUMENTATION & TECHNOLOGY

99

- > A new device for bimorph mirrors technology: The SY900S/A1902BS Bipolar High Voltage Power Supply System 100
- > The ELETTRA Virtual Collaboratory: The evolution of a Virtual Laboratory Software 104
- > Novel instrument for synchrotron light application 108

PROJECTS

111

- > Science with FERMI@ELETTRA: an EUV soft X-ray Free Electron Laser 112
- > Coordination of European science: The I3 Project and the I3 Network 117
- > Theory@ELETTRA 118

FACTS & FIGURES

125

- > ELETTRA beamline status 126
- > ELETTRA layout 127
- > Resources allocated at ELETTRA 128
- > ELETTRA staff 129
- > Statistics of performed measurements 130
- > Statistics of the Industrial Liaison Office 131

EVENTS

133

- > Explora and others - Science TV at ELETTRA 134
- > Photo gallery
 - Visit Moratti* 137
 - Italian - Australian Workshop* 139
 - Visit Potočnik* 140
 - Grid Project* 142
 - IAEA Affiliation Ceremony* 143
 - Accelerator Physics Course* 144



RESEARCH HIGHLIGHTS

MAGNETIC PROPERTIES AND ELECTRONIC STRUCTURES

Electronic structure and magnetism are at the origin of the most relevant functional and fundamental properties in all classes of materials. Advanced and powerful instrumentation on several beamlines at ELETTRA is dedicated to their investigation. Experiments carried out in the last year yielded to novel findings over a very wide range of applications, covering a variety of subjects on material science, nanostructures, surface physics, and solid state chemistry, and extending to basic aspects of the interaction between radiation and matter. The reports that follow highlight a selection of these results.

The first contribution describes the electronic states of metal cations in Prussian blue derivatives with interesting photomagnetic properties. X-ray absorption provides an understanding of their local electronic configuration and relates unusually small crystal field parameters derived from the measurements to the geometry of the atomic sites. Two contributions elucidate the role of chemical and exchange interactions at interfaces in magnetic film structures, constituting typical functional elements of spintronic devices. The elemental selectivity of circular magnetic dichroism is exploited, by using cobalt atoms as local markers, to obtain the layer-resolved magnetic profile of the interface between iron and gallium arsenide. In an other important class of interfaces, such as those formed by antiferromagnetic and ferromagnetic materials, linear and circular magnetic dichroism identify a particular non-collinear magnetic structure emerging from frustrated exchange interactions. The last two contributions describe fundamental aspects of the photoemission from atoms and solids. Total ion yield and partial cross sections above the 3d threshold reveal the role of spin-orbit activated interchannel coupling in the photoionization of atomic cesium. The technical development of coincidence spectroscopy, driven by the availability of intense radiation sources, leads to a detailed analysis of the inelastic scattering processes following core level photoexcitations in solids.

Carlo Carbone

THE Co LIGAND FIELD: A KEY PARAMETER IN PHOTOMAGNETIC CoFe PRUSSIAN BLUE DERIVATIVES

> V. Escax, G. Champion, C. Cartier dit Moulin, A. Bleuzen

Laboratoire de Chimie Inorganique et Matériaux Moléculaires, UMR CNRS 7071, Université Pierre et Marie Curie, Bât. F, 4, place Jussieu, 75252 Paris Cedex 05, FRANCE

> M.A. Arrio

Laboratoire de Minéralogie Cristallographie, UMR CNRS 7590-IPGP, Universités Paris 6 et 7, 4, place Jussieu, 75252 Paris Cedex 05, FRANCE

> M. Zacchigna, M. Zangrando, F. Bondino

TASC Laboratory, CNR-INFN, Beamline BACH, S.S. 14 km 163.5, in AREA Science Park, 34012 Trieste, ITALY

Spectacular and numerous properties in the fields of electrochemistry, magnetism or photomagnetism have been recently revealed in Prussian blue and analogues [1]. The general formula is $A^{II}_3[B^{III}(CN)_6]_2 \cdot nH_2O$ where A and B are transition metal cations. It is a lacunary structure where the $[B(CN)_6]$ vacancies are filled by water molecules, coordinated to the A^{II} cation. The presence of an excess of alkali cation during the synthesis leads to a perfect face cubic centered (fcc) structure $X^I A^{II}[B^{III}(CN)_6]$ in which the X^I alkaline cation occupies half of the interstitial tetrahedral sites. In intermediate cases, the divalent cation occupies all the fcc sites whereas the occupation of the octahedral sites by the hexacyanometalate varies as a function of the amount of alkali

cation inserted in the structure. In one unit cell, the number of divalent cation is then always four and the number of hexacyanometalate and alkali cation are equal to $(8+x)/3$ and x respectively, due to the electroneutrality of the solid. The formulas will be given as $X^I_x A^{II}_4 [B^{III}(CN)_6]_{(8+x)/3}$.

We are engaged in the synthesis of new photomagnetic Prussian Blue compounds, bimetallic complexes with fcc structure. For some of iron-cobalt analogues, the magnetization increases strongly after irradiation with visible light at low temperature ($T < 20$ K). Our goal is the understanding of the origin of this phenomenon to create new objects with controlled properties.

We synthesized the CoFe Prussian Blue analogue $Rb_{1.8}Co_4[Fe(CN)_6]_{3.30} \cdot 13H_2O$ ($Rb_{1.8}CoFe$)

Figure 1. Representation of the unit cell of the $Rb_{1.8}Co_4[Fe(CN)_6]_{3.30} \cdot 13H_2O$ compound.

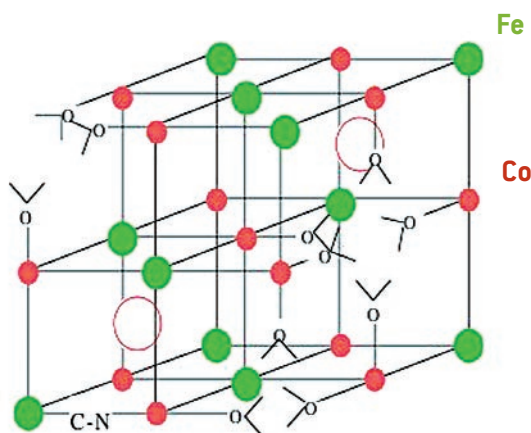


(Figure 1). Such compound displays spectacular photomagnetic effects due to a light-induced $\text{Co}^{\text{III}}(\text{Low Spin}, S=0)\text{-Fe}^{\text{II}}(S=0) \rightarrow (\text{Co}^{\text{II}}(\text{High Spin}, S=3/2)\text{-Fe}^{\text{III}}(S=1/2))^*$ electron transfer accompanied by a spin change of Co and a lengthening of the Co to ligand bonds from 1.91 Å for $\text{Co}^{\text{III}}(\text{LS})$ to 2.08 Å for $\text{Co}^{\text{II}}(\text{HS})$ [2]. It has been commonly proposed that the stabilization of the $\text{Co}^{\text{III}}(\text{LS})\text{-Fe}^{\text{II}}$ switchable pairs is correlated with the average amount of $-\text{NC}$ ligands in the Co coordination sphere. The average chemical composition of the Co coordination polyhedron is given by $\text{Co}(\text{NC})_{(8+x)/2}(\text{OH}_2)_{(4-x)/2}$. When x increases (the quantity of inserted alkali cation), $-\text{OH}_2$ weak field ligands are replaced by $-\text{NC}$ stronger ones in the Co coordination sphere. An increase of the amount of $-\text{NC}$ ligands in the Co coordination sphere should then lead to an increase of the Co ligand field and of the reducing power of Co, and then to the stabilization the $\text{Co}^{\text{III}}(\text{Low Spin})\text{-Fe}^{\text{II}}$ photoactive diamagnetic pairs. Thus, the photomagnetic properties are supposed to be linked to the Co crystal field parameter $10Dq(\text{Co})$.

To show the relation between photomagnetic properties and Co crystal field parameter, two Prussian Blue analogues in which the Co coordination sphere is different were chosen. In $\text{Co}^{\text{II}}_4[\text{Fe}^{\text{III}}(\text{CN})_6]_{2.7} \cdot 18\text{H}_2\text{O}$ (1) (No photomagnetic effect) and in $\text{Rb}_{1.8}\text{Co}^{\text{III}}_{3.3}\text{Co}^{\text{II}}_{0.7}[\text{Fe}^{\text{II}}(\text{CN})_6]_{3.3} \cdot 13\text{H}_2\text{O}$ (2), the average chemical composition of the Co coordination sphere and the cell parameter are respectively $\text{Co}(\text{NC})_4(\text{OH}_2)_2$ (10.32 ± 0.05 Å) and $\text{Co}(\text{NC})_5(\text{OH}_2)$ (9.96 ± 0.05 Å). Since a quantitative UV-Visible spectroscopic investigation is impossible due to the existence of large intervalence bands, we used X-ray absorption spectroscopy to determine the $10Dq(\text{Co})$ values [3].

X-ray absorption spectra of 1 and 2 were recorded at the Co-L₃ edge and compared to the spectrum of $[\text{Co}(\text{OH}_2)_6]^{2+}$ (Figure 2). L_{2,3} edges of 3d transition metals involve symmetry allowed electric dipole transitions from 2p core electrons to incompletely filled 3d and 4s levels ($2p^64s^0 \rightarrow 2p^54s^1$ transitions can be neglected due to their low intensity relative to the $2p^63d^n \rightarrow 2p^53d^{n+1}$ ones). They consist of multiplet structures due to the $2p^53d^{n+1}$ configurations. The peaks A to

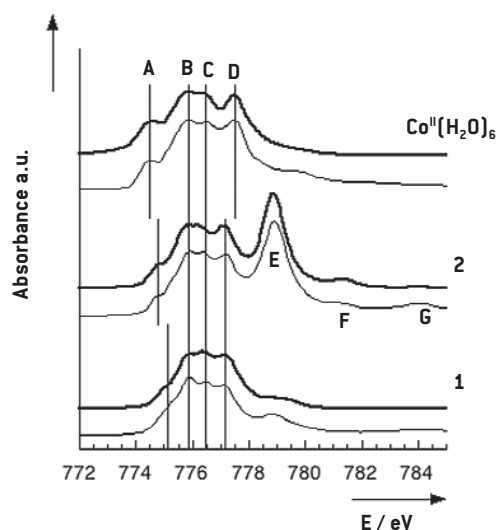
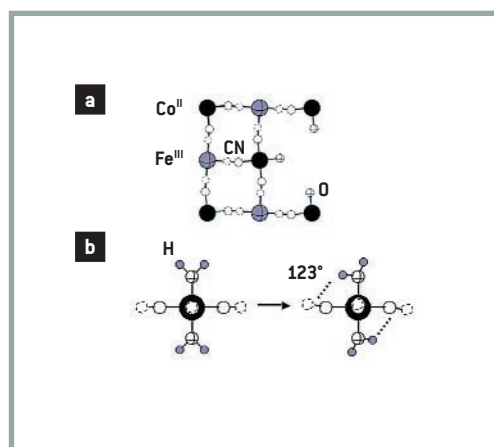


Figure 2. Experimental Co-L₃ edges [–], best simulations [—] performed in the Ligand Field Multiplet model for $[\text{Co}(\text{OH}_2)_6]^{2+}$, compounds 1 and 2.

D are characteristic of Co^{II} (high spin) in octahedral symmetry and the peaks E to G, at higher energy, of Co^{III} (low spin) [2]. The Co^{II} contribution (Features A to D) is different from one spectrum to the other. In order to extract quantitative information from L_{2,3} edges absorption spectra, we simulated experimental data performing calculations using the so-called Ligand Field Multiplet Theory. The approach takes into account all the electronic interactions, the spin-orbit coupling on any electronic open shell and treats the geometrical environment of the absorbing atom through crystal field potential. The best simulations (see Figure 2) indicate that the observed differences are due to different $10Dq(\text{Co}^{\text{II}})$ values. An increase of the energy gap between the peaks A and D of Co^{II} species corresponds to an increase of $10Dq(\text{Co}^{\text{II}})$. $10Dq(\text{Co}^{\text{II}})$ in $[\text{Co}^{\text{II}}(\text{OH}_2)_6]^{2+}$ (1 eV) is close to the one given by UV-Visible spectroscopy and $10Dq(\text{Co}^{\text{III}})$ in 2 (2.4 eV) is also the expected one for a Co^{III} (Low spin) surrounded by a majority of NC ligands, close to $10Dq(\text{Co}^{\text{III}})$ in $[\text{Co}^{\text{III}}(\text{NH}_3)_6]^{3+}$.

Surprisingly, $10Dq(\text{Co}^{\text{II}})$ in 1 (0.55 eV) and $10Dq(\text{Co}^{\text{II}})$ in 2 (0.7 eV) are extremely low compared with $10Dq(\text{Co}^{\text{II}})$ in $[\text{Co}(\text{OH}_2)_6]^{2+}$ or any $10Dq(\text{Co}^{\text{II}})$ value reported, to our knowledge, for octahedral $\text{Co}^{\text{II}}(\text{HS})$ coordination compounds. If only the nature of the ligands is considered, one expects a value close to $10Dq(\text{Co}^{\text{II}})$ in $[\text{Co}^{\text{II}}(\text{NH}_3)_6]^{2+}$ or $[\text{Co}^{\text{II}}(\text{en})_3]^{2+}$, around 1.3 ± 0.1 eV. We can explain these

Figure 3. Proposed scheme for **(a)** the 100 plane of one unit cell and **(b)** the Co^{II} coordination polyhedron using sensible structural parameters for compound **1**.



low $10Dq(\text{Co}^{\text{II}})$ values from structural considerations. They are due to the geometry of the Co^{II} coordination polyhedron imposed by the 3-dimensional network.

In **1**, the geometry of the Co^{II}-NC-Fe entities deviates from the linear most stable one. They are bent as represented for the 100 plane of one unit cell of **1** in Figure 3a, leading to a weaker orbital interaction between Co and NC and a weaker ligand field than expected. The geometry of the Co-OH₂ entities also deviate from the most stable one, leading again to the decrease of the ligand field exerted by OH₂. These deviations can be explained by the formation of hydrogen bonds between OH₂ bond to Co and the electronic density on the NC ligand

as schematized in Figure 3b. Due to these interactions, the OH₂ ligands swing around the O position and consequently, the orbital interaction between Co and OH₂ is weakened leading to a weak crystal field value. The structural model proposed to explain the $10Dq\text{Co}^{\text{II}}$ value in **2** can be found in reference [3].

This is the first experimental determination of Co crystal field parameters in photomagnetic CoFe Prussian Blue analogues using X-ray absorption spectroscopy. We show that, contrary to expectation, the Co^{II} crystal field parameter is, to our knowledge, weaker than for any octahedral Co^{II}(HS) molecular entities. The $10Dq$ value is essentially determined by the geometry of the Co coordination polyhedron rather than by the chemical nature of the ligands.

References

- [1] Verdaguer M. et al., *Coord. Chem. Rev.* **190-192**, 1023 (1999)
- [2] Cartier dit Moulin C., Villain F., Bleuzen A., Arrio M. A., Saintavit P., Lomenech C., Escax V., Baudalet F., Dartyge E., Gallet J.-J., Verdaguer M., *J. Amer. Chem. Soc.* **122**, 6653 (2000)
- [3] Escax V., Champion G., Arrio M.-A., Zacchigna M., Cartier dit Moulin C., Bleuzen A., *Angew. Chem. Int. Ed.* **44**, 2 (2005)

INTERFACE MAGNETISM PROBED BY X-RAY MAGNETOMETRY OF MARKER IMPURITIES: Fe/GaAs(001)-4x6

> **L. Giovanelli**

Laboratoire Matériaux et Microélectronique de Provence, UMR CNRS 6137, Univ. P. Cezanne, 13397 Cedex 20 Marseille, FRANCE

TASC Laboratory, CNR-INFN, S.S. 14 km 163.5, in AREA Science Park, 34012 Trieste, ITALY

> **G. Panaccione, J. Fujii, M. Fabrizio**

TASC Laboratory, CNR-INFN, S.S. 14 km 163.5, in AREA Science Park, 34012 Trieste, ITALY

> **G. Rossi**

TASC Laboratory, CNR-INFN, S.S. 14 km 163.5, in AREA Science Park, 34012 Trieste, ITALY

INFN- Dip. di Fisica Univ. di Modena e Reggio Emilia, Via A. Campi 213/A, 41100 Modena, ITALY

> **C.H. Back**

Institut für Exp. Physik, Univ. Regensburg, 93040 Regensburg, GERMANY

Probing magnetism at interfaces between materials with different transport properties is of central interest to understand phenomena like spin injection into semiconductors. The properties of interfaces between semi-infinite solids are, in general, quite different with respect to interfaces between substrates and submonolayer or ultra-thin films, both in terms of spin and orbital moments. In the case of continuity in two dimensions, thin films can be considered bulk like already for a relatively small number of layers and MBE growth may produce a realistic interface. Therefore, it is possible to study the interfacial magnetic properties of relevant systems for spintronics applications, like Fe/GaAs (001). The remaining problem is how to reach a detailed knowledge of the magnetic properties at the interface, i.e. where the extended electron wavefunctions match between the Fe and the GaAs and where therefore the spin and charge transport across the two media occur. The access to the information on buried interfaces can be obtained by using magnetic markers. Layer dependent analysis of magnetic films has been demonstrated by selectively depositing isotopes of Fe and Co during the magnetic film growth, by performing Mössbauer spectroscopy¹.

Here we show that a magnetic marker atom technique can be used for this system,

as well as for several related systems, by exploiting the atom specificity and magnetometric power of X-ray magnetic dichroism (XMCD). By exploiting the chemical sensitivity of XMCD it is therefore possible to measure the changes of magnetization of impurity atoms purposely dispersed at the interface between Fe and GaAs as well as within the Fe film at various depths from the interface. We have therefore prepared a double wedge structure of iron containing an oblique layer of $\text{Co}_{0.5}\text{Fe}_{0.5}$ (see Figure 1): the Co magnetic markers are embedded in the macroscopically magnetized Fe film, and their XMCD signal reflects the local magnetization of the Fe film that changes from the interface up to the surface with a characteristic profile. This allows obtaining a profile of the magnetization as a function of the distance from the interface to the bulk of the overlayer as well as from the bulk to the overlayer surface. Experiments were performed at the APE-INFN beamline, using GaAs(001)-(4x6) surfaces obtained in UHV by standard sputter/annealing treatments. A moveable shutter allowed to grow a first iron wedge of 6 atomic layers maximum thickness over a sample length of 6 mm along the [110] substrate direction. One mm of sample length was left uncovered. On this wedge, a single monolayer of $\text{Fe}_{0.5}\text{Co}_{0.5}$ was deposit-

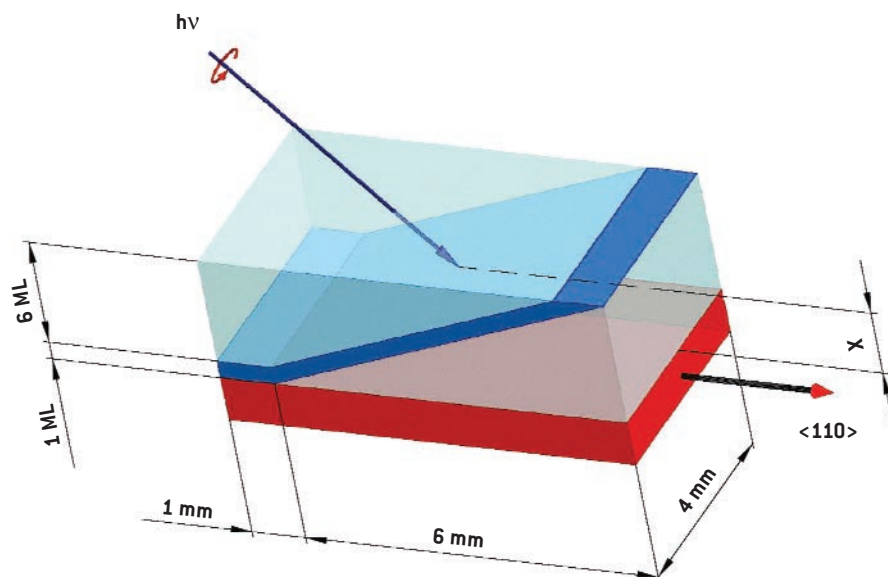


Figure 1. Sketch of the experimental geometry and of the double wedge as described in the text. The sample was magnetized in plane along the $[110]$ direction. The X-rays impinge parallel to the $[1-10]$ plane forming an angle of 45° with the sample magnetization. The distance from the interface is referred as $X(\text{ML})$. b) Kerr analysis results: on the left axis the Kerr intensity [saturation magnetization] is plotted as a function of thickness for the wedge samples (triangles for the Fe wedge, squares for the Fe wedge covered with the $\text{Fe}_{0.5}\text{Co}_{0.5}$ ML) and as a function of X for the double-wedge sample (filled circles).

ed by co-evaporation. Finally an opposite wedge of pure iron was grown obtaining a sample with Co atoms embedded at a variable distance (denoted in the figure as $X(\text{ML})$) from the interface in an evenly thick 6 ML Fe film. The magnetization was probed by the transverse magneto-optic Kerr effect (MOKE), *in situ*, at various positions along the easy magnetization axis with a lateral resolution of $300 \mu\text{m}$. In agreement with previous studies performed on Fe/GaAs(001)-(4x6), the FM state at RT sets in at about 3 ML and the remnant magnetization increases for increasing thickness. When 1 ML of $\text{Fe}_{0.5}\text{Co}_{0.5}$ is added to the first Fe wedge the thickness value for the onset of the FM state does not change. Consequently, the Kerr response at a given point of the sample is enhanced. Finally, the sample magnetization results to be constant across the whole sample in the case of the double-wedge sample. In agreement with previous result, we found islands of Fe to coalesce into a continuum film at a nominal thickness of 3 ML. At the same time the substrate atoms segregation was found to be uneven with Ga prevailing between 3 and 4.5 ML (probably due to the Ga-termina-

tion of the present reconstruction) while As becomes more abundant on the surface at higher coverage. The Fe coalescence was accompanied by the onset of magnetization as observed by MOKE³.

The XMCD Co $L_{2,3}$ spectra were measured with the sample placed at 45° incidence angle to the soft X-rays (see Figure 1) in total electron yield mode. Figure 2 displays three representative sets of polarization dependent XAS spectra, along with the XMCD spectra, corresponding to the Co atoms residing 4.6, 3.2 and 0.4 ML from the GaAs substrate. As it can be seen, all spectra display a net dichroic signal testifying that the film is magnetic even at the interface with the semiconductor. Making use of the X-ray magneto-optical sum rules, results show that in general the marker magnetic moments are large also at the interface, i.e. for Co atoms embedded in the iron atomic layer in the vicinity of the substrate, this rules out the presence of a magnetically dead or weakly ordered interface, in agreement with data from capped samples. Particularly, the spin moment is reduced both at the interface with GaAs and at the surface of the film². The measured magnetic profile

confirms: i) that the presence of Ga within the film does not quench the Fe magnetic moment ii) that the magnetic phase diagram of the thin Fe film on GaAs(001) depends critically on the small details of the Fe film chemical configuration, the key feature being the degree of hybridization between the Fe and As atoms.

On the opposite, the orbital moment increases in going towards the Fe/GaAs interface where it is sensibly higher than the reference values. This is better seen in the lowest panel of Figure 2 where the dichroic spectra have been normalized to the L_2 intensity. The Δ_3 intensity increases for Co markers closer to the interface, thus indicating that the orbital moment within the Fe film increases near the interface, in agreement with previous findings. The observed increase of the orbital moment can be a consequence of a variation in the anisotropy value, as observed in low dimensional systems showing perpendicular magnetic anisotropy. Finally, we would like to point out that the layer sensitive evaluation of the orbital moment might play a key role in explaining the phenomenon of UMA observed in these systems. In fact, one of the possible routes to explain this phenomenon is the anisotropic bonding of Fe atoms with the 2-fold symmetric substrate: since the crystalline anisotropy is driven by the anisotropy of the spin-orbit interaction, a possible orbital moment anisotropy induced by the anisotropic bonding with substrate atoms would confirm the hypothesis mentioned above. The observed increase of the orbital moment can be a consequence of such anisotropy as observed in low dimensional systems showing perpendicular magnetic anisotropy. Our results emphasize the importance of the chemical profile on the magnetic properties in this type of hetero-epitaxial systems. It is worth noting that the sensing-layer approach was the key issue to probe the magnetic properties along the Fe film thickness that results to be more reliable than a thickness dependent analysis as far as the interface properties are concerned. Moreover, the possibility of studying samples prepared in-situ circumvents the ambiguity introduced by the presence of a capping layer.

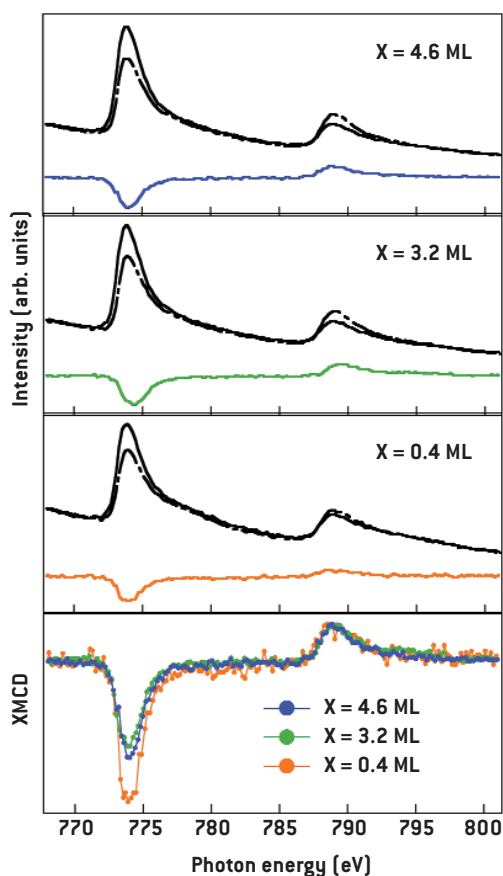


Figure 2. XMCD results. Upper panels: Co $L_{2,3}$ XMCD spectra for Co atoms lying at different distances (X) from the interface. The spectra have been normalized to the incident photon flux as measured on a calibrated photodiode. Lowest panel: the three representative dichroic spectra after normalization of the XMCD intensity at L_2 .

References

- [1] Liljequist D., Ismail M., Saneyoshi K., Debusmann K., Keune W., Brand R. A., and Kiauka W., *Phys. Rev. B* **31**, 4137 (1985) and refs therein
- [2] Giovanelli L., Fabrizioli M., Tian C.S., Gastelois P.L., Fujii J., Panaccione G., Rossi G. and Back C.H., *Applied Physic Letters* **87**, 1 (2005)
- [3] Giovanelli L., Fabrizioli M., Tian C.S., Gastelois P.L., Fujii J., Panaccione G., Rossi G. and Back C.H., *Phys. Rev. B* **72**, 045221 (2005)

SPIN-FLOP ORDERING FROM FRUSTRATED FERRO- AND ANTIFERROMAGNETIC INTERACTIONS: A COMBINED THEORETICAL AND EXPERIMENTAL STUDY OF A Mn/Fe(100) MONOLAYER

> **C. Grazioli, M. Veronese, S. Turchini, C. Carbone**

Istituto di Struttura della Materia, Consiglio Nazionale delle Ricerche, AREA Science Park, 34012 Trieste, ITALY

> **D. Alfè**

Department of Earth Sciences and Department of Physics and Astronomy, University College London, Gower Street, London WC1E 6BT, UK

CNR-INFM DEMOCRITOS National Simulation Center, Trieste, ITALY

> **S. R. Krishnakumar**

International Centre for Theoretical Physics, Strada Costiera 11, 34100 Trieste, ITALY

> **Nicola Bonini, Andrea Dal Corso, Stefano Baroni**

SISSA - Scuola Internazionale Superiore di Studi Avanzati, Via Beirut 2-4, 34014 Trieste, ITALY

CNR-INFM DEMOCRITOS National Simulation Center, Trieste, ITALY

> **Subhra Sen Gupta, D.D. Sarma**

Solid State and Structural Chemistry Unit, Indian Institute of Science, Bangalore 560 012, INDIA

The magnetic structure of ultrathin antiferromagnetic (AFM) overlayers on ferromagnetic (FM) substrates determines the properties of ferromagnetic and antiferromagnetic multilayers that are key constituents of devices such as exchange-bias or tunneling magnetoresistance recording systems. Complex, non-collinear, magnetic structures are expected at these interfaces, for spin canting minimizes the exchange energy between a ferromagnet and an antiferromagnet that exposes a plane with antiparallel spins. The resulting spin-flop alignment of the moments in the antiferromagnet, perpendicular to the magnetization in the ferromagnet, is the microscopic basis of the large coercive field in exchange-bias devices. In spite of the great interest in these systems, the understanding gained so far on the basis of semiempirical models has neither been validated by accurate first-principles calculations, nor by a direct experimental observation of the non-collinear magnetic order at the interface. In fact, on one hand, accurate, fully unconstrained methods based on density-functional theory (DFT) for studying non-collinear magnetic structures have

become available only recently [1]; on the other hand, the simultaneous access to both antiferromagnetic and ferromagnetic ordering, not possible by usual experimental methods, has become possible by magnetic circular and linear dichroism methods using advanced synchrotron sources.

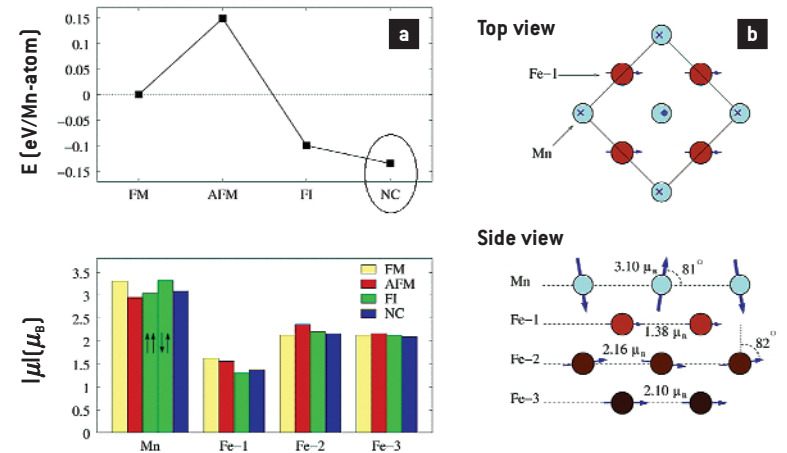
The aim of this work is to determine the magnetic structure of Mn deposited on Fe(100) in the mono-layer regime, using state-of-the-art theoretical and experimental techniques. Mn/Fe(100) has been simulated using fully unconstrained Spinor Density Functional Theory (SDFT) which allows for a proper account of non-collinear magnetic structures [1]. This same system has then been investigated experimentally by means of a combination of X-ray magnetic circular dichroism (XMCD) and X-ray magnetic linear dichroism (XMLD) spectroscopies, which allows for a direct assessment of ferromagnetic and antiferromagnetic ordering, and also for a determination of the moment orientations with chemical sensitivity.

Our SDFT calculations have been performed within the local density approximation and neglecting spin-orbit interactions.

The latter approximation makes the calculated magnetic structures degenerate with respect to an arbitrary overall rotation of the magnetization field. By constraining all the magnetic moments to be collinear a Mn overlayer on Fe can assume one of three distinct configurations: in the *ferromagnetic* (FM) structure all the Mn magnetic moments are parallel to each other and to the magnetization of the ferromagnetic iron substrate; in the second, *anti-ferromagnetic* (AFM), structure the Mn magnetic moments are antiparallel with respect to the substrate magnetization; the third, *ferrimagnetic* (FI), structure is finally characterized by an anti-ferromagnetic arrangement of atomic moments in the overlayer, which result alternately parallel or anti-parallel to the substrate magnetization. It is interesting to notice that the inequivalence of spin-up and spin-down atoms in the overlayer may determine some buckling in the surface.

When the constraint of spin collinearity is released, the frustration of the magnetic bonds across the interface drives a rotation of the Mn moments resulting in a chess-board arrangement where these moments form angles of $\sim 80^\circ$ with respect to those of the underlying Fe atoms. This non-collinear (NC) structure is depicted in Figure 1b. We note that, with such arrangement, the magnetic interactions between Mn and Fe are the same for all the Mn atoms, which are therefore all structurally equivalent. The almost perpendicular orientation of the Mn moments corresponds to a quasi-anti-ferromagnetic order in the Mn plane, still avoiding the magnetic frustration experienced in the collinear situations. We find that this NC structure is more stable by about 35 meV/atom than the FI collinear structure (see the top panel of Figure 1a), and should therefore be clearly observable also at room temperature.

Using XMCD and XMLD at the Mn- $L_{2,3}$ edges we examined the magnetic structure of sub-monolayer and monolayer (0.1-1.0 ML) Mn films deposited on Fe(100). The samples were grown *in situ* in the 10^{-10} mbar range using a quartz-crystal microbalance to control the thickness. As a first step, an Fe(100) surface was epitaxially grown on a clean and ordered Ag(100) single crystal surface and magnetized in remanence along the



Fe[001]. The thickness of the Fe film was above 50 ML in order to suppress Ag surface segregation. A wedge of Mn in the range of 0-1.1 ML was prepared. The experiments were performed at the 4.2 beamline “Circular Polarization”.

The magnetization of Mn was investigated by circular dichroism. The XMCD data measurements performed at different Mn thicknesses for the submonolayer regime (not shown here) are in accordance with Ref. 2. For less than 1 ML, we observe an XMCD effect of the Mn adlayer opposite to that of Fe, which is a proof of long-range ferromagnetic order of the adlayer aligned antiparallel to the magnetization in the Fe substrate. The net magnetization of Mn decreases with increasing thickness and approaches zero for 1 ML (Figure 2a), thus pointing out a rather smooth transition from ferro- to anti-ferromagnetic arrangement.

The XMLD was measured rotating the sample in the polar and azimuthal geometries. The spectra recorded for in-plane and for out-of-plane polarization (polar rotation) are shown in Figure 2b. The intensity ratio between the L_2 well defined double peak structures (labeled as P_I and P_{II}) turns out to be well suited to detect the spectral changes. The intensity ratios for two geometries, reported in Figure 2a and 2b, show that the polar measurement has a regular dependence as a function of the angle, while the azimuthal one is much less pronounced, which supports the idea that the orientation is perpendicular to the surface.

We have simulated the spectral lineshapes by exact diagonalization of an atomic many-

Figure 1. (a) Top panel: total energies of the FM, AFM, FI, and NC structures relative to the FM structure. Bottom panel: magnitude of the atomic magnetic moments in the various structures. For the FI structure $\uparrow\uparrow$ and $\uparrow\downarrow$ indicate the Mn atom with magnetic moment parallel and antiparallel to the underlying Fe atoms, respectively. **(b)** Schematic view of the Mn/Fe magnetic interface.

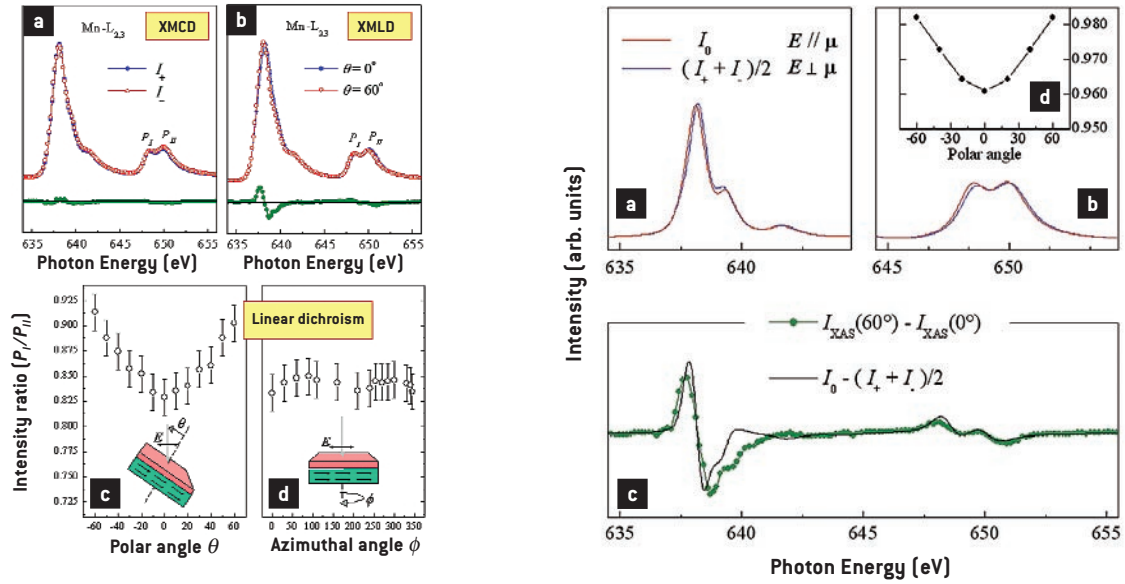


Figure 2. Top: **(a)** XMCD data at the $L_{2,3}$ edges for 1 ML of Mn; **(b)** Mn $L_{2,3}$ X-ray-absorption spectroscopy for 1 ML of Mn as a function of the angle between E and the surface normal. Bottom: XMLD effect for the polar **(c)** and for the azimuthal **(d)** rotations; the intensity ratio of the Mn- L_2 double peak structures is used to measure the intensity of the effect.

Figure 3. (a) and (b) Simulation of the absorption spectra for the two polarization directions after suitable broadening. **(c)** Comparison between the simulated and the experimental XMLD. **(d)** Simulated P_{\perp}/P_{\parallel} intensity ratio.

body Hamiltonian, based on a fully coherent spectral function given by:

$$I_q(\omega) = \sum_n \left| \sum_{v,c} \langle \Psi_f^n(N) | a_v^\dagger a_c | \Psi_g(N) \rangle \langle v | r C_q^{(1)} | c \rangle \right| \times \delta(\hbar\omega - [E_f^n(N) - E_g(N)])$$

The irreducible components of the dipole operator are defined as: $T_q^{(1)} = r C_q^{(1)}$, where $q=0, +1, -1$ correspond to z -linearly polarized, right circularly polarized and left circularly polarized light, respectively, and $C_q^{(1)}$ are normalized spherical harmonics [3].

In Figure 3a,b we show the results of the spectral simulations. By using different combinations of the irreducible components of the dipole operator $T_q^{(1)}$ we are able to simulate the Mn- $L_{2,3}$ spectra as a function of the orientation between the magnetic moment on Mn and \vec{E} : I_0 for $\vec{E} \parallel \vec{\mu}$ and $(I_+ + I_-)$ for $\vec{E} \perp \vec{\mu}$. In terms of the lineshape, the agreement with the experimental spectra of Figure 2b is very good. As shown in Figure 5c, the XMLD spectrum, which carries all information about the lineshape changes, is well reproduced by the simulated XMLD lineshape calculated as $I_0 - (I_+ + I_-)/2$. The calculated P_{\perp} and P_{\parallel} intensity ratio, assuming perpendicular orientation of the Mn moments with respect to the surface plane, also simulates the angular dependence of the

experimental results. We can conclude that the magnetic moments of Mn are aligned out of the surface plane, perpendicular to the Fe magnetization.

The non-collinear magnetism of the system intrinsically derives from the competing exchange interactions between the monolayer and the substrate moments. This mechanism may also lead to the development of similar spin-flop structures in other monolayer systems, where the exchange interaction within the antiferromagnetic monolayers prevails, but does not overwhelm, the coupling with the ferromagnetic substrate.

References

- [1] T. Oda, A. Pasquarello, and R. Car, *Physical Review Letters* **80**, 3622 (1998). R. Gebauer et al., *Physical Review B* **61**, 6145 (2000). D. Hobbs, G. Kresse, and J. Hafner, *Physical Review B* **62**, 11556 (2000)
- [2] O. Rader, W. Gudat, D. Schmitz, C. Carbone, and W. Eberhardt, *Physical Review B* **56**, 5053 (1997). J. Dresselhaus et al., *Physical Review B* **56**, 5461 (1997)
- [3] P. Mahadevan and D.D. Sarma, *Physical Review B* **61**, 7402 (2000); Subhra Sen Gupta, P. Mahadevan and D.D. Sarma (Unpublished results)

OBSERVATION OF THE SPIN-ORBIT ACTIVATED INTERCHANNEL COUPLING IN THE $3d$ PHOTOIONIZATION OF CESIUM ATOMS

> **H. Farrokhpour**

*Chemistry Department, Isfahan University of Technology, Isfahan 84154, IRAN
The Abdus Salam International Centre for Theoretical Physics, 34014 Trieste, ITALY*

> **M. Alagia**

*CNR - ISMN Sez. Roma1, P.le A. Moro 5, 00185 Roma, Italy
TASC Laboratory, CNR-INFN, Gas Phase Beamline@ELETTRA, AREA Science Park, 34012 Trieste, ITALY*

> **M. Ya Amusia**

*Racah Institute of Physics, The Hebrew University, Jerusalem 91904, ISRAEL
A.F. Ioffe Physical-Technical Institute, St. Petersburg 194021, RUSSIA*

> **L. Avaldi, M. Coreno**

*CNR - IMIP, Area della Ricerca di Roma, CP10, 00016 Monterotondo Scalo, ITALY
TASC Laboratory, CNR-INFN, Gas Phase Beamline@ELETTRA, AREA Science Park, 34012 Trieste, ITALY*

> **L.V. Chernysheva**

A.F. Ioffe Physical-Technical Institute, St. Petersburg 194021, RUSSIA

> **M. de Simone**

TASC Laboratory, CNR-INFN, Gas Phase Beamline@ELETTRA, AREA Science Park, 34012 Trieste, ITALY

> **R. Richter**

Sincrotrone Trieste, AREA Science Park, 34012 Trieste, ITALY

> **S. Stranges**

*Dipartimento di Chimica, Università di Roma "La Sapienza", 00185 Roma, ITALY
TASC Laboratory, CNR-INFN, Gas Phase Beamline@ELETTRA, AREA Science Park, 34012 Trieste, ITALY*

The $3d$ photo-absorption spectra of atoms and ions have attracted some interest because the high localization of the $4f$ electrons plays a key role in the determination of the electronic structure and magnetic properties of lanthanide and pre-lanthanide compounds. These studies mainly aimed at the characterization of the potential barrier effect of f electrons, which governs the relative strengths of discrete vs. continuum transitions. Both theoretical studies and experiments investigated the f wavefunction collapse due to the double-wells structure of the effective potential at the $4d$ or $3d$ thresholds. Although the general agreement of experiment and theory is good for the total ionization cross section, several important discrepancies between the calculated and measured partial ionization cross section of the $3d_{5/2}$ and $3d_{3/2}$ channels have been noticed in

the recent results on xenon of Kivimäki et al.[1]. Those differences have been accounted for by the recent calculations in the frame of the spin-polarized random phase approximation with exchange (SPRPAE) [2] and relativistic time-dependent density functional (RTDDFT) [3] theories, which included spin-orbit activated inter-channel coupling. This is an interesting phenomenon because it is a pure manybody effect, with no single particle analog. While other effects of the weak spin-orbit force, like the spin polarization and distortion of the angular distribution of the photoelectrons, may be, at least qualitatively, interpreted in a single-particle picture, the observed effect in the partial ionization cross section only occurs due to continuum correlation, i.e. the configuration interaction among continuum states. In order to emphasize the generality

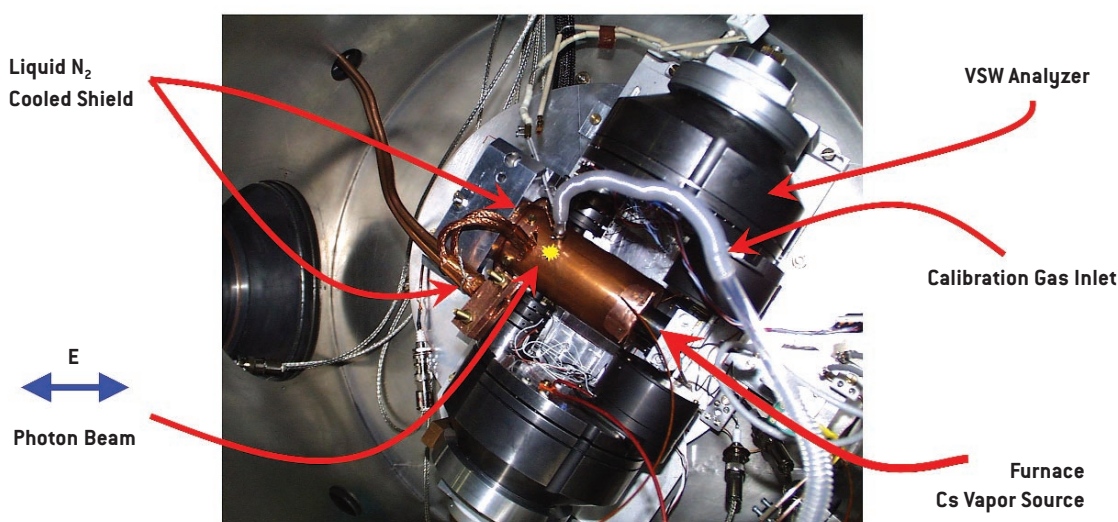
of this new effect, reference [2] reported also results for the $3d$ ionization of barium and cesium. In both cases the differences in the partial ionization cross section obtained by the introduction of the spin-orbit activated inter-channel coupling are very significant.

Here we present the first set of experimental results on the $3d$ photoionization of atomic cesium. The relative ionization cross section of the two ionization channels, $3d_{5/2}$ and $3d_{3/2}$, was followed over a photon energy range of 50 eV from the near-threshold region. For free cesium atoms to our knowledge no experimental results have been published so far. The experiments were carried out using the Angle Resolved Photoemission Spectroscopy end-station (ARPES) at the Gas Phase beamline at the storage ring ELETTRA (Trieste, Italy). The setup is shown in Figure 1. The photoelectron spectra have been recorded using two identical hemispherical analyzers (VSW, 50 mm mean radius) mounted facing each other at the pseudo-magic angle ($\sim 55^\circ$) with respect to the light polarization vector. They were operated in constant pass energy mode at a resolution of ~ 0.5 eV. Another channeltron was also mounted directly at the intersection of the vapor and light beam (outside of the cooling jacket) to record the $3d$ total ion yield spectra for calibration of the photon

energy. Cesium vapor was introduced using an anti-inductively wound, resistively heated oven, which was kept at a constant temperature ($\sim 130^\circ$ C). The oven and the ionization volume are enclosed in a cooled jacket designed to minimize contamination of the electron analyzers.

The performance of the full set-up has been verified using xenon. The measurements on xenon were done with the oven in place and the gas was introduced using a hypodermic needle pointing towards the ionization region, but kept at a distance of several centimeters. The results obtained are summarized in Figures 2(a) and 2(b) where the total ion yield spectra and relative partial ionization cross sections for the two $3d_{5/2}$ and $3d_{3/2}$ components are shown. The total-ion-yield spectra were recorded mainly to provide a photon energy calibration for the X-ray photoelectron spectra. In the figures are indicated the ionization thresholds for the two components of the $3d$ spin-orbit doublet. The background contribution near threshold is quite small in the photoelectron spectrum of xenon and the ionization cross section of $3d_{5/2}$ and $3d_{3/2}$ channels could be followed right to the respective thresholds also in our experiment. The results of the present experiment shown in Figure 1(b) are in reasonable agreement with the experi-

Figure 1. Photograph of the experimental setup.



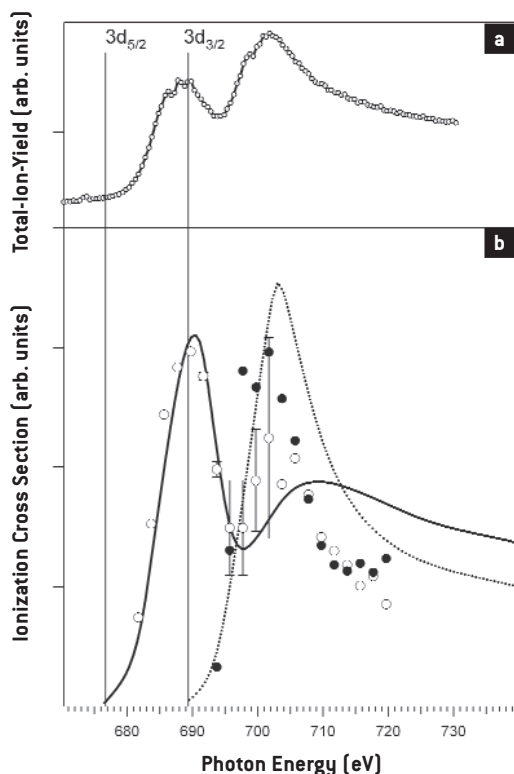


Figure 2. (a) Total-Ion-Yield spectrum of xenon recorded near the $3d$ ionization threshold. The two thresholds are marked. (b) Relative partial ionization cross section for the $3d_{5/2}$ (\circ) and $3d_{3/2}$ (\bullet) channels.

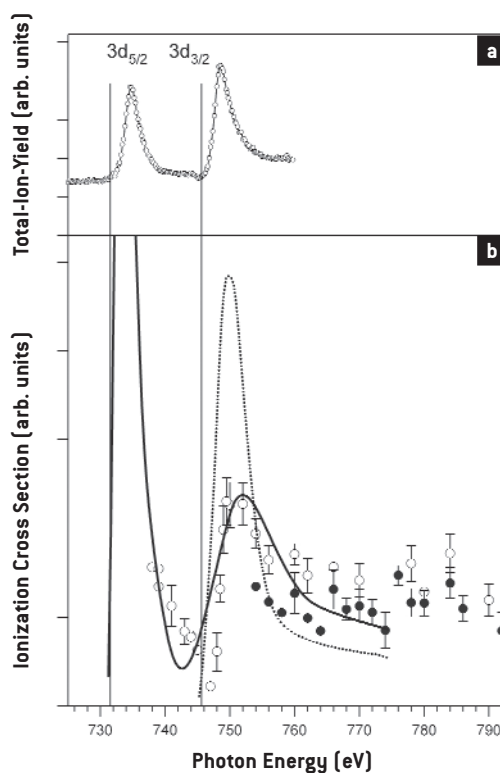
Solid/dotted lines are theoretical results from reference [2] shifted by ~ 2.5 eV. The experimental relative cross section has been normalized to the calculated curves at the excitation energy of ~ 690 eV.

ments of Kivimäki et al [1], and allow us to rule out systematic error in the measurements as well as in the data analysis. The experimental results on Cs are shown in Figures 3(a) and 3(b), where they are also compared with the theoretical results of Amusia et al. [2]. The energy scale was calibrated using the values of the $3d$ thresholds (731.6 and 745.6 eV for the $3d_{5/2}$ and $3d_{3/2}$ threshold, respectively) and the total-ion-yield spectrum. For the comparison the theoretical predictions have been shifted by 4.5 eV. Our results qualitatively confirm the theoretical predictions. Indeed the $3d_{5/2}$ relative cross section displays a clear minimum and a second maximum near the calculated maximum of the $3d_{3/2}$ relative cross section, which definitely prove the effect of the interchannel coupling. The $3d_{3/2}$ relative cross section does display a monotonous slowly decreasing behavior in the energy range investigated and above 760 eV is always slightly smaller than the $3d_{5/2}$ relative cross section. There are, however, some discrepancies between the

theoretical predictions and experiment. The slope of the $3d_{5/2}$ cross section leading to the second maximum in the photon energy range between 747 eV and 750 eV in (Figure 3) is steeper than in the theoretical result. Presently the reason for this discrepancy is unknown. Note also that the calculated cross section at $h\nu > 765$ eV is prominently bigger, particularly for $3d_{5/2}$ level, than in experiment. Inclusion of the $3p$ subshell effect failed to eliminate this discrepancy. On the experimental side measurements in this photon energy range suffer of a changing background when the strong resonance in the absorption spectrum is crossed. Then the second maximum appears to be narrower and centered at lower photon energy in the experiment than in the theory. Finally, the difference between the two relative cross sections above 760 eV is smaller in the experiment than in theory. It is remarkable that for $h\nu \geq 765$ eV the measured cross sections became considerably larger than the calculated ones, particularly for the $3d_{5/2}$ level.

Figure 3. (a) Total-Ion-Yield spectrum of Cesium recorded near the $3d$ ionization threshold. The two thresholds are marked. **(b)** Relative partial ionization cross section for the $3d_{5/2}$ (\circ) and $3d_{3/2}$ (\bullet) channels.

Solid/dotted lines are theoretical results from reference [2] shifted by 4.5 eV. The intensities experimental intensities have been normalized at the excitation energy of ~ 752 eV.



In summary the present results qualitatively confirm the theoretical predictions of Amusia et al. [2] of the existence of a new and explicitly manybody aspect of the spin-orbit interaction, the spin-orbit activated interchannel coupling which can significantly alter the photoionization cross-section of a spin-orbit doublet. These data together with the observation of an anomalous enhancement of the Cs $M_5N_{45} N_{45}$ Auger manifold in CsF thin films [4] confirm the generality of the effect, as predicted after the first observation and interpretation in xenon. However, there are some discrepancies between experiment and theory and the agreement is not as good as in the case of xenon. This might be partially due to shortcomings of the experiment, which in the case of atomic cesium is more demanding. Measurements of other observables, as the electron angular distribution or predicted non-dipole effects, would help to refine the comparison with theoretical data. The theoretical predictions have also been extended to include the $3d$ ionization of barium atoms, and indicate a dramatic increase in

the ionization cross section of the $3d_{5/2}$ channel near the $3d_{3/2}$ ionization threshold. Such a large effect should be easily observed in the experiment. Therefore, measurements in barium have been started to verify the accuracy of the calculations.

References

- [1] Kivimäki A., Hergenhahn U., Kempgens B., Hentges R., Piancastelli M.N., Maier K., Rüdél A., Tulkki J.J. and Bradshaw A.M. 2000 *Phys. Rev. A* **63** 012716
- [2] Amusia M. Ya, Chernysheva L.V., Manson S.T., Msezane A.M. and Radojevic V. 2002 *Phys. Rev. Lett.* **88** 093002
- [3] Toffoli D., Stener M. and Decleva P. 2002 *J. Phys. B: At. Mol. Opt. Phys.* **35** 1275
- [4] Ruus R., Kooser K., Nömmiste E., Saar A., Martinson I. and Kikas A. 2004 *J. Electron Spectrosc. Relat. Phenom.* **137-140** 377

EMISSION-DEPTH-SELECTIVE AUGER PHOTOELECTRON COINCIDENCE SPECTROSCOPY

> **W.S.M. Werner, W. Smekal, H. Störi, H. Winter**

Institut für Allgemeine Physik, Vienna University of Technology, Wiedner Hauptstraße 8-10, 1040 Vienna, AUSTRIA

> **G. Stefani, A. Ruocco, F. Offi**

Dipartimento di Fisica and Unità INFN, Università di Roma Tre, via della Vasca Navale 84, 00146 Rome, ITALY

> **R. Gotter**

TASC Laboratory, CNR-INFN, AREA Science Park, S.S. 14 km 163.5, 34012 Trieste, ITALY

> **A. Morgante, F. Tommasini**

TASC Laboratory, CNR-INFN, AREA Science Park, S.S. 14 km 163.5, 34012 Trieste, ITALY

Dipartimento di Fisica, Università di Trieste, via Valerio 2, 34127 Trieste, ITALY

Electron spectroscopy is a well-established tool for investigating the electronic, structural and magnetic properties of materials in various aggregation states. New solid state systems that hold the promise of entirely new approaches to technological applications are increasingly complex and typically confined in overlayer/interface assembled structures or thin multilayers, both on the nanometer scale and including a large number of constituent in a variety of chemical states. Therefore, there exists a compelling need for techniques that can explore the local electronic structure of individual constituents with increasing discrimination.

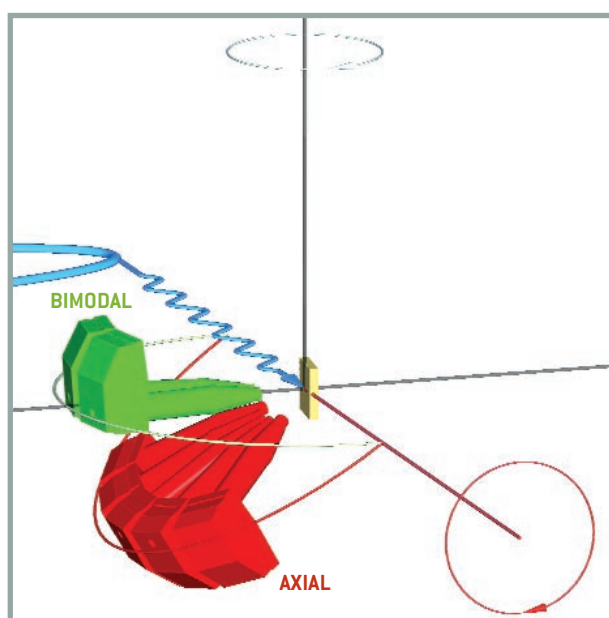
In conventional electron spectroscopy the average probing depth can be varied by changing the photoelectron kinetic energy and take-off angle. However, it is not possible in this way to directly select the depth range of photoelectrons accepted for analysis with a resolution better than the mean free path. This poses severe restrictions for calibrating the depth scale of nano-systems where a depth resolution significantly smaller than the electron mean free path is of great interest.

In the present work, we have shown that by measuring photoelectrons in coincidence with Auger electrons that have lost a fraction of their original energy, it is possible to select the depth range from which individual photoelectrons originate. Since in coincidence measurements, the Auger- and associated photoelectron originate from the

same atom and the energy lost by the Auger electron is proportional to its generation depth, the average depth from which the recorded photoelectrons originate can be selected by measuring the photoelectrons in coincidence with the loss features in the Auger spectrum. This possibility to discriminate the emission depth of individual photoelectrons makes Auger Photoelectron Coincidence Spectroscopy (APECS) a unique non-destructive tool to investigate interfaces at the nanoscale level [1].

Coincidence spectra were measured at the ALOISA beamline at ELETTRA by means

Figure 1. Schematic representation of multi-coincidence apparatus at the Aloisa beamline showing the scattering geometry used for this experiment.



of the available multi coincidence technique that makes use of seven hemispherical electron analyzers that can be positioned and tuned with a high degree of freedom [2]. As a matter of fact the photoelectron line shapes here reported have been collected simultaneously by the same analyzers, i.e. in the same conditions, but in timing coincidence with different analyzers tuned on the Auger electrons.

Si 2p photoelectrons and Si-LVV Auger electrons emitted from a Si(100) surface

were measured. The scattering geometry is sketched in Figure 1. The two photoelectron analyzers (bimodal in Figure 1) were very close to the surface normal while the Auger spectrometers (axial in Figure 1) were sitting on a plane 35° apart from it. Si 2p electrons were detected in the two bimodal analyzers (energy resolution $\Delta E=2.2$ eV) of the ALOISA apparatus (see Figure 1) while Auger electrons were reaching in coincidence the five axial analyzers ($\Delta E=3$ eV). Two of them were tuned to the no-loss Auger peak,

Figure 2. Experimental Si-LVV spectrum (dash-dotted line) and subjected to a Partial Intensity Analysis (open circles).

These three components compare well with the assignment made by means of an extended Cini-Sawatzky theory.

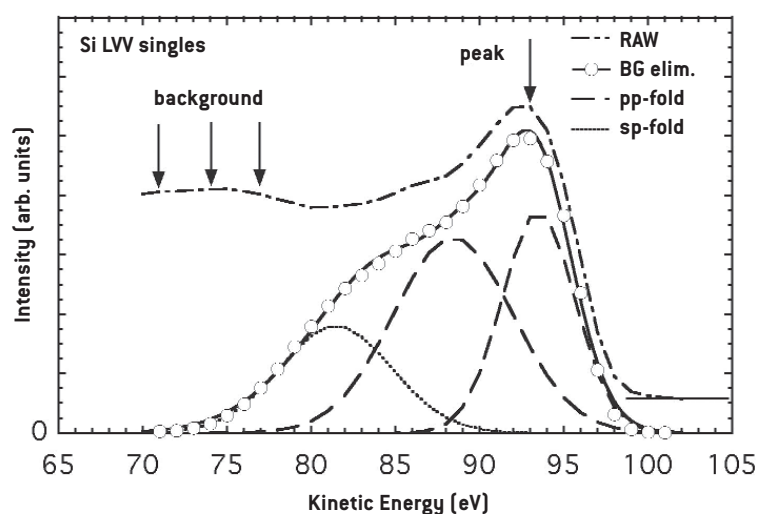
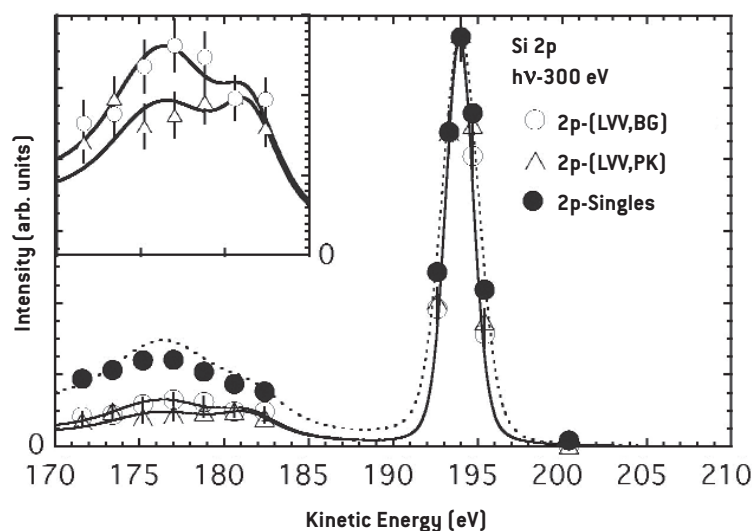


Figure 3. Si 2p spectrum measured in coincidence with the peak (PK) as well as with the background (BG) of the Si-LVV Auger line. The filled circles are the corresponding singles intensities. The solid and dotted lines represent results

of model calculations with the SESSA software [Simulation of Electron Spectra for Surface Analysis]. Calculated emission depths are 2.0 ± 2.1 Å, 4.7 ± 4.9 Å, 6.1 ± 6.5 Å for PK, BG and singles spectra, respectively.



while the other three measured the intensity at the first plasmon loss, as indicated by the arrows in Figure 2. After data acquisition, the spectra recorded in coincidence with the LVV peak and plasmon loss were combined to yield the $2p$ spectra shown in Figure 3 with the required statistics in the plasmon region.

The results are summarized in Figure 3. The filled circles represent the singles spectra of the Si $2p$ region that are compared with the intensities measured in coincidence with the elastic peak (open triangles, referred to as “PK” hereafter) and the inelastic background (open circles, “BG”) in the Si- LVV Auger electron line. All data shown in this figure are normalized to the same height in the peak maximum. The intensity of the plasmon in the PK spectrum is significantly reduced as compared to the singles spectrum, by about a factor of 2.5. This is a consequence of the well-known enhancement of the surface sensitivity of APECS as compared to ordinary XPS. In the BG spectrum, the first plasmon intensity is again higher, indicating that the path length the electrons travel inside the solid is longer, or in other words, that they originate from greater depths.

An estimate for the average emission depth $\langle z \rangle$ in APECS can be obtained in terms of the mean free paths $\lambda_{A,X}$, emission angles $\theta_{A,X}$ and collision number $n_{A,X}$ for the photoelectrons (X) and Auger (A) electrons, respectively [1,3]:

$$\langle z \rangle_{n_X, n_A} = (n_A + n_X + 1) \frac{\mu_A \mu_X}{\mu_A + \mu_X}$$

where $\mu_{A,X} = \lambda_{A,X} \cos(\theta_{A,X})$. According to this model, the emission depth of the elastic peak in the photoelectron spectrum ($n_X = 0$) can be selected by measuring the spectrum in coincidence with energies corresponding to a particular number n_A of plasmon losses in the Auger line. For common electron spectroscopy, the photoelectrons in the elastic peak always originate from the same average depth $\langle z \rangle = \mu_X$.

A quantitative agreement with the theoretical model for the surface sensitivity of APECS [1] (solid and dotted lines) can be observed in Figure 3, allowing us to conclude that the three $2p$ -photoelectron spec-

tra shown in Figure 3 originate from entirely different depth regions: $\langle z \rangle_{0,0} = 2.0 \pm 2.1$ Å, $\langle z \rangle_{0,1} = 4.7 \pm 4.9$ Å and $\mu_X = 6.1 \pm 6.5$ Å. The quoted uncertainties in these average depths are not experimental errors, but are due to the statistical fluctuations corresponding to a certain energy loss of the Auger electrons.

References

- [1] W.S.M. Werner, H. Störi, and HP. Winter, *Surf. Sci.* **518**, L569 (2002)
- [2] R. Gotter, A. Ruocco, A. Morgante, D. Cvetko, L. Floreano, F. Tommasini, G. Stefani, *Nucl. Instrum. Methods Phys. Res., Sect. A* **467**, 1468 (2001)
- [3] W.S.M. Werner, W. Smekal, H. Störi, H. Winter, G. Stefani, A. Ruocco, F. Offi, R. Gotter, A. Morgante, F. Tommasini, *Phys. Rev. Lett.* **94**, 38302 (2005)

SURFACE AND INTERFACE SCIENCE

Interfacial processes are in the heart of key technologies that involve design and fabrication of structures with reduced dimensions, e.g. catalysts, electronic and magnetic devices, chemical and bio-sensors, etc. Among the current research, frontiers in surface and interface science are bonding and self-organization processes at complex interfaces, such as realistic catalytic systems, oxides, polymers, biopolymers and bio-molecules. Beyond modern material technology and applications a wide range of novel physical and chemical properties at surfaces and interfaces still need to be studied and understood, e.g. the effect of quantum confinement of electrons in low dimensional structures on the physical properties and reactivity is a topic with many questions that remain unanswered. Many of the important advances in surface and interface science have been made thanks to the development of powerful characterization techniques at the third generation soft X-ray synchrotron radiation facilities. Most of these techniques are based on X-ray absorption and photoemission spectroscopies adding also possibility for lateral resolution using electron optics or photon focusing devices.

The highlights in the surface and interface section represent research done employing the X-ray spectroscopy techniques using photon-in/electron-out mode, namely X-ray photoelectron spectroscopy (XPS), Auger electron spectroscopy (AES) and X-ray absorption near edge spectroscopy (XANES) in combination, when necessary, with ancillary 'laboratory' structural techniques as low energy electron diffraction (LEED), low energy electron microscopy (LEEM) and atomic force microscopy (AFM).

The first contribution reports on the coincidence techniques developed at the INFM-ALOISA beamline, which allows the features in the Auger spectra to be associated to the corresponding core hole. It demonstrates the potential of the photoelectron-Auger coincidence spectroscopy to identify the chemisorption geometries of adsorbed Na adatoms, and the possibility to expand the application field of the Auger spectroscopy for determination of the adatom bonding configurations.

The second contribution is focused on the effect of electron confinement in ultrathin metal films on their surface reactivity. Sensible difference in the local oxidation rate of Mg films with varying thickness has been demonstrated using chemical specific imaging, combined with LEEM and LEED. The measured difference in the local reactivity correlates to the periodic changes in the density of electronic states induced by quantum-well states crossing the Fermi level of the Mg film.

The third contribution exploits the potential of the XPS and XANES for detailed structural and bonding characterization of self-assembled monolayers of peptide nucleic acid (PNA) on Au and their interaction with DNA molecules. The core level and XANES spectra obtained at the SuperESCA beamline, and the complementary ex-situ AFM results have provided the necessary basis for describing the mechanism responsible for the DNA recognition capability of the PNA self-assembled monolayers.

Maya Kiskinova

SELECTIVITY OF AUGER DECAYS TO THE LOCAL SURFACE ENVIRONMENT

> M.I. Trioni, S. Caravati, G.P. Brivio

CNR-INFM and Dipartimento di Scienza dei Materiali, Università di Milano-Bicocca, Via Cozzi 53, 20125 Milano, ITALY

> L. Floreano, F. Bruno, A. Morgante

TASC Laboratory, CNR-INFM, AREA Science Park, S.S. 14 km 163.5, 34012 Trieste, ITALY

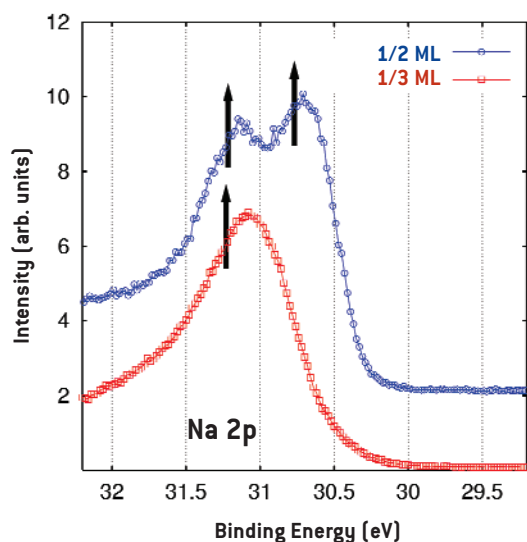
Figure 1. Na 2p photoemission spectra taken with a photon energy of 150 eV and energy resolution better than 325 meV for the upper spectrum and 450 meV for the lower one. Room temperature spectra at 1/2 ML [2×2 phase] and at 1/3 ML [$(\sqrt{3} \times \sqrt{3})R30^\circ$ phase] are shown in blue and red, respectively. The arrows identify the DFT energies.

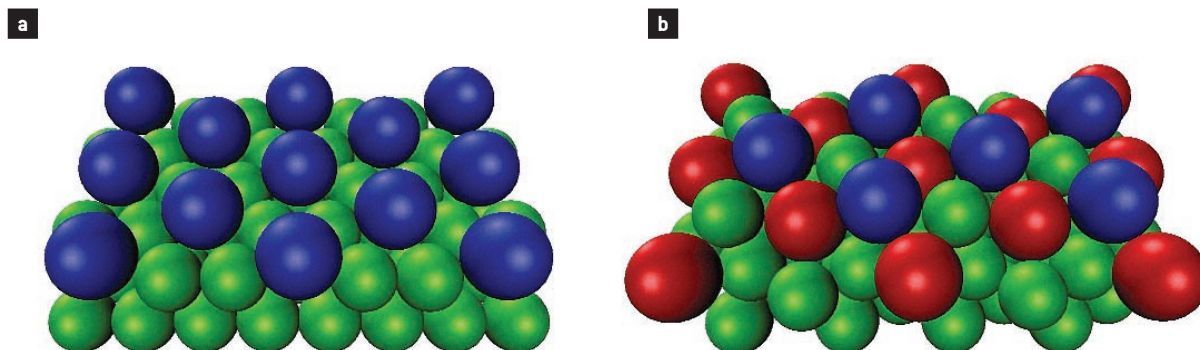
Auger spectroscopy as a sensitive tool for surface analysis is currently receiving a new impetus thanks to coincidence and synchrotron radiation measurements. For Auger processes that involve valence electrons, the Auger peaks transform into broader bands. Such features account for the local density of states (LDOS) around a core-ionized atom, and for correlation properties like plasmon satellites. In this work, by a joint theoretical and experimental investigation, we have shown that such Auger lineshapes contain further important information [1]. In fact, their analysis may allow one to derive structural properties, such as different surface reconstruction and adsorption geometries. Consequently, our results open up a new route to significantly extend the applicability of Auger spectroscopy to the surface microscopic analysis.

We have studied Na/Al(111), a system in which different Na adsorption geometries,

on changing the adatom fractional coverage and the substrate growth temperature, are known from previous experiments and calculations. We have concentrated on the Core Core Valence (CCV) Auger line-shapes of electronically excited Na atoms in order to be able to use a first principle approach, which greatly increases the accuracy of the results with respect to phenomenological models. In fact, CCV spectra of alkali metals can be taken into account accurately in the Kohn-Sham scheme of the density functional theory (DFT), since the system may be assumed to be in a relaxed quasi ground state with a core hole on the adatom. In this framework, we have calculated the Auger profiles of Na adsorbed at different sites via the excited state LDOS. From the experimental point of view, we have exploited last generation synchrotron radiation facilities, which allow for obtaining the very weak CCV signal of the adatoms. In this way, such Auger profiles and their dependence on the Na adsorption geometry have been measured in an unambiguous way. We have found that the theoretical Auger spectra are in excellent agreement with the experimental ones.

To calculate the CCV Auger decays we have determined the transition rates of an adsorbate by using an approximate expression, which sums up a suitably weighted orbital resolved valence LDOS calculated in a localized sphere centered at the ionized impurity [2]. Its radius essentially depends on the range of the adatom core wave function, and has been worked out by DFT by applying the exact Fermi golden rule on a simple jellium substrate. Consequently, it is a property of the chemical species, regardless of the substrate and the impurity site (bulk,





sub-, or on-surface). The DFT calculations of the LDOS have been performed on a semi-infinite realistic solid in the local density approximation by using the Green function embedding method [3]. Finally, we have obtained the Auger profiles by convolving the rates with a Lorentzian, accounting for hole lifetime, and a Gaussian, for instrumental broadening.

The experiments have been carried out at the INFM-ALOISA beamline installed at the ELETTRA Synchrotron in Trieste. The Na $2p$ photoemission spectra for two representative depositions at room temperature (RT) are shown in Figure 1. The DFT energies (arrows) have been derived from the Kohn-Sham eigenvalues by applying the transition state within our DFT approach. In Figure 1, at Na coverage of $1/3$ ML, only one $2p$ component is observed in XPS. The film shows instead an additional $2p$ component at lower binding energy, when further Na is evaporated up to the saturation coverage. Several investigations argue that Na deposition at RT creates first a $(\sqrt{3}\times\sqrt{3})R30^\circ$ phase at $1/3$ ML, then a 2×2 phase at the saturation coverage of $1/2$ ML, both with Na and Al intermixing. In particular the $1/3$ -ML phase is formed by the substitution of one Al atom by Na every three surface unit cells (see Figure 2a). For the 2×2 phase two distinct Na adsorption sites are observed in the photoemission spectrum. Most authors agree on a two-layer Na-Al surface alloy, where the inner Na atoms are substitutional and the outer Na-Al layer is formed by Na atoms in fcc sites and Al atoms in hcp ones (Figure 2b).

The measurement of the Na KLV Auger spectra is a difficult task due to three concurrent factors: i) the decay rate is very small as compared with KLL transitions, which dominate the Auger spectrum; ii) the Na signal arises from a tiny amount of atoms, since we are considering structures in the sub-monolayer range; iii) the background is strongly affected by the Al L-shell photoemission, whose plasmons are also very intense and numerous. We concentrate on the $KL_{2,3}V$ peak, since data of the more intense KLL transition partially overlap on those of the KL_1V one, hence the analysis may result less transparent. In this respect the most striking result of this work is displayed in Figure 3, namely the clear difference between the Auger spectra of the Na films at $1/3$ ML and at saturation, the latter exhibiting a shoulder on the $KL_{2,3}V$ peak at 1.5 eV lower energy (see also Figure 4). The weak bump at ~ 1027 eV in the $1/2$ ML

Figure 2. Panel **(a)**: model of the $1/3$ ML Na phase. Substitutional Na atoms in a $(\sqrt{3}\times\sqrt{3})R30^\circ$ symmetry are coloured in blue. Panel **(b)**: model of the $1/2$ ML $[2\times 2]$ Na phase, as made by a Na bilayer. The inner Na atoms (blue) are substitutional, while the outer Na-Al layer is formed by Na atoms in fcc sites (red).

Figure 3. The Na KLV Auger spectra. The 2×2 phase is reported in blue and the $(\sqrt{3}\times\sqrt{3})R30^\circ$ phase in red. The dashed line is the background from the clean Al $\{111\}$ surface.

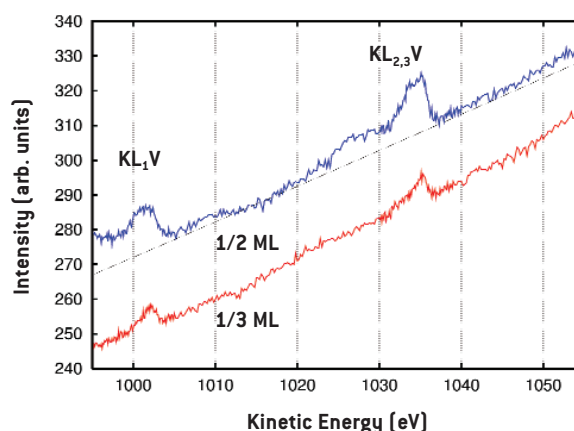
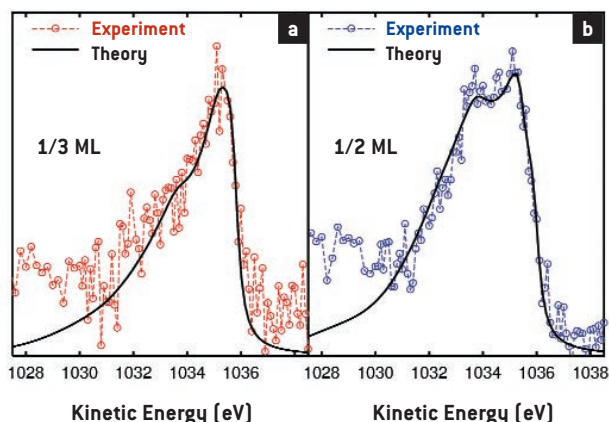


Figure 4. (a): the Na ($\sqrt{3}\times\sqrt{3}$)R30° phase (1/3 ML). Calculated (solid line) and measured (red circles) KL₂₃V Auger profiles. The calculated curve, normalized to the experimental data, obtained convolving the Auger rate with a Lorentzian with half width equal to 0.42 eV for the core hole lifetime and a Gaussian for

nominal instrumental broadening. The measured one obtained after background subtraction. **(b):** the Na 2×2 phase (1/2 ML). Calculated (solid line) and measured (blue circles) KL₂₃V Auger profiles. The calculated curve as in panel (a) but summing the contributions from the two inequivalent Na atoms (see text).



spectrum is due to a small amount of sodium oxide, whose formation has been observed to be faster than for the 1/3 ML surface.

The agreement between the experimental and theoretical KL₂₃V spectra, reported in Figure 4, is impressive. For the 1/3 ML, in panel a), both theoretical and experimental spectra display a main feature of the same shape and intensity. On the other hand, to fit the experiments for the 1/2 ML phase, it is necessary to sum up the contributions of the two theoretical spectra obtained from the inner and outer Na atoms. The best fit was obtained by shifting the Auger spectrum of the outer atom by -0.5 eV, and assigning a weight of 3/8 to the outer Na atom signal and 5/8 to the inner one. The weight ratio between the two Na components is in accord with the analysis of the relative height of the XPS signal (see Figure 1). It is interesting to note that this result suggests a different population for the Na atoms in the two inequivalent sites.

In conclusion, we have demonstrated the capability of CCV Auger line-shapes to account for the geometry of different adsorption phases for a given atom on the same solid surface. This approach could be extended to Core-Valence-Valence decays too. In fact, DFT calculations can be employed to determine, via the LDOS, the Auger rates of a large class of adsorbate systems, provided that the width of the valence

band of the solid is much larger than the on-site Coulomb interaction representing the final state correlation interaction between two valence holes. We also wish to stress that our theoretical method is not only able to determine the line-shapes of Auger spectra but is also potentially capable to predict features from different adsorbate components coexisting in the signal. While the former result has been verified experimentally, the latter one requires the use of coincidence techniques, a field of growing interest and expansion at synchrotron facilities. In fact, photoelectron-Auger coincidence spectroscopy allows one to unequivocally associate every Auger feature with the originating core level photo-hole. In all these respects, this work should provide new perspectives for Auger spectroscopy.

References

- [1] Trioni M.I., Caravati S., Brivio G.P., Floreano L., Bruno F., and Morgante A., *Physical Review Letters* **93**, 206802 (2004)
- [2] Du A.J., Trioni M.I., Brivio G.P., and Bonini N., *Surface Science* **545**, L753 (2003)
- [3] Butti G., Caravati S., Brivio G.P., Trioni M.I., and Ishida H., *Physical Review B* **72**, 125402 (2005)

TUNING SURFACE REACTIVITY VIA QUANTUM ELECTRON CONFINEMENT

> L. Aballe, A. Barinov, A. Locatelli, M. Kiskinova

Sincrotrone Trieste SCpA, Strada Statale 14, km 163.5, in AREA Science Park, 34012 Trieste, ITALY

> S. Heun

TASC Laboratory, CNR-INFM, Strada Statale 14, km 163.5, 34012 Trieste, ITALY

INTRODUCTION

The chemical reactivity of surfaces is a crucial property of many technological materials. It determines the chemisorption of molecules and atoms, the first reaction step playing a decisive role in their interaction with gases. A distinct feature of commonly used catalysts, protective coatings and gas sensors is that they are composed of nano-particles or thin films on metal, semiconductor or oxide supports, i.e. materials with strongly reduced dimensions in one or more directions. These materials typically present a chemical activity strongly modified with respect to the bulk parent. Several effects are thought to be responsible such as size effects on the atomic and electronic structure, strain, or interaction with the substrate. Our study aims at a quantitative understanding of the effect of electron confinement on surface reactivity in ultrathin metal films. Electrons in such films can be confined between the surface and the interface to an appropriate substrate (either by an absolute energy gap or by a symmetry- or momentum-dependent gap), resulting in a discrete number of allowed states. These commonly called quantum-well states (QWSs) modify the electronic density around the Fermi level, which determines the reactive properties of the materials. Studying the oxidation of ultrathin magnesium films, we demonstrate the essential role of the changes in the electron density due to QWSs in the dissociative O_2 adsorption, determining the initial oxidation rate.

EXPERIMENTAL

Measuring the influence of QWSs on surface reactivity is a challenging task: it requires

atomically flat films and exactly the same reaction conditions in order to derive unambiguous conclusions. We used a combination of complementary microscopic methods to study the effects of QWSs on the initial oxidation rate of Mg films grown in-situ on a W(110) substrate. This is an ideal model system, because the Mg films grow epitaxially with (0001) orientation, develop well-defined QWSs [1] and have a high affinity to oxygen.

The spectroscopic photoemission and low energy electron microscope SPELEEM available at the “Nanospectroscopy” beamline allowed us to characterize the morphology, local structure and local chemical state

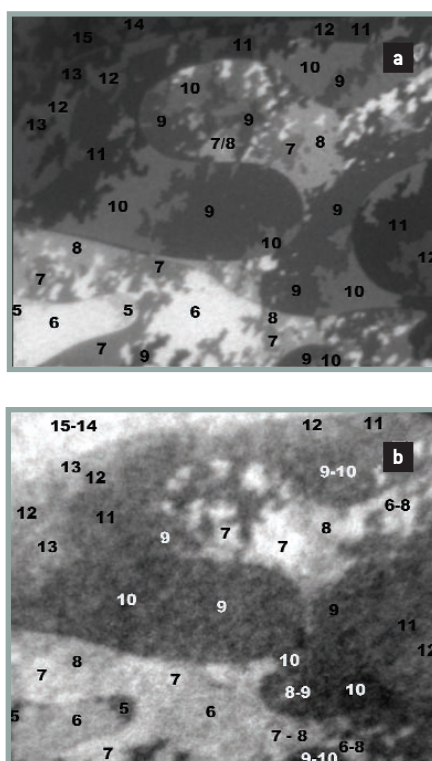


Figure 1. $6 \times 5 \mu\text{m}^2$ images of a Mg film in an advanced growth stage. **(a)** 1.3 eV LEEM image: the indicated number of atomic layers corresponding to the micro-regions was determined following the reflectivity changes during film growth. **(b)** XPEEM image of the same Mg film after exposure to 9 L of O_2 at 350 K, where the contrast corresponds to the extent of local Mg oxidation. The image is obtained by measuring the Mg 2p intensity of oxidised Mg (I_{ox}).

of the Mg films at a sub-microscopic length scale. The growth of Mg films was followed in real time with low energy electron microscopy (LEEM) with atomic height resolution thanks to interference effects in the backscattered electrons used for imaging. Micro-spot low energy electron diffraction (LEED) measurements showed a bulk-like Mg (0001)-(1×1) structure already above three atomic layers. Growth parameters were optimized for a wide thickness distribution that allowed probing simultaneously the oxidation of Mg micro-regions of different thickness, excluding any side effects due to variations in the O₂ exposure or temperature. Typical growth parameters are 400 K and 0.1 layer/minute. The oxidation experiments were performed at ~ 350 K and oxygen partial pressures ≤ 10⁻⁸ mbar. The magnesium valence band and 2p core level were measured locally by X-ray photoemission electron microscopy (XPEEM) and used as fingerprints of the oxidation rate. Mg surface atoms bound to oxygen are characterized by a distinct chemically shifted broad feature in the Mg 2p spectra that grows at the high binding energy side of the metallic Mg 2p peak. This 'oxide' component can be distinguished from an oxygen density less than 0.1 atomic layers and its intensity is

proportional to the relative number of Mg atoms bound to O.

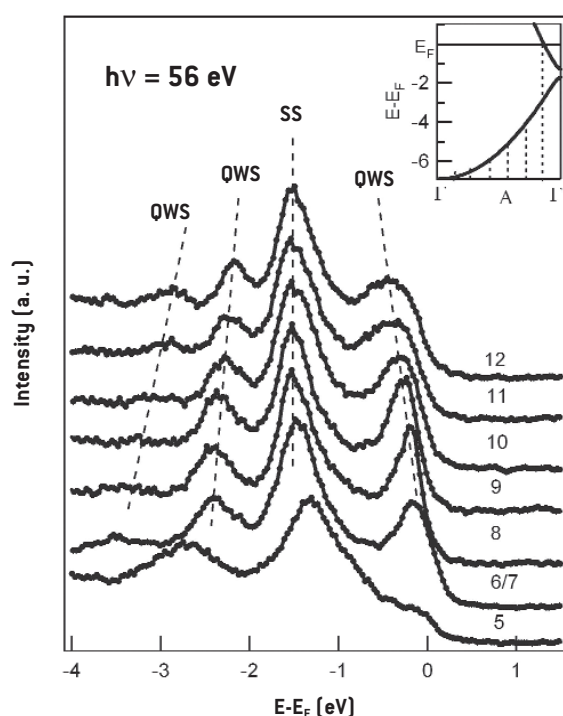
RESULTS AND DISCUSSION

The local surface reactivity was probed by comparing the initial oxidation of regions of the Mg film having different thickness. Mg oxidation begins with dissociative adsorption of O₂, followed by an intermediate stage of incorporation of the oxygen atoms and growth of MgO islands that coalesce, ending with the formation of a MgO bulk-like phase [2]. At these relatively low O₂ doses the coalescence of the MgO islands is not completed and the oxidation is limited to the two topmost atomic layers, concomitant with the very high surface sensitivity of our XPEEM measurements (photoelectron escape depth of ~2.8 Å). In fact, it is in the very first oxidation stages, when most of the surface is still metallic, that electronic quantum size effects dominate more strongly.

The LEEM image in Figure 1(a) shows a typical Mg film with coexistence of regions from 5 to 15 atomic layers. The XPEEM image of the Mg 2p 'oxide' component in Figure 1(b) shows the lateral heterogeneity in the extent of Mg oxidation for the same film after exposure to 9 Langmuir of O₂. The brighter regions correspond to a more advanced oxidation, i.e. the oxidation rate in these regions is faster. Comparison with Figure 1(a) reveals immediately a clear modulation of the oxidation rate with thickness: the regions of 6 to 8 and 13 to 15 atomic layers are more heavily oxidized. This modulation is directly correlated to the periodic changes in the density of electronic states induced by quantum-well states crossing the Fermi level of the Mg film, as described below.

Using XPEEM we recorded laterally resolved valence band spectra of the Mg layers. As shown in Figure 2, spectra of single atomic thickness regions exhibit a number of quantum well states derived from the magnesium s-p band, caused by electron confinement within the overlayer [1]. With increasing Mg coverage more states are allowed and they become closer in energy; a new peak appears across the Fermi level whenever the Mg film thickness is a multiple of 7/8 atomic layers, and shifts then to higher binding energies, as predicted by the

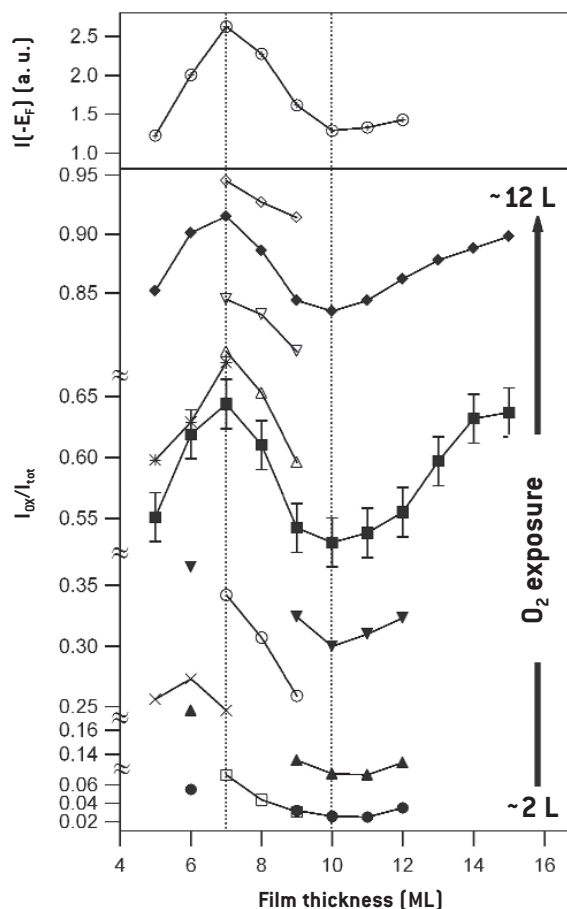
Figure 2. Valence band spectra obtained from micro-regions with the indicated thickness. The inset shows the Mg (0001) band structure in the Γ A direction (normal to the film). The allowed wavevector-energy (k_{\perp} , E) values for 7 atomic layers are calculated from the simple Bohr-Sommerfeld rule assuming perfect reflectivity at the surface and interface and are indicated by dotted vertical lines.



simple Bohr–Sommerfeld rule. The strong thickness dependence of the electronic structure results in oscillations of the density of states at the Fermi energy, a maximum occurring each time a further state becomes occupied.

The dependence of the oxidation rate on the number of atomic layers is quantitatively confirmed by a large set of experiments with Mg films consisting of different thickness combinations [3]. A striking correlation of the period of oscillation in the Mg surface reactivity with the period of crossing of the Fermi level by a QWS is found. The maximum in surface reactivity at 6–8 atomic layers occurs when the first QWS crossing the Fermi level increases the electron density of states, as shown in the top panel. The reactivity decreases to a local minimum at 9–12 layers and grows again at 14–15 layers when the second QWS crosses the Fermi level. In summary, films with the thickness at which the density of states at the Fermi level is increased due to quantum size effects exhibit a dramatic increase in surface reactivity [3]. This effect was observed at film thickness above 4 atomic layers, for which the chemically active surface layer is already insensitive to the presence of the substrate, and the strain due to lattice mismatch has been relieved. The surface reactivity can thus be tailored by simply changing the number of atomic layers that build the film.

The QWSs in Mg films evolve in the s-p band, and cannot be considered as laterally localized electronic states to which an orbital picture of the chemical interaction could be applied. The observed ‘tuning’ of the oxidation rate by varying the thickness of the Mg film can be attributed to QWS-induced oscillations in the magnitude of the electron density at the Fermi level. In accordance with theoretical concepts such electronic variations should play an essential role for the interaction between the O₂ molecule and the Mg surface, which involves a significant charge transfer to the lowest unoccupied O₂ molecular orbital and formation of O₂⁻ species. Even though a detailed explanation of the atomistic mechanisms involved is still under development, and understanding the more complicated case of transition metals with localized d-bonds will require a strong experimental and theoretical effort, we are confi-



dent that the present experimental study will provide fuel for lively discussion and design of further experiments towards a deeper understanding of the molecule-surface interaction.

References

- [1] Schiller F., Heber M., Servedio V.DP., Laubschat C., *Physical Review B* **70**, 125106 (2004), Aballe L., Rogero C., Horn K., *Physical Review B* **65**, 125319 (2002)
- [2] Bungaro C., Noguera C., Ballone P., Kress W., *Physical Review Letters* **79**, 4433 (1997), Goonewardene A.U., Karunamuni J., Kurtz R.L., Stockbauer R.L., *Surface Science* **501**, 102 (2002), Schröder E., Fasel R., Kiejna A., *Physical Review B* **69**, 115431 (2004)
- [3] Aballe L., Barinov A., Locatelli A., Heun S. and Kiskinova M., *Physical Review Letters* **93**, 196103 (2004)

Figure 3. Initial oxidation rate and the electronic density of states at the Fermi level as a function of the film thickness. [Lower panel] Plots of the relative weight of the Mg 2p ‘oxide’ component, I_{ox}/I_{total} , obtained in several experimental runs. Data indicated with the same symbols correspond to the same O₂ exposure. [Upper panel] Photoemission intensity at the Fermi level measured for different micro-region thickness before oxygen exposure with energy resolution of 0.25 eV.

SELF-ASSEMBLY OF PEPTIDE NUCLEIC ACIDS ON GOLD SURFACES AND ITS USE AS DNA AFFINITY BIOSENSORS

> C. Briones, E. Mateo-Martí

Centro de Astrobiología (CAB, CSIC-INTA), Carretera de Ajalvir km 4, 28850 Torrejón de Ardoz, Madrid, SPAIN

> C. Gómez-Navarro, E. Román, J.A. Martín-Gago

Instituto de Ciencia de Materiales del Madrid (ICMM, CSIC), Campus de Cantoblanco, 28049, Madrid, SPAIN

ABSTRACT

We have grown and characterized ordered self-assembled monolayers (SAMs) of peptide nucleic acid (PNA), a DNA analogue with higher biological and chemical stability. Our results show that thiol-modified single stranded (ss) PNA oligomers can form SAMs without requiring the co-immobilization of adjuvant molecules. The molecular orientation strongly depends on surface coverage, so that at optimal concentrations ssPNAs self-assemble standing-up on gold surfaces, in spite of their remarkable length of up to 7 nm. BioSAMs of ssPNAs recognize complementary ssDNA, and their specificity is such that they act as biosensors able to discriminate even a point mutation in target ssDNA. These structural and functional results have been obtained by means of label-free techniques for surface characterization such as synchrotron radiation based X-ray photoemission spectroscopy (XPS), X-ray absorption near-edge spectroscopy (XANES) and atomic force microscopy (AFM), and they have been recently confirmed using reflection absorption infrared spectroscopy (RAIRS).

INTRODUCTION

Self-assembly of molecules on surfaces provides an optimal way to produce organic layers with tailored properties, particularly those required for the development of biosensors and bioactive materials. Alkanethiols show an outstanding capability to form SAMs on gold surfaces, and a number of technological applications have been described. Nevertheless, thiol-modified DNA do not form SAMs on surfaces, rendering

disordered formless globular structures with reduced bioactivity. Such a disappointing behavior is due to the strong DNA-surface interactions as well as to the electrostatic repulsion among the negatively charged DNA molecules. Therefore, uncharged analogues of natural nucleic acids raised as suitable candidates to circumvent this problem. Interestingly, ssDNA films used in biosensors are typically less than 10 nm thick, so highly efficient, label-free and element-specific surface characterization techniques can be used.

We have performed this characterization through high resolution techniques such as XPS and XANES. The suitability of those methodologies for studying ex-situ prepared complex systems has been questioned because of the difficult data interpretation. We probe in this work that these techniques can be successfully applied.

PNA appears as the most studied DNA analogue since it was synthesized in 1991. PNA is an achiral and uncharged DNA mimic where the sugar-phosphate backbone is replaced with a peptide-like *N*-(2-aminoethyl)glycine polyamide structure, to which the nucleobases are connected by methylenecarbonyl linkages. PNA strongly and specifically binds to complementary DNA according to the Watson-Crick rules for base-pairing. These unique properties make PNA a suitable candidate for biosensor applications.

EXPERIMENTAL SETUP

Two cysteine-modified ssPNA oligomers were used: P-G142, Cys-O-O-AATCCCCGCAT,

and P-M41, Cys-O-O-GCCATCTCT (written in amino-carboxyl orientation). The Cys moiety at the PNA amino terminus provides the thiol group that allows immobilization on gold surfaces. The “O-O” spacer is a 3.0 nm long dimmer of 8-amino-3,6-dioxoacetic acid. The total lengths of the ssPNAs are 7.1 nm (P-G142) and 6.4 nm (P-M41). 31 nucleotide-long target ssDNA molecules were designed, with their central region complementary to the PNAs either perfectly or showing a single mutation mismatch. Further details can be found in [2]. Immobilization of ssPNA was performed at 22°C for 4 h in a humid chamber, on two different substrates: polycrystalline Au layers evaporated on glass and single-crystal Au(111). After the immobilization step, the crystals were rinsed in H₂O with agitation. Hybridization of the complementary ssDNA was performed for 1 hour in the appropriate buffer [1], at temperatures ranging from 41 to 58°C. Post-hybridization stringent wash was performed for 15 min at temperatures from 36°C to 64°C.

High resolution XPS and XANES experiments were performed at the Super-ESCA beamline in ELETTRA synchrotron radiation facility (Trieste, Italy). A hemispherical electron energy analyzer was used and the overall resolution (beamline+analyser) was estimated to be around 80 meV. The quantification by XPS of the total amount of PNA adsorbed on the surface before and after DNA hybridization was performed by normalizing the N1s core-level photoemitted signal to the Au4f peak measured in the

same conditions. We checked that the samples resisted desiccation and were not damaged after 36h of X-ray radiation.

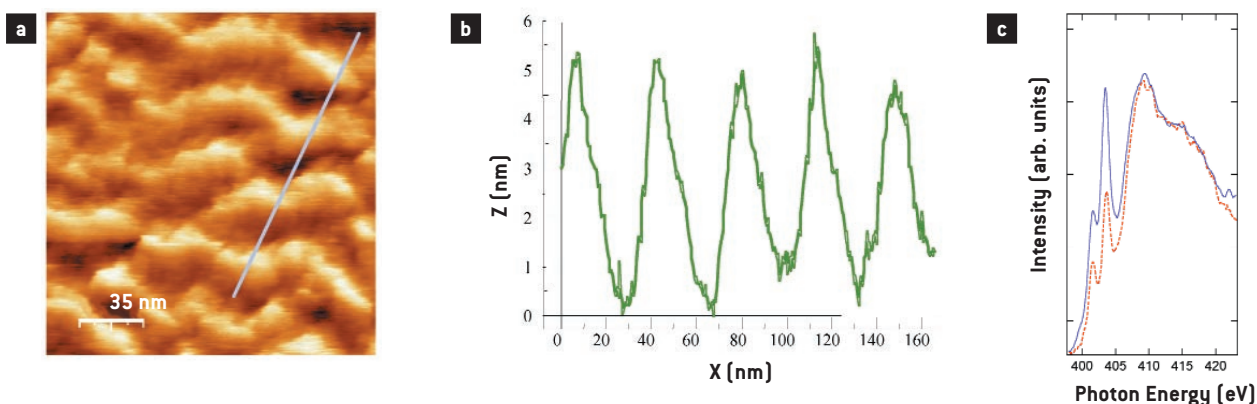
Polycrystalline Au layers evaporated on glass were flame-annealed to produce a predominant (111) faceting. A commercial Nanotec electronic system was used in non-contact dynamic mode. Olympus cantilevers with a silicon nitride tip, resonance frequency of 80 kHz, force constant of 0.74 N/m, and nominal radius smaller than 20 nm have been employed.

RESULTS AND DISCUSSION

The structural characterization of the ssPNA layers was performed by AFM and XANES. A systematic AFM study showed that at optimal surface coverage, corresponding to 1 μ M PNA, reproducible aligned and meandering patterns were observed (Figure 1a). The ordered protrusions are about 6 nm high from the bare surface and their width is 10 to 30 nm (Figure 1b), being interpreted as groups of molecules standing-up on the surface. The lower apparent height measured by AFM could be related (apart from some degree of flexibility allowed by the PNA backbone) to a small tilt of the molecule, that would also facilitate non-complementary hydrogen bonding between nucleobases placed at different position in neighboring molecules.

We used XANES as a complementary structural technique to check if the molecules show a preferential orientation on the surface. XANES spectra of ssPNA layers at

Figure 1. (a) AFM image recorded in air of ssPNA molecule P-G142 immobilized on gold at 1 μ M concentration. (b) Cross-section profile recorded across the line in (a), showing an ordered SAM of PNA, with groups of molecules standing up from the bare surface up to 6 nm in height. (c) XANES spectra, normalized to the σ^* intensity, at the N1s edge recorded at different polar angles of incidence. The angles between the surface normal and the X-ray polarization vector were 90° (dotted line) and 20° (solid line).



1 μM were recorded at the N threshold for different incident angles (Figure 1c). The spectra could be decomposed in two sharp π^* and a broad σ^* peak transitions, being the π^* transition enhanced as the light polarization vector approaches normal emission. Since most of the π^* orbitals lie along the backbone of the PNA and the σ^* are parallel to the nucleobases plane, the data indicate that the axes of the PNA stand almost perpendicular to the surface, in agreement with the arrangement observed by AFM [1]. These AFM and XANES results have been recently confirmed using RAIRS [3]. XPS (high resolution) detailed deconvolution analysis of the N(1s) core-level peak shows a shifted component originating from chemical effects [3]. A schematic model of the arrangement of PNA molecules on the surface is depicted in Figure 2.

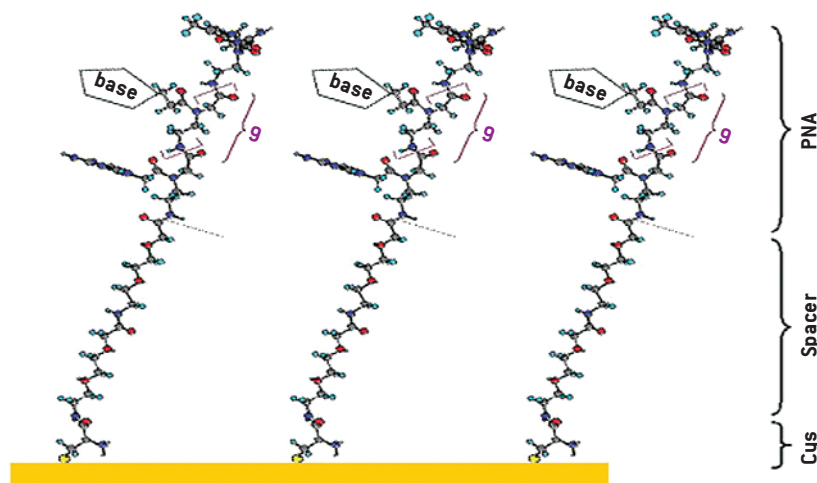
We have purposed a two-step mechanism for the formation of a bioSAM of ssPNA: i) ssPNAs are adsorbed on the surface as lying molecules; ii) at a certain coverage density the layer undergoes a phase transition and the molecular backbone realigns almost perpendicular to the surface. A similar mechanism was described for SAMs of alkanethiols and demonstrates the importance of the molecule-molecule interaction in self-assembly. One peculiarity of our system comes from the extraordinary length (up to 7 nm) of the immobilized PNA molecule that generates the SAM with respect to alkanethiol

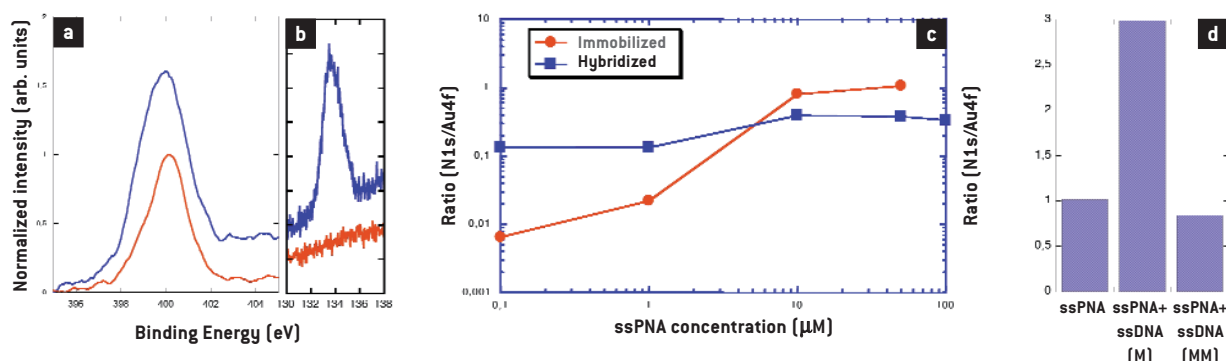
SAMs, which typically range from 0.2 to 2.5 nm high. Also interesting, SAMs of ssPNA are formed without requiring the addition of thiols or other adjuvant molecules that would lead to mixed monolayers, as reported for ssDNA. Two main reasons can account for the clear advantage of ssPNA over ssDNA in the formation of SAMs: the lack of charged groups in the PNA molecule and the higher rigidity of the PNA backbone composed of planar amide groups [1, 2].

To investigate the interaction of immobilized ssPNA with complementary ssDNA, a set XPS experiments was performed. A high-resolution XPS spectrum for N1s recorded at 500 eV of photon energy from an immobilized ssPNA SAM is presented in Figure 3a. We quantified an average increase of the normalized peak ranging from 2.6 to 3.2 times after complementary ssDNA hybridization. This suggests that in the optimal conditions the fraction of ssPNA hybridized with DNA target is near 100% [1]. A second fingerprint of the hybridization event comes from the emergence of a net P2p peak due to the phosphate groups in the DNA backbone (Figure 3b).

Figure 3c shows the N1s/Au4f photoemission signal for different concentrations of the immobilized ssPNA, before and after hybridization with complementary ssDNA. This signal is proportional to the concentration of ssPNA on the surface, up to a saturation value at 10 μM that corresponds to

Figure 2. Proposed immobilization geometry of the ssPNA molecules at optimal concentration on gold surface, derived from AFM, XANES and RAIRS data [1, 3]. The molecular backbones are aligned standing up from the surface. Tilted ssPNA molecules (7.1 nm long) are imaged by AFM as protrusions with an apparent height of 6 nm (Figures 1a and 1b).





the complete blocking of the available absorption sites at the surface by neighboring ssPNA molecules. For concentrations ranging from 0.1 to 1 μM , the enhancement of the signal after hybridization is close to 3, behaving as a sensitive biosensor. We have also tested the capability of the bioSAM of ssPNA to discriminate ssDNA targets bearing single point mutations. Post-hybridization washing protocols based on the increase of ionic strength did not allow a complete removal of the mismatched target, whilst optimized washing buffers including detergents or denaturant agents [1] permitted a perfect match/mismatch discrimination (Figure 3d). This improved specificity is equivalent to that recently obtained with conventional microarray technologies. Thus, bioSAMs of ssPNA offer the possibility of being employed for mutation screening and single nucleotide polymorphism mapping, relevant features for biomedical and biotechnological applications.

CONCLUSION

We have described the combined use of different complementary surface characterization techniques for the structural and functional analysis of SAMs of PNA on gold surfaces. The unique properties of ssPNA for self-assembly on surfaces encourage the use of PNA-based biosensors for the detection of label-free nucleic acid targets in complex biological samples. This interdisciplinary approach could open new lines of

research in the emergent field of bionanotechnology.

References

- [1] Briones C., Mateo-Martí E., Gómez-Navarro C., Parro V., Román E. and Martín-Gago J.A. Ordered self-assembled monolayers of peptide nucleic acids with DNA recognition capability, *Phys Rev Lett* **93**, 208103 (2004)
- [2] Briones C., Mateo-Martí E., Gómez-Navarro C., Parro V., Román E. and Martín-Gago J.A. Structural and functional characterization of self-assembled monolayers of peptide nucleic acids and its interaction with complementary DNA, *J Mol Catal A: Chem* **228**, 131 (2005)
- [3] Mateo-Martí E., Briones C., Román E., Briand E., Pradier C.M. and Martín-Gago J.A. Self-assembled monolayers of peptide nucleic acids on gold surfaces: a spectroscopic study. *Langmuir* **21**, 9510 (2005)

Figure 3. Functional characterization of the SAMs of ssPNA as biosensors. XPS spectra, normalized to the Au4f, of the N1s core level peak **(a)** and P2p peak **(b)** before [lower curve] and after [upper curve] hybridization of the SAM of 1 μM ssPNA with the complementary ssDNA. **(c)** XPS N1s/Au4f ratio for increasing ssPNA concentrations before and after hybridization with the complementary DNA at 100 μM . **(d)** Specificity of the biosensor studied by comparing the N1s/Au4f ratio before and after hybridization of ssPNA with the perfectly matching [M] and a single mutation mismatching [MM] ssDNA molecule: the use of optimized hybridization and washing buffers allowed to completely remove the mutated DNA while the matching DNA was maintained [see details in Ref. [1]].

NANOSTRUCTURES

The trend toward miniaturization is well known in the manufacturing and microelectronics industries, as evidenced by the rapid increase in computing power through reduction of the area and volume needed per transistor on chips. In material science a similar trend is also occurring, but for different reasons. Smallness itself is not the goal. Instead, it is the realization and the expectation that new properties intrinsic to novel nanostructures will enable breakthroughs in a multitude of technologically important areas.

The fact that nanostructures have higher surface areas than conventional materials is of particular interest to scientists. The impact of nanostructures on the properties of high surface area materials is a field of increasing importance to understanding, creating, and improving materials for diverse applications. High surface areas can be attained either by fabricating small particles or clusters where the surface-to-volume ratio of each particle is high, or by creating materials where the void surface area (pores) is high compared to the amount of bulk support material. Materials such as highly dispersed supported metal catalysts and gas phase clusters fall into the former category, and microporous (nanometer-pored) materials such as zeolites, porous carbons and nanotubes, fall into the latter category. Moreover, a fundamental driving force towards efforts to exploit the nanoscale or nanostructures is based upon the fact that nanostructured materials typically exhibit unique (quantum) properties that are expected to open windows of opportunity previously inaccessible with existing materials.

A very important (or maybe the most important) place among the building blocks of this new trend toward nanostructured materials and devices, is reserved to carbon-based materials, such as fullerenes and their relatives, carbon nanotubes, carbon nanoparticles and nanofoams and organic molecules. Reasons for this favored position include the simplicity of growth and manipulation of carbon-based materials, the versatility of their geometric and electronic structures as well as the wide range of magnetic and electronic properties, and the capability to self-assemble. The contribution from Larciprete et al. shows a nice example of how the electronic properties of carbon nanotubes bundles can be tuned from one-dimensional to three-dimensional by simply adding Li atoms to the bundles.

Over the last two decades, the development and improvement of new instruments, techniques and approaches to fabricate and characterize nanoscale materials have fueled much of the enormous growth in nanoscale science and technology, not only by making nanoscale materials relatively easily available for scientific study and characterization, but also in some instances, opening the door for large scale industrial use. It is important to recognize that nanoscale science and technology is not a “stand alone” field of endeavor, but rather is more of a “generic” area that is expected to have a critical impact and overlap in many areas of science and technology. The fields that fall under the “nanoscale” umbrella are many and diverse, illustrating that nanoscale science and technology is a collection of many different disciplines and areas of expertise.

The contributions from Tello et al. and Casalis et al. report two examples of this interdisciplinary and of our capabilities to fabricate in controlled positions nano-structures by means of scanning probes microscopies.

Andrea Goldoni

TRANSITION FROM 1D TO 3D BEHAVIOR INDUCED BY LITHIUM DOPING IN SINGLE WALL CARBON NANOTUBES

> R. Larciprete

*Sincrotrone Trieste S.C.p.A., S.S. 14 km 163.5, in AREA Science Park, 34012 Trieste, ITALY
CNR-Istituto dei Sistemi Complessi, via Salaria km 29.3, 00016 Monterotondo (RM), ITALY*

> L. Petaccia, S. Lizzit, A. Goldoni

Sincrotrone Trieste S.C.p.A., S.S. 14 km 163.5, in AREA Science Park, 34012 Trieste, ITALY

The electronic and structural properties of single wall carbon nanotubes (SWNTs) can be designed by introducing p-type and n-type dopant elements able to exchange charge with the C lattice. In the presence of dopants, charge transfer allows the Fermi level (E_F) position to be adjusted in the density of states (DOS), in a way which parallels the case of other C based material as fullerenes or graphite intercalated compounds (GICs).

Alkali metal intercalation represents an efficient route to accomplish n-type tube doping. Li intercalated SWNTs possess a strong technological interest as anode materials for Li-ion batteries, but also a high fundamental appeal, because unlike heavier alkali atoms, the lower atomic radius of lithium is compatible with adsorption even inside small radius tubes [1,2,3]. It has been calculated that Li adatoms should adsorb in the interstitial sites of the bundle crystallites as well as penetrate into the tubes through their open ends or through suitable topological defects and, similarly to adsorption on graphene, sit on top of the hollow sites (hexagon centers) [1,4,5].

In this study [6] we used high-resolution photoemission spectroscopy to investigate the electronic structure of Li doped SWNTs up to $Li/C=0.06$, in order to correlate the occurrence of charge transfer to the enhancement of the DOS close to the Fermi energy as well as to the transition from a one-dimensional (1D) Tomonaga-Luttinger liquid to a three-dimensional (3D) Fermi liquid character of the conduction electrons.

The experiment was performed at the SuperESCA beamline of ELETTRA. A com-

mercial mat of purified SWNTs (average diameter of 1.2 nm) was cooled at 150 K and dosed with Li. C1s and Li1s core level and VB spectra were measured at photon energy of 400, 135 and 90 eV, respectively, the corresponding overall energy resolution being 100 meV in the first case and 60 meV otherwise. Measurements were performed while the beam impinged at about 20° from the sample surface and photoelectrons were collected at normal emission.

Figure 1 shows the C1s spectra measured as a function of the Li/C ratio together with their best-fit curves with Doniach-Sunjić functions convoluted with Gaussians. The transfer of the Li valence electrons to the C π^* orbital is tracked by the shape and position of the C1s peak. Starting from the pristine SWNTs, the C1s peak exhibits a progressive shift towards higher BE with increasing Li intercalation. Moreover, the peak manifestly broadens on the high BE side. In the rigid band picture the change of localization of the Fermi level in the DOS causes a BE up-shift of all C related spectroscopic features. The inset in Figure 1 compares the BE displacements measured as a function of Li/C for the C1s peak and for the C $2p-\pi$ band, which at $Li/C=0.06$ are 0.26 eV and 0.30 eV, respectively. These values are significantly lower than the values reported in the case of K doping at similar alkali metal concentration [7,8]. As K intercalation is generally considered to correspond to a complete charge transfer from the alkali metal to SWNTs [8-10], then the behavior observed here indicate for Li a lower magnitude of charge exchange. Consider-

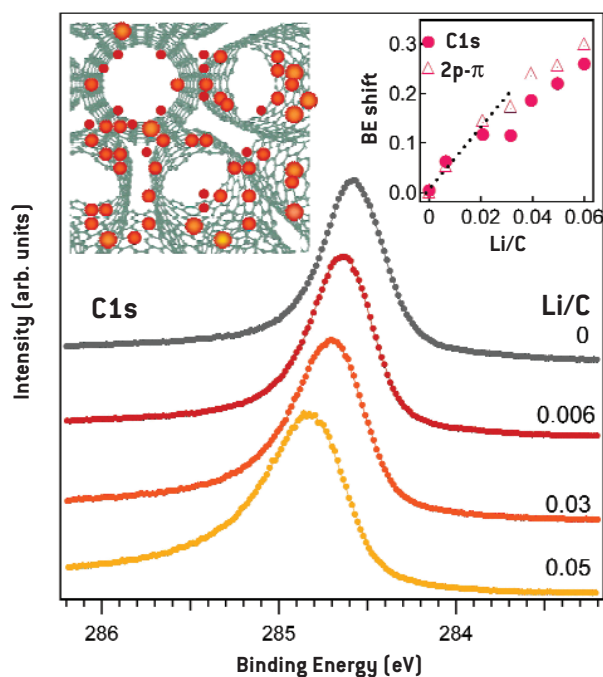


Figure 1. C1s experimental spectra (dots) and best fit curves (lines) taken on the pristine and lithiated SWNTs at increasing Li doping level. The peak

intensities are normalized to the same height. The right inset shows the BE shift measured for the C1s peak and the $2p-\pi$ band vs. the Li/C ratio.

ing that in GICs a more covalent character was found for the Li-C interaction relative to other alkali atoms [11], it seems reasonable that also for SWNTs the localization of the charge density along the Li-C bond enhances the covalency of the interaction and reduces the effective charge transfer.

Figure 2 shows the photoemission spectra measured in the near Fermi level region. The quantization of the electronic states along the SWNT circumference manifests with the appearance of weak intensities oscillations superimposed on the continuous photoemission spectrum, which arise from 1D van Hove singularities (VHSs) in the density of states [7,12]. The bottom curve in Figure 2, measured on the pristine SWNTs, clearly shows three oscillations at 0.4, 0.7 and 1 eV corresponding to S_1 , S_2 and M_1 VHSs, respectively, which indicate an average tube diameter of 1.2 nm, in agreement with the estimation obtained by electron energy loss spectra. Upon electron doping, the VHSs shift to higher BE following the behavior of the other C related peaks due to the new position of the Fermi level [7]. Moreover, the oscillations are damped and smeared out by

Li adsorption, because of the rising disorder and the progressive increase of the tube-tube interaction within the intercalated bundles, which extinguish the perfect 1D nature of the SWNT valence band.

The left inset in Figure 2 reports the photoemission spectra measured close to the Fermi energy for increasing Li concentration, whereas the inset on the right side shows how, with increasing Li/C ratio, the spectral integral in the range $-0.2 \div 0.2$ eV (A) rises with respect to the case of pristine nanotubes (A_0). It is interesting to discuss in detail the behavior and the origin of the observed DOS increase with Li concentration. The DOS for the undoped system is expected to be the superposition of the DOS of metallic and semiconducting SWNTs. According to our photoemission spectra, the metallic SWNTs should contribute with a finite flat DOS near E_F , having VHS peaks at ~ 1 eV below and above the Fermi level (M and M^* respectively). The semiconducting SWNTs should have a gap around E_F with occupied VHSs at 0.4 eV and 0.7 eV (S_1 and S_2) below the Fermi level and the unoccupied VHSs (S_1^* and S_2^*) symmetrically above it [13].

As Li is added to the system, electron doping concerns the metallic tubes at first, and the Fermi level moves into a flat DOS. This is consistent with the initial behavior (up to $\text{Li}/\text{C} = 0.02$) of the DOS at E_F , which remains constant, and the linear binding energy shift of the C related features (see Figure 1). At higher Li concentration, the DOS at E_F starts rising and accordingly the shift of the C related features deviates from linearity showing a lower doping dependence. The increasing DOS at E_F cannot be explained with the filling of the first S_1^* VHS because semiconducting tube doping would start at $\Delta E_F > 0.3$ eV, that is at Li concentrations higher than those that can be reached with our growth conditions.

There are two possible explanations for the observed behavior.

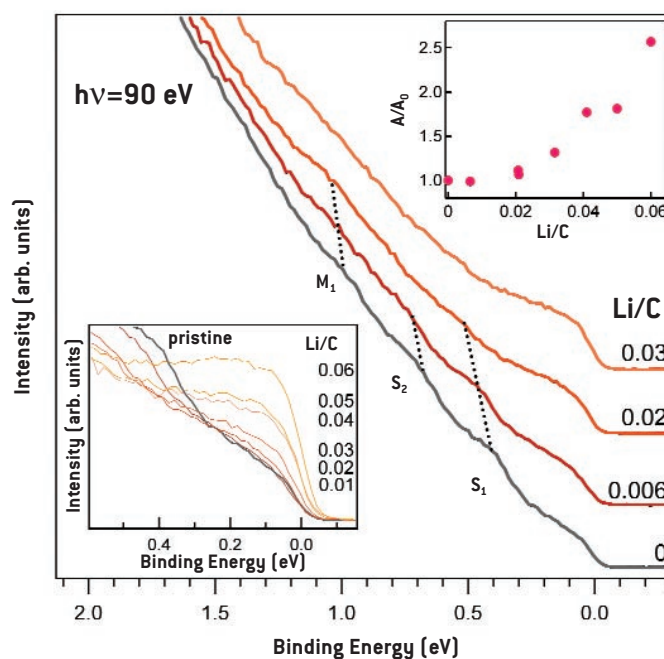
First, we note that in LiC_6 GIC the electronic structure of the graphite conduction band is modified by the interaction with Li because of the hybridization between the intralayer state of graphite and the $\text{Li}2s$ state, which originates a strongly dispersing band close to the Fermi energy [14]. Similarly, it has been calculated that the hybridization between Li and C SWNTs introduces some

new states in the conduction band [5]. The observed DOS enhancement can be then associated to the appearance of new states close to the Fermi level in the conduction band of the pristine SWNTs perturbed by the interaction with lithium.

A second explanation involves a possible transition from a Tomonaga-Luttinger liquid (1D) to a Fermi liquid (3D) in the conduction behavior of SWNTs. In a Tomonaga-Luttinger liquid the DOS vanishes at E_F following a power law dependence $n(E) \propto |E - E_F|^\alpha$, where $\alpha = (g + g^{-1} - 2)/8$ depends on the size of the Coulomb interaction and g is the Luttinger parameter [15,16]. We show in Figure 3 a double logarithmic representation of the photoemission spectra measured for pristine and Li doped SWNTs near the Fermi energy together with the corresponding fits, which allow obtaining α . For pristine tubes the exponent α results to be 0.54 [7,12]. With increasing Li/C ratio α reduces progressively and finally vanishes at $\text{Li}/\text{C} \approx 0.06$. The α values are plotted versus the Li/C concentration in the bottom inset of Figure 3, whereas the top inset in the same figure illustrates the change of the DOS profile.

Figure 2. Photoemission spectra measured on pristine and Li doped SWNTs. The dashed lines are guidelines for the evolution of the VHS peaks. The left inset shows the evolution of the near Fermi level

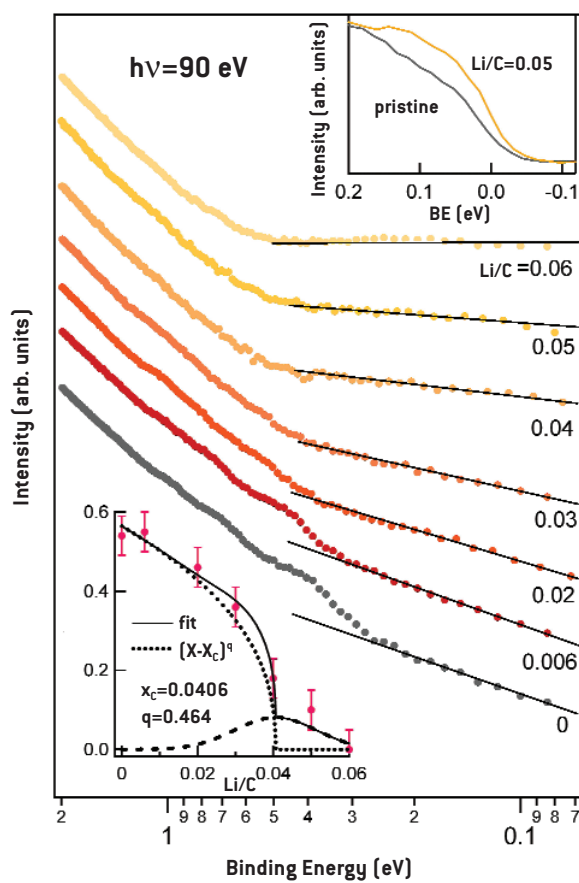
region with increasing Li doping. The increase of the spectra integral between -0.2 and 0.2 eV with respect to the pristine SWNTs is shown as a function of the Li/C ratio in the inset on the right side.



For n-doped SWNTs the electron injection should cause the system to evolve from a Tomonaga-Luttinger liquid to a Fermi liquid behavior, when the doping displaces the Fermi level into the S_1^* VHS [7]. This indeed makes metallic also the semiconducting tubes and imparts a three-dimensional character to the electronic structure. However, for Li intercalated SWNTs we observe a decay with doping more rapid than that, because α approaches zero when still only the metallic tubes are doped. Considering the possible inhomogeneous Li distribution on a scale of several tens of microns (the dimension of our beam spot), the transition to a Fermi liquid behavior is between $\text{Li/C}=0.04$ and 0.06 as shown by the solid line in the bottom inset of Figure 3, obtained by fitting the data with a power law decay $(x-x_c)^q$ for $x < x_c$ and zero above x_c (where x is the Li/C ratio and x_c the critical value for which α is zero) plus a Gaussian distribution around the critical ratio x_c . Therefore, the break down of the Tomonaga-Luttinger liquid behavior, rather than to the metallic character gained by the semiconducting tubes, has to be ascribed to disorder with increasing Li concentration and cross-links between the tubes mediated by the occurrence of interactions via the Li-C hybridized states close to the Fermi energy, which give a 3D character to the sample transport.

References

- [1] Dubot P. and Cenedese P., *Phys. Rev. B* **63**, 241402 (2001)
- [2] Yang J., Liu H.J., Chan C.T., *Phys. Rev. B* **64**, 085420 (2001)
- [3] Liu H.J., Chan C.T., *Solid State Commun.* **125**, 77 (2003)
- [4] Meunier V., Kephart J., Roland C., Bernholc J., *Phys. Rev. Lett.* **88**, 075506 (2002)
- [5] Zhao J., Buldum A., Han J., Lu J.P., *Phys. Rev. Lett.* **85**, 1706 (2000)
- [6] Larciprete R., Petaccia L., Lizzit S., Goldoni A., *Phys. Rev. B* **71**, 115435 (2005)
- [7] Rauf H., Pichler T., Knupfer M., Fink J., Kataura H. *Phys. Rev. Lett.* **93**, 096805 (2004)
- [8] Jo C., Kim C. and Lee Y.H., *Phys. Rev. B* **65**, 035420 (2002)



- [9] Liu X., Pichler T., Knupfer M., Fink J., *Phys. Rev. B* **67**, 125403 (2003)
- [10] Suzuki S., Maeda F., Watanabe Y., Ogino T. *Phys. Rev. B* **67**, 115418 (2003)
- [11] Hartwigsen C., Witschel W., Spohr E., *Phys. Rev. B* **55**, 4953 (1997)
- [12] Ishii H. *et al.*, *Nature* **426**, 540 (2003)
- [13] Mintmire J.W. and White C.T., *Phys. Rev. Lett.* **81**, 2506 (1998)
- [14] Posternak M., Baldereschi A., Freeman A.J., Wimmer E., Weinert M., *Phys. Rev. Lett.* **50**, 761 (1983)
- [15] Kane C., Balents L. and Fisher M.P.A., *Phys. Rev. Lett.* **79**, 5086 (1997)
- [16] Bockrath M., Cobden D.H., Lu J., Rinzler A.G., Smalley R.E., Balents T., McEuen P.L., *Nature* **397**, 598 (1999)

Figure 3. Log-log representation of the photoemission spectra measured near the Fermi energy on pristine and Li doped SWNTs. The fits up to 0.2 eV provide the α values plotted vs. the Li/C ratio in the bottom inset. The bottom inset also displays the best fit curve [solid] for the α values, obtained with a power law decay function [dots] plus a Gaussian distribution [dashes]. In the top inset the valence band shapes measured on pristine [rescaled] and doped [Li/C=0.05] SWNTs are compared.

BOTTOM-UP FABRICATION OF CARBON-RICH SILICON CARBIDE NANOWIRES BY MANIPULATION OF NANOMETER-SIZE ETHANOL MENISCI

> M. Tello, N.F. Martínez, M.S. Martín-González and R. García

Instituto de Microelectrónica de Madrid, CSIC, 28760 Tres Cantos, Madrid, SPAIN

> J.A.M. Gago

Instituto de Ciencia Materiales de Madrid, CSIC, Campus Cantoblanco, 28049 Madrid, SPAIN

> L. Aballe, A. Barinov and L. Gregoratti

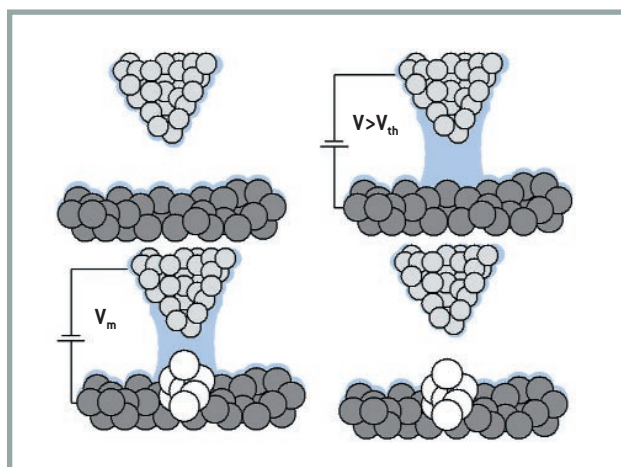
Sincrotrone Trieste S.C.p.A., S.S. 14 km 163.5, in AREA Science Park, 34012 Trieste, ITALY

The development of nanometer-scale lithographies is the focus of an intensive research activity because progress on nanotechnology depends on the capability to fabricate, position and interconnect nanometer-scale structures. Here we describe an atomic force nanolithography based on the spatial confinement of an electrochemical reaction within a nanometer-size ethanol meniscus. The meniscus is induced by the application of an electrical field. We show, by spatially resolved photoemission spectroscopy, that the nanostructures are made of carbon-rich SiC. The nanolithographic possibilities are illustrated by the fabrication of nanowires with widths and positioning below 45 nm, both singly or forming arbitrarily shaped networks.

The nanolithography is based on the ability to form and manipulate the properties of ethyl alcohol nanometer-size bridges. The ethanol bridge is formed by the application of an electrical field between a n-doped silicon tip and a silicon surface [1]. Once an ethanol nanocell has been formed, a voltage pulse drives the ethanol molecules to a silicon (100) interface where the electrochemical reaction occurs. The experimental set-up consists of a conductive dynamic AFM, which is enclosed in a chamber filled with N_2 and CH_3CH_2OH vapors. A voltage pulse applied between tip and sample condensates the vapor underneath the AFM tip, which gives rise to the formation of a nanometer-size liquid bridge. Tip-surface separation, voltage strength and pulse duration controls the meniscus size and hence

Figure 1. Formation of a nanometer-size ethanol meniscus. The meniscus is induced by the application of an electric field. This requires the application

of a voltage above a threshold value. Once the meniscus is formed, the same or another voltage pulse drives the chemical reaction inside the nanocell.



the size of the electrochemical cell, which in turn will control the nanostructure size [2].

The presence of four different chemical elements in the nanocell (C, O, H and Si) gives some uncertainty over the chemical composition of the formed structures. Similarities with AFM nano-oxidation experiments would suggest the formation of a silicon oxide [3]. However, exposure of the nanostructures to HF vapors did not remove them, which indicates the absence of silicon oxide. To determine quantitatively the chemical composition we have performed photoemission spectromicroscopy experiments in a synchrotron radiation facility. A series of rectangular structures of several microns in size were generated. AFM images of those structures reveal two major rectangles surrounded by smaller structures, all of them fabricated under the same conditions (Figure 3a). The height of the structure varies from 6 nm at the edges to 14 nm at the center. Photoemission microscopy images of those structures are shown in Figure 3b. To record them, the electron analyzer was tuned to the kinetic energy of the C 1s core-level orbital. The lighter regions (more emission from C 1s orbitals) matched the position of the AFM fabricated structures while the darker regions correspond to the silicon surface. This image was taken with a spatial resolution of about 200 nm (pixel size) [4].

The X-ray photoemission (XPS) spectra recorded on the center of the upper structure reveals two well-defined peaks (Figure 3c). The higher signal is centered at the C 1s core-level binding energy (~ 284 eV), while the smaller peak corresponds to the emission from the Si 2p core level (~ 101 eV). The other minor features in the spectra are easily associated with other core levels or multiple electron excitations. A higher resolution spectrum on the C 1s shows the peak centered at 284.2 eV (Figure 3d). The experimental data points were fitted and deconvoluted into three components, which are shown together with the best fit obtained. In the deconvolution process, Lorentzian and Gaussian widths of 190 meV and 1 eV respectively were used. The binding energies of the components are 284.8, 284.1 and 283.4 eV. Those components can be assigned to C-C sp^2 orbitals such as those in graphite,

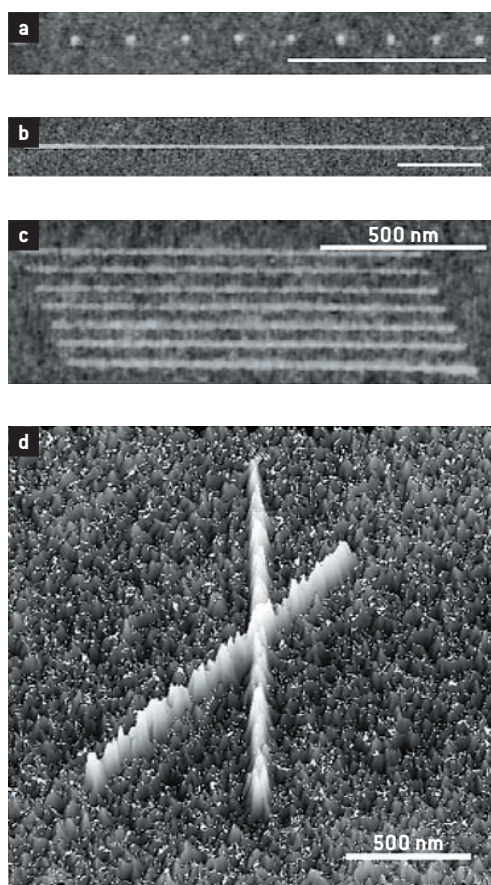


Figure 2. AFM images of nanostructures fabricated in an ethyl alcohol nanocell.

(a) Series of nanodots spaced 220 nm apart. Width range 40-60 nm.

(b) Single nanowire.
(c) Parallel array of nanowires. The wires are placed 70 nm part with an average width of 45 nm.

(d) Interconnected nanowires. The average height of the above structures is 2 nm. Bar 1 μm unless otherwise stated.

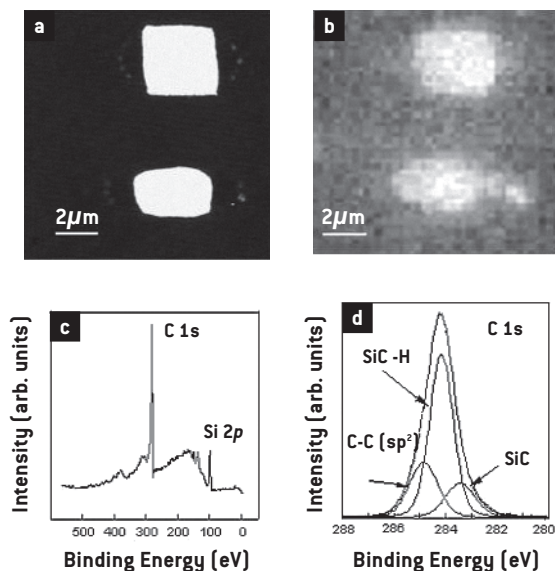
hydrogenated SiC (Si_3C-H environment) and SiC, respectively. The formation of SiC and the incorporation of hydrogen in the compound is also supported by the study of the core level shifted components of the Si 2p photoemission peak (not shown). The broad and symmetric peak at 2.3 eV higher binding energies than the Si 2p peak in bulk silicon corresponds to the SiC energy. Furthermore, we have performed in-situ measurements of some reference samples during the same experimental run. For instance, C 1s from a highly oriented pyrolytic graphite sample was measured and found to give a sharp peak at 284.8 eV.

In Figure 3d the intensity ratio C:Si deviates from the 1:1 stoichiometry towards a C-rich SiC:H (2.5:1). This could be due to either a C-rich surface termination or to a substitution of some Si atoms by H. The presence of oxygen in the structures has been disregarded because the low intensity of the oxygen O1s peak. Furthermore, the presence of oxygen in SiC gives components at 104-106 eV, which have not been observed in these experiments.

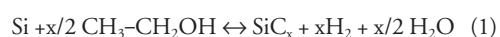
Figure 3. Topographic and spectroscopy images of the fabricated structures.

(a) AFM image of two rectangular structures. The height of the structure varies from 6 nm at the edges to 14 nm at the center. **(b)** XPS image of the fabricated structures taken at the energy of the C 1s core level. **(c)** XPS spectrum

recorded in the middle of the upper rectangle. Similar spectra were obtained in the other points of upper and lower rectangles. **(d)** C 1s core-level photoemission spectrum of a nanostructure. The three deconvolutions are also plotted. Thick solid line represents the fit and the solid points the experimental data.



The overall chemical reaction leading to the formation of a carbon rich SiC could be as follows



where the x reflects the non-stoichiometric character of the formed SiC compound.

Silicon carbide is a wide band gap semiconductor with good thermal conductivity and high electrical breakdown field. The nanolithographic process developed here allows the fabrication of carbon-rich silicon carbide structures that in combination with silicon oxide barriers could allow the development of high performance nanometer-size transistors and sensors.

Finally, we would like to emphasize that this process opens a general method for a bottom-up fabrication of nanomaterials based on the spatial confinement of a chemical reaction within a nanometer-size meniscus. Menisci of different liquids can be formed which would allow to produce a large variety of nanostructure compositions that are easily addressed, positioned and amenable of precise electrical and chemical characterization.

References

- [1] Tello M. and García R., *Applied Physics Letters* **83**, 2339 (2003)
- [2] Calleja M. and García R., *Applied Physics Letters* **76**, 3427 (2000)
- [3] Lazzarino M. et al., *Applied Physics Letters* **81**, 2842 (2002)
- [4] Tello M. et al., *Advanced Materials* **17**, 1480 (2005)

NANOGRAFTING AS A TOOL FOR THE FABRICATION OF NANO-BIOSENSORS AND THE STUDY OF BIOMOLECULES IN CONSTRAINED GEOMETRIES

> **L. Casalis**

Sincrotrone Trieste S.C.p.A., S.S. 14 km 163.5, in AREA Science Park, 34012 Trieste, ITALY

> **F. Bano**

*Sincrotrone Trieste S.C.p.A., S.S. 14 km 163.5, in AREA Science Park, 34012 Trieste, ITALY
International Center for Theoretical Physics (ICTP), Strada Costiera 11, 34100 Trieste, ITALY*

> **N. Bahar**

*Physics Department, University of Trieste, Piazzale Europa 1, 34127 Trieste, ITALY
International School of Advanced Studies (SISSA-ISAS), Via Beirut 2-4, 34014 Trieste, ITALY*

> **M. Castronovo**

*Physics Department, University of Trieste, Piazzale Europa 1, 34127 Trieste, ITALY
TASC Laboratory, CNR-INFM, S.S. 14 km 163.5, in AREA Science Park, 34012 Trieste, ITALY*

> **M. Dell'Angela**

Physics Department, University of Trieste, Piazzale Europa 1, 34127 Trieste, ITALY

> **R. Hudej**

*Sincrotrone Trieste S.C.p.A., S.S. 14 km 163.5, in AREA Science Park, 34012 Trieste, ITALY
International School of Advanced Studies (SISSA-ISAS), Via Beirut 2-4, 34014 Trieste, ITALY*

> **D. Scaini**

*Sincrotrone Trieste S.C.p.A., S.S. 14 km 163.5, in AREA Science Park, 34012 Trieste, ITALY
Physics Department, University of Trieste, Piazzale Europa 1, 34127 Trieste, ITALY*

> **G. Scoles**

*Sincrotrone Trieste S.C.p.A., S.S. 14 km 163.5, in AREA Science Park, 34012 Trieste, ITALY
International School of Advanced Studies (SISSA-ISAS), Via Beirut 2-4, 34014 Trieste, ITALY
Princeton University, Chemistry Department, Princeton, NJ 08540, USA*

Scanning probe microscopy (SPM) and in particular atomic force microscopy (AFM) are being increasingly used for applications in nanotechnology, in particular in the field of biomaterials and molecular electronics. AFM can easily be operated at ambient conditions and/or in a liquid environment, often a requirement in bio-science. It also offers the unique capability of manipulating molecules on surfaces at the nano-scale, while simultaneously measuring correlations between topography and other mechanical or physical-chemical properties of the system (i.e. friction, compressibility, electron transport, etc.).

The possibility of nano-manipulating complex molecules, such as DNA and proteins, makes AFM an optimal tool for fabri-

cating and studying nano-biosensors for molecular recognition in genetic expression and proteomics. On the other side, fabrication of controlled nano-scale metal-molecule-metal junctions, through nano-manipulation, enables the study of the mechanisms of charge transport, a crucial issue in molecular electronics. By adding a bias to a couple of nano-electrodes when organic materials are contained between them, and measuring the current tunneling through the gap, the “conductivity” of the junction can be obtained. Such experiments can shed light on the fundamental mechanisms of electron tunneling.

In the Nanostructure Laboratory at ELETTRA we currently fabricate molecular nanostructures by using a technique called nano-

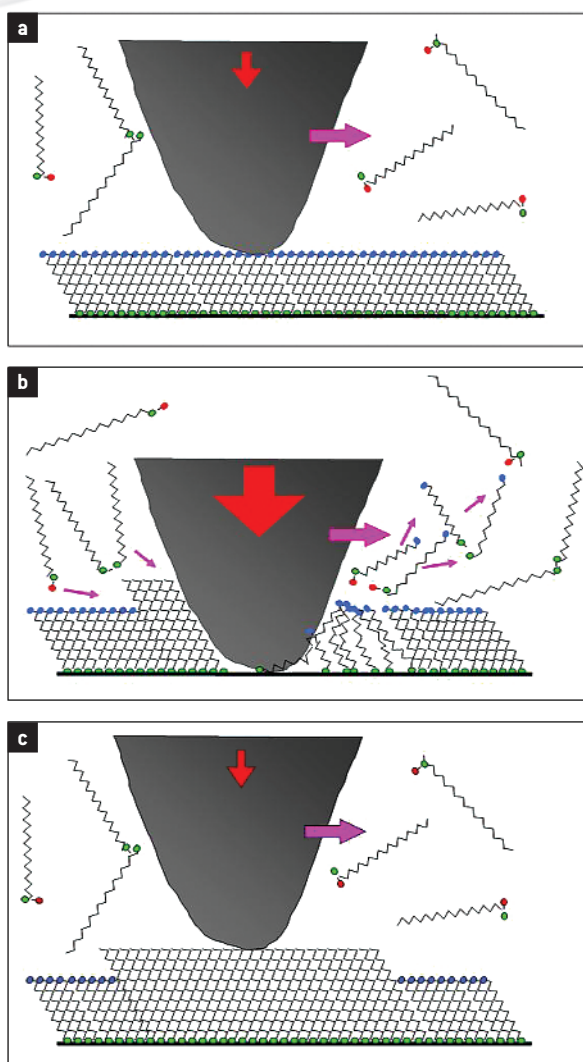


Figure 1. Schematic diagram illustrating the basic steps of the nanografting lithography technique.

grafting, first introduced by Gang-Yu Liu at Wayne State University in 1997 [1]. Nanografting is an AFM-assisted lithographic technique, which consists of locally substituting molecules of a self-assembled monolayer (SAM) with a different type of molecules. This is obtained by pressing the tip of the AFM at high load onto the SAM in presence of a solution containing the substituting molecules. As a result, nanopatterns of new molecules are embedded in a carpet of the original SAM molecules: in this way, properties of patterned molecules can be differentially measured relatively to the ones of the surrounding SAM strongly reducing systematic errors.

In our nanografting experiments we start from a SAM of the well studied and easy to prepare alkanethiol molecules ($\text{CH}_3(\text{CH}_2)_{n-1}\text{SH}$) on gold films evaporated on mica. The

AFM is operated in a liquid cell, with a solution containing the molecules to be released on the surface. Such molecules must interact with the gold film with the same S-Au chemistry of the alkanethiol SAM. In the case of proteins or DNA, they must be properly functionalized in order to contain a SH group which allows bonding to the gold surface. The surface (see Figure 1a) is imaged at low force (below 1 nN, corresponding to pressures of about 0.01-0.1 GPa), for a topographical characterization; once a nice area for nanofabrication is selected, the load is increased by one order of magnitude or more, causing a local displacement of the SAM molecules from the gold substrate, and their substitution with the molecules present in solution (Figure 1b); finally, the surface is imaged again at low force, and nanostructures are characterized from topography measurements (Figure 1c).

We apply nanografting to many different molecular systems. In the case of proteins, we apply the technique to understand protein-protein interactions, to study mechanical properties of membrane proteins and protein folding. In the case of DNA (or RNA), we demonstrated the possibility of designing a device where different DNA nanostructures, each one with a specific single stranded DNA sequence, are immobilized at specific addresses on the surface [2]. Such a device contains a much smaller number of addresses with respect to the currently manufactured micro-arrays (few hundreds versus hundreds of thousand), but has a much higher density of addresses. It is more sensitive, and can analyze a much smaller quantity of DNA than micro-arrays. It could be successfully employed in gene expression analysis in case of poorly expressed genes.

An AFM topographic image of a device containing 9 addresses with three different single stranded DNA sequences in a C_{18} SAM matrix is shown in Figure 2, together with the height profiles. The measured heights are in good agreement with the expected values for single stranded DNA standing up on the gold surface: in the case of the DNA central sequence, for instance (a 18mer with a C_6 thiol linker), we measure an height of $5.4 (\pm 0.2)$ nm with respect to the C_{18} SAM matrix. Taking into account

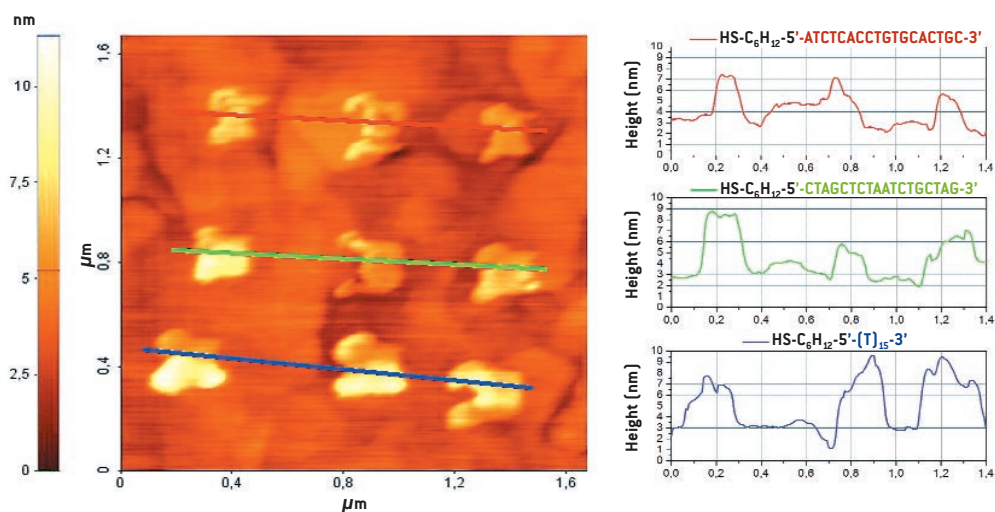


Figure 2. Single stranded DNA nano array fabricated with three different DNA sequences. Each nanopatch is a square of 150 nm x 150 nm. Height profiles across the nanopatches are used to check the structure of DNA molecules inside the patch.

the height of $2.2 (\pm 0.2)$ nm measured for the C_{18} SAM, the measured height of the DNA in the nanostructures is comparable to the length of the fully stretched DNA, which is about 8.4 nm.

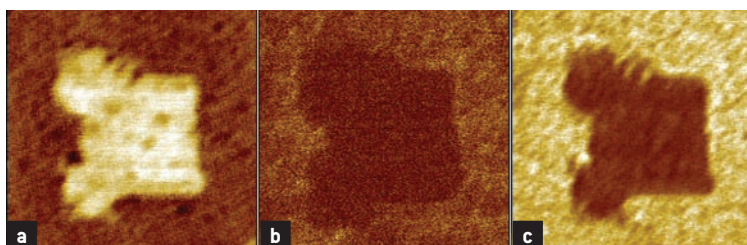
With this method, several hours are needed to produce a matrix with 100 different DNA addresses. In order to allow manufacturing of the device at a reasonable cost, the master copy produced by nanografting must be then efficiently duplicated. This can be realized by coupling our technique with a patent pending idea recently developed by Francesco Stellacci and coworkers at MIT [3]. This technique mimics the most efficient duplication method provided by nature, namely the DNA/RNA information transfer. The idea is to let single stranded DNA hybridize with the complementary strand, which is in turn functionalized with a thiol linker that points out from the surface; a second gold surface is brought in contact with the film, to allow bonding to the thiols of the complementary strands; by varying the pH or the temperature of the system, DNA is let de-hybridize, while the two gold surfaces are brought apart. In such way, the master copy is duplicated into its negative copy. The same master copy can be duplicated several times, and each negative copy is itself a master copy for subsequent duplications.

At present, we are working at the realization of the copies and the optimization of

the parameters of the copying process. In order to optimize the copying efficiency, we need to optimize the hybridization efficiency, by controlling the density of single stranded DNA molecules in the nanopatches. Nanografting is in fact known to accelerate the kinetics of formation of alkanethiol SAMs and to facilitate higher packing. In the case of DNA nano array, high packing could mean sterical hindrance to the hybridization process, and as a consequence reduced efficiency of the copying process itself.

One more example of application of AFM to nanotechnology is the study of the correlations between mechanical properties, such as friction or adhesion between two adjacent surfaces, and the structure of the surfaces. While friction at the macro-scale can be reduced by polishing the surfaces and by the use of lubricants, when the dimension of the surfaces is reduced to micro- or nano-scale, for example in micro-machines, these techniques become unusable. In order

Figure 3. (a) Topography image of a C_{18} 150 nm x 150 nm nanopatch in a $C_{11}OH$ SAM matrix. (b) Frictional image of the nanopatch in water. (c) Frictional image of the nanopatch in 2-butanol.



to develop new ways of controlling friction, it is extremely important to understand how friction depends on the atomic structure of the interface.

It is well known that, in the case of alkanethiol SAMs, friction is function of the chain length and of the nature of the terminal group. Up to a certain limit, longer chains exhibit lower friction, because they are better packed than shorter ones, due to the stronger chain-chain Van der Waals forces. This closed packing prevents the tip from penetrating the layer, and opening channels for energy dissipation, such as bending of the molecules or formation of defects in the chains.

By nanografting, we can correlate on the same substrate, by using the same tip, frictional properties of patches of alkanethiol with, for instance, hydrophobic termination (i.e. CH_3), and of the outside carpet of alkanethiol with hydrophilic termination (i.e. OH), in liquid, as a function of the nature of the used solvent. One example is the study of nanopatches of C_{18} inside an undecanethiol ($\text{OH}(\text{CH}_2)_{11}\text{SH}$, briefly C_{11}OH) SAM matrix, in water and in alcohol (2-buthanol). Height measurements from topographic images confirm the expected height of 2.2 nm of the C_{18} molecules in the nanopatches (see Figure 3a). Preliminary data of the frictional properties of the system are shown in Figures 3b and 3c: frictional images respectively in water and 2-buthanol show a good contrast between the patch and the outside SAM, which allows for differential friction analysis. Friction between the silicon tip and the CH_3 -termi-

nated molecules is not expected to change when the solvent is changed, because the CH_3 groups do not interact with both solvents. The contrast in friction between the patch and the OH-terminated SAM, however, changes by changing the solvent, and in particular it is lower when the measurements are performed in water. This result points to a reduction of friction at the OH hydrophilic surface in presence of water, which can be explained by assuming the presence of an organization of water molecules at the tip-SAM interface. The occurrence of an icy-like state of water at the OH surface is a particularly interesting phenomenon, which needs more data to be addressed.

We have shown here how, by using nanografting, nanostructures of different type of even complex molecules, such as DNA or proteins, can be easily fabricated at high resolution. Moreover, with the same AFM that we use for fabricating the nanostructures, different physical properties of such spatially confined molecules can be investigated simultaneously in a systematic way.

References

- [1] Xu S., Liu G.Y., *Langmuir* **13** (2), 127 (1997)
- [2] Dell'Angela M., Scaini D., Castronovo M., Hudej R., Casalis L. and Scoles G., in preparation
- [3] A. Amy Yu A.A., Savas T.A., Taylor G.S., Giuseppe-Elie A., Smith H.I. and Stellacci F., *Nano Letters* **5**(6), 1061 (2005)

MATERIAL SCIENCE

ELETTRA has a wide range of beamlines catering to the scientific community involved in the study of materials and covering the complete spectrum of techniques, including those based on spectroscopy, diffraction, scattering and microscopy. Spectroscopy, such as photoelectron spectroscopy, X-ray absorption and emission spectroscopies, can be carried out using both linearly polarized and elliptically polarized lights covering an energy range starting from a few eV to more than thousand eV. This allows one to study the electronic and magnetic structures of systems in great detail, thereby contributing deeply to a wide range of fields, such as surface science, magnetism, and strongly correlated electron systems. Due to the availability of a large number of specialized end-stations, it is possible to carry out many sophisticated experiments using these spectroscopic techniques including three dimensional band-mapping and magnetic circular dichroic studies. ELETTRA's unique capabilities in the area of microscopy with the use of its three sophisticated microscopy beamlines, supporting experiments investigating phenomena involving different length-scales are already well-known and have been highlighted in previous years' publications. Over the years, there is a clearly noticeable trend of growing applications from the field of nano-science and technology at various ELETTRA's beamlines. SAXS beamline, providing both scattering and diffraction information, has turned out to be a work-horse for material science, in particular in the area of nano-technology. We highlight this aspect by providing some details of a few selected experiments performed and results obtained from the SAXS beamline during the last one year. For example, the work carried out at this beamline provides us with the understanding of the detailed structures of mesoporous materials, helping to design hybrid materials with important and interesting properties, such as ultra-low k dielectric materials (see Innocenzi et al., JACS) with possible applications in photonics or in microelectronics and ones based on multi-metallic oxides to utilize the diverse functionality of such materials (see Grosso et al., Nature Materials). In another interesting application (see Gupta and Fratzl, PRL), studies carried out here provided us an understanding of why biomineralized tissues have such high stiffness and toughness.

D.D. Sarma

FIBRILLAR DEFORMATION IN MINERALIZED TENDON

> H.S. Gupta, P. Fratzi

Max Planck Institute of Colloids and Interfaces, Department of Biomaterials, 14424 Potsdam, GERMANY

> P. Messmer, P. Roschger, K. Klaushofer

Ludwig Boltzmann Institute of Osteology, Vienna, AUSTRIA

> S. Bernstorff

Sincrotrone Trieste S.C.p.A., SAXS Beamline, S.S. 14 km 163.5, in AREA Science Park, 34012 Trieste, ITALY

INTRODUCTION

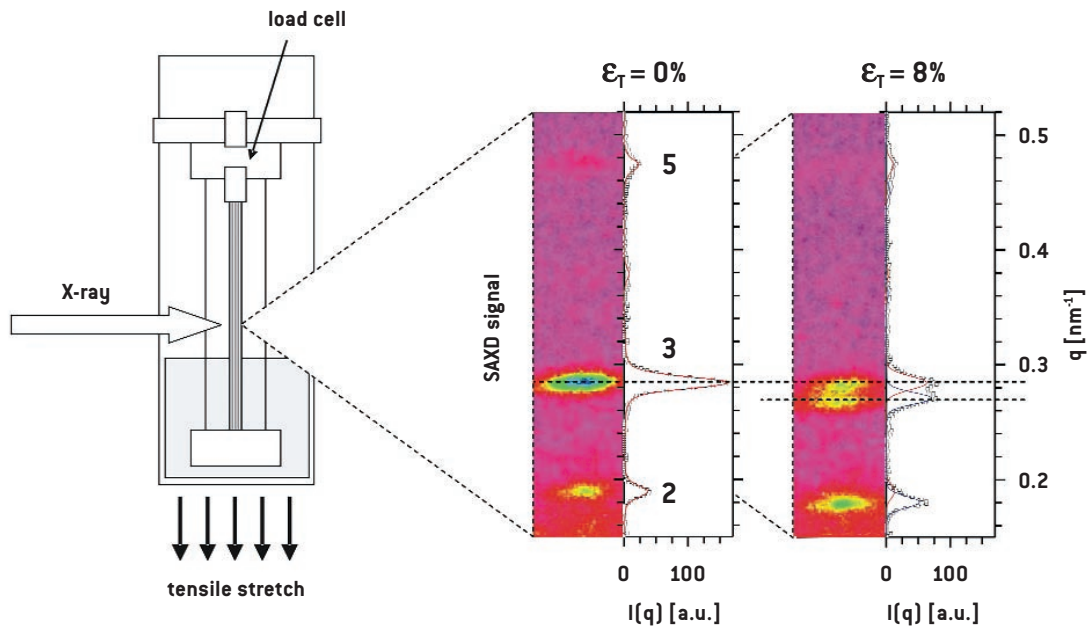
How the structure of bones and other calcified tissues at the supramolecular and lamellar level results in a combination of high stiffness and high work of fracture of biomineralized tissues is a question whose answer is of considerable scientific interest. From a clinical point of view, one would like to know how to prevent or minimize catastrophic fractures occurring as a result of bone diseases and aging, and from a materials science point of view, how to make synthetic composites that use natural design principles to achieve high structural stability. As is well known, bone is a hierarchically structured material from the nanometer to the organ level [1]. The phenomenon of bone fracture depends on the structure at all the different length scales, from changes in the mineralized fibril structure at the nanometer level [2] to alterations at the organ level structure [3] at the scale of 100 μm - 1 mm. Nonetheless, very little is still known about the actual deformation mechanisms in mineralized collagen fibers under application of external load.

To study this question, we used the parallel fibered mineralized turkey leg tendon (MTLT) as a model for parallel fibered mineralizing collagen. This system has been widely used for studying the early stages of calcification, since it remains uncalcified up till 10-12 weeks of age, and then starts mineralizing in a proximal to distal manner with time. Because of the increasing load that the leg tendon has to bear with increasing age of the bird, the origin of the calcification has been suggested to be stress - induced at the

molecular level [4]. By its parallel fibered nature as well as variable overall mineralization, MTLT is suitable for both uniaxial tensile testing as well as for producing a 1D series of Bragg reflections from the 67 nm collagen D-period. Percentage changes in this D-period are a measure of the fibrillar strain, which can be tracked *in-situ* during mechanical testing during time resolved small angle X-ray diffraction. In unmineralized collagen from rat tail tendon, *in-situ* testing has shown that the tissue strain is a mixture of fibrillar strain as well as extrafibrillar shearing [5]. Recently we have shown that a similar phenomenon occurs also in parallel fibered bovine bone [6].

MATERIALS AND METHODS

Mineralized digital flexor tendons were dissected from freshly slaughtered farm grown turkeys obtained from a commercial Austrian turkey farmer. Turkeys of 12, 15, and 24 weeks age were used, to cover a broad range of mineralization. Adhering soft tissue was carefully removed using scrapers and scalpels. Samples were kept wet in phosphate buffered saline (PBS) throughout sample preparation, storage and testing. For preparation of the tensile test samples, the tendons were carefully clamped between two Plexiglas sheets and sectioned parallel to their long axis with a Leica SP1600 inner hole saw (Leica Microsysteme GmbH, Germany). The sheets so obtained were split parallel to their fiber axis using a very fine scalpel. Resulting sample dimensions were typically 200 - 400 μm \times 500 - 1000 μm \times



5 - 10 mm. Sample dimensions were measured both from the vertical drive knob on the microtome as well as with a pressure sensitive micrometer and under a light microscope. For preparing the samples in the tensile test configuration, specially prepared quadratic stainless steel metal pieces were sandblasted manually and attached to a test frame. A dental glue (Bond It!TM primer and Flow-It FlowableTM amalgam (Jeneric - Pentron GmbH, Germany) was used to fix the samples to the metal clamps.

A specially designed tensile testing apparatus was used to carry out the test with the samples in a wet state. A load cell (A.L. Design Inc., Buffalo, NY, USA) with maximum load 12.5 kg was mounted on one fixed grip, while the other was mounted on a sliding guide rail driven by a DC - encoder motor (M-125.10, Physik Instrumente, Germany). The sample was half immersed in physiological phosphate buffered saline (PBS) during the test, to keep it wet. User written software was used to control the tensile test setup.

Synchrotron small angle X-ray diffraction (SAXD) measurements were carried out at beamline BL 5.2 (SAXS), Sincrotrone Tri-

este, Trieste, Italy, concurrently with tensile testing (Figure 1). Samples from all three ages were tested. Frames were recorded on a 2D CCD detector (Bruker AXS GmbH) at a sample - detector distance of 257.5 cm and beam wavelength $\lambda = 0.154$ nm. After correction for the empty beam background, the frames were integrated along the vertical direction (direction of the fibril axis). Peak-Fit version 4 (SPSS Inc, USA) was used to carry out the fitting of the integrated intensity.

Selected tested samples were embedded in polymethylmethacrylate (PMMA) and sectioned perpendicular to the fiber axis. The samples were carbon coated and then imaged in the quantitative backscattered electron mode (qBEI) in a scanning electron microscope (SEM), to reveal the spatial distribution of the mineral content at the micron level.

RESULTS

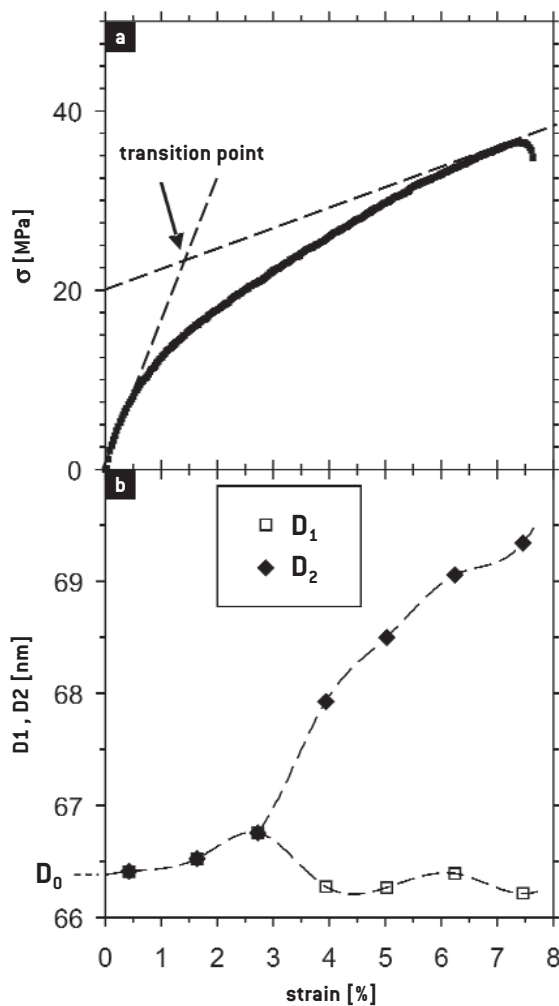
In-situ tensile testing with small angle X-ray diffraction: Time resolved measurements of the changes in fibrillar D-period and stress with increasing tissue strain showed a dis-

Figure 1. Schematic of the *in-situ* tensile testing setup combined with small angle X-ray diffraction (SAXD) at ELETTRA. On the right are sections of the two-dimensional SAXD patterns, showing the Bragg reflections arising from the collagen D-periodicity, as well as the integrated intensity profiles.

tinct correlation. For low tissue strain ϵ_T , the tissue stress increased linearly with a (relatively) high elastic modulus, but for $\epsilon_T \geq 2 - 3\%$, the effective modulus (slope of the stress - strain curve) decreased. Simultaneously, for low strains, the fibril D-period increased, but for larger strains, the fibril diffraction pattern showed two distinct sets of Bragg reflections corresponding to two distinct fibril elongations in the tissue. The first (D_1) relaxed back to near its stress - free value D_0 , while the second (D_2) increased at a much faster rate up to values of 70 nm (Figure 2).

Figure 2. Change in tissue stress and fibril D-period with applied tissue strain, showing inhomogeneous fibrillar elongations in the tissue for strains $\geq 2 - 3\%$.

Back scattered electron imaging of tendon microstructure. qBEI measurements showed a highly inhomogeneous mineralization distribution at the micron level. Specifically, overview images of the tendon showed light (highly mineralized) regions coexisting with dark (unmineralized) regions, like a two -



phase system (Figure 3(a)). At higher magnifications, this inhomogeneity resolved into two groups of fiber bundles, one group highly mineralized and the other much less mineralized (Figure 3(b)). The typical diameter of the fiber bundles was between 2 to 4 μm , and the bundle consisted of mineralized fibrils (which are too small to be resolved in the SEM). The total area fraction of unmineralized tissue decreases with age of the bird, going from 39.7% (12 week) to 3.5% (24 week). However, if the mineralized tissue alone is considered, then the difference in the degree of mineralization is not so different from human trabecular bone. Indeed, the mineral weight percentage of the mineralized tissue is about 51.4%, compared to about 55.5% in human trabecular bone [7].

DISCUSSION AND CONCLUSION

To interpret our results in terms of microstructural deformation mechanisms, a simple fiber composite model can be constructed at the tissue level (Figure 3(c)), where unmineralized, extensible collagen fiber bundles (gray) coexist with stiff, inextensible mineralized collagen fiber bundles (white). When the tissue is stretched, below the fracture strain of the mineralized fiber bundles, homogeneous elongation occurs. For strains above the fracture strain of the mineralized fiber bundles, the mineralized fiber bundles break and the unmineralized fibers bear the remaining load. As a result, the effective modulus decreases, but since the unmineralized fibers are more extensible, the tissue does not break as a whole until the failure strain of the unmineralized fibers is reached. In this way, the tendon achieves a high stiffness as well as a high work to failure by means of a novel micron level failure mechanism.

In conclusion, our investigation into the deformation mechanisms of parallel fibered mineralized tendon from turkey leg tendon established, firstly, the feasibility of applying *in-situ* tensile testing combined with synchrotron X-ray diffraction for studying fibrillar deformation in mineralized tissues. Secondly, a novel two step deformation mechanism was demonstrated to occur in MTLT, whereby the tissue maintains a high stiffness in the low working strain regime

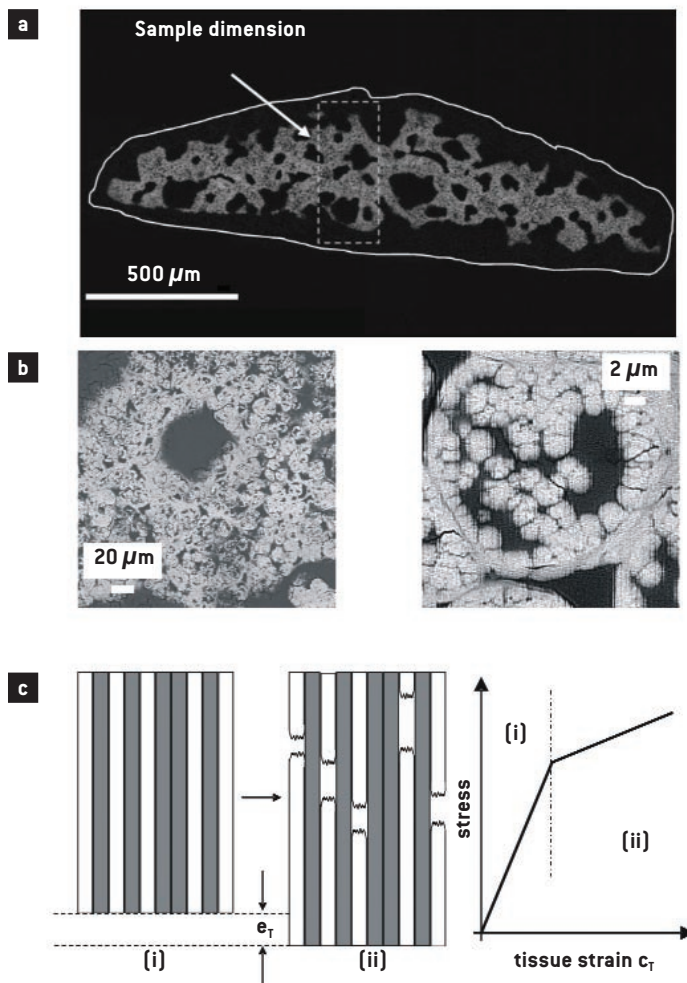


Figure 3.

(a) SEM image of an embedded cross-section of MTLT. Lighter regions are more mineralized, and darker regions are less mineralized. **(b)** Higher magnification images of MTLT, showing the discrete

unmineralized and mineralized fiber bundles. **(c)** Fiber composite model of fiber fracture, showing the mineralized [white] fibers breaking before the unmineralized [gray] fibers for large tissue strains.

but requires a large amount of work to fracture, by means of a biphasic failure mechanism [8].

References

- [1] Weiner S. and Wagner H.D., *Annual Review Material Science* **28**, 271 (1998)
- [2] Landis W.J., *Bone* **16**, 533 (1995)
- [3] Power J. et al., *Osteoporosis International* **16**, 1049 (2005)
- [4] Landis W.J. et al., *Journal of Bone and Mineral Research* **10**, 859 (1995)
- [5] Puxkandl R. et al., *Philosophical Transactions of the Royal Society of London B* **357**, 191 (2002)
- [6] Gupta H.S. et al., *Nano Letters*, in press
- [7] Roschger P. et al., *Bone* **32**, 316 (2003)
- [8] Gupta H.S. et al., *Physical Review Letters* **93**, 158101 (2004)

SELF-ASSEMBLED HIGHLY-ORDERED MESOSTRUCTURED HYBRID FILMS

> **Stefano Costacurta, Paolo Falcaro**

Dipartimento di Ingegneria Meccanica, Settore Materiali, Università di Padova, Via Marzolo 9, 35131 Padova, ITALY

> **Giovanni Mattei**

Dipartimento di Fisica "Galileo Galilei", Università di Padova, Via Marzolo 8, 35131 Padova, ITALY

> **Heinz Amenitsch**

Institute of Biophysics and X-ray Structure Research, Austrian Academy of Sciences, Schmiedelstrasse 6, 8042 Graz, AUSTRIA

> **Luca Malfatti, Tongjit Kidchob, Plinio Innocenzi**

Laboratorio di Scienza dei Materiali e Nanotecnologie, Nanoworld Institute, Dipartimento di Architettura e Pianificazione, Università di Sassari, Palazzo Pou Salid, Piazza Duomo 6, 07041 Alghero, Sassari, ITALY

INTRODUCTION

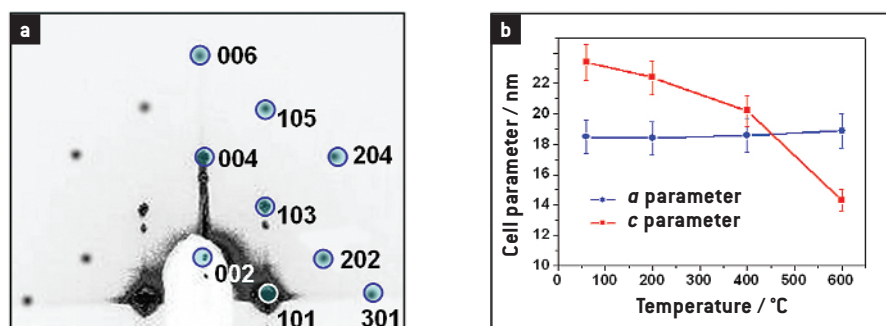
The research on hybrid mesoporous films has aroused great interest because of the prospective applications in advanced devices, for example as ultralow- k dielectric materials in microelectronics and as low refractive index materials in photonics. The synthesis of self-assembled silica films containing methyl groups has been reported in numerous publications over the past few years¹. The next step towards the fabrication of such mesoporous-based devices is the achievement of a thorough control on the properties of the material, especially a high and reproducible porosity order. Synchrotron small angle X-ray scattering (SAXS) has been largely used to study self-assembled mesostructured films deposited via dip-coating. This technique has revealed to be particularly effective to study the self-assembly mechanisms through which the organic micelles assemble to give rise to different organized mesophases. With the purpose to reach a higher order in the pore organization, in this work we have synthesized hybrid mesostructured films prepared by cohydrolysis and self-assembly of an optimized MTES-TEOS mixture that show large "crystal-like" domains. We were able to identify a new tetragonal mesophase in the final material by a synergic coupling of TEM and SAXS analysis.

EXPERIMENTAL

Pluronic F127 ($\text{OH}(\text{CH}_2\text{-CH}_2\text{O})_{106}(\text{CH}_3\text{CH}_2\text{O})_{70}(\text{CH}_2\text{CH}_2\text{O})_{106}\text{H}$), tetraethy-

lorthosilicate (TEOS), methyltriethoxysilane (MTES) and ethanol (EtOH) were purchased from Aldrich and used as received. Silicon wafers were employed as substrate. A stock solution was prepared, with molar ratios TEOS : MTES : EtOH : HCl : H₂O = 1 : 0.56 : 4.17 : 0.11 : 1.55. The solution was stirred for one hour to allow the hydrolysis of the silane units. A template solution was prepared, containing 1.3 g Pluronic F127, 15 ml EtOH and 1.5 ml HCl 5·10⁻³ M. Next, 7.7 ml were taken from the stock solution and added to the template solution. The resulting solution was then aged for one week. The final molar ratios were TEOS : MTES : EtOH : H₂O : HCl : F127 = 1 : 0.56 : 24.48 : 14.70 : 0.11 : 7.6·10⁻³. The substrates, previously cleaned with hydrofluoric acid, water, EtOH and acetone, were dip-coated in the aged solution. The relative humidity (RH) in the deposition chamber was set to 40%, the withdrawal speed was set to 15 cm·min⁻¹. Finally, the samples were thermally treated in air at different temperatures.

The mesostructures of the films were investigated using the high-flux grazing incidence small angle X-ray scattering (GI-SAXS) apparatus at the Austrian high-flux beamline of the electron storage ring ELETTRA taking for each image the average of 10 single acquisitions and different exposition time. The instrumental grazing angle was set maintaining an incident X-ray beam (wavelength 1.54 Å) smaller than 3°. From the



recording of the CCD detector the *out of plane* diffraction maxima were observed. Transmission electron microscopy (TEM) structural and compositional characterization was performed with a field-emission gun FEI TECNAI F20 SuperTwin FEG-(S)TEM microscope operating at 200 kV. The samples were prepared as cross-sections cutting the mesoporous films along two perpendicular directions with respect to the Si substrate in order to have access to different crystallographic projections of the mesostructures. To maximize the contrast between pores and matrix, the samples were investigated by acquiring TEM images in scanning mode (STEM).

RESULTS AND DISCUSSION

The synthesis of thin films via evaporation-induced self-assembly (EISA) typically yields organized porous structures whose porosity lies in the 2–50 nm range (mesopores). Since a 1-D X-ray diffraction pattern generally does not present a number of spots sufficient for the identification of the mesophase, 2D-SAXS techniques, using synchrotron light as X-ray source, are preferred for analysis of self-assembled films. However, up to now, a complete identification procedure has been seldom applied because of the difficult interpretation of SAXS patterns and the lack of a codified method. We have employed GI-SAXS to record four diffraction images, corresponding to samples thermally calcined at

60, 200, 400, and 600°C. To identify the mesostructure, we have used the GI-SAXS image at 200°C, because the several detected diffraction spots allowed an easier attribution of the phase with respect to the other patterns. To start the phase identification through simulation of the diffraction spots, we have used the fast Fourier transform of the STEM images of the sample calcined at 200°C (not shown in the figure), which suggested that the structure is body-centered tetragonal². To support the hypothesis of a tetragonal mesophase, we have simulated the diffraction patterns of the 200°C sample with CMPR software (B. Toby, NIST) using a body-centered tetragonal unit cell (BCT) with an $I4/mmm$ space group. The simulated spots well reproduced the GI-SAXS results: Figure 1a shows the CMPR simulation superimposed with the GI-SAXS image of the film calcined at 200°C. The experimental spots were obtained from different images taken varying the exposition times and then, using their original positions, merged into a low saturation level diffraction image. The reader can notice the more regular shape of the added spots. Applying the same procedure, we have identified the same tetragonal symmetry in the mesostructured samples calcined at 400 and 600°C.

A general phenomenon, observed in mesostructured films during thermal shrinkage, is the symmetry transition of the mesophase caused by the uniaxial contraction of the amorphous matrix along the direction

Figure 1.

(a) Correspondence between the simulated structure and the measured GISAXS images in MTES-TEOS films calcined at 200°C. **(b)** Variation of *a* (blue) and *c* (red) cell parameters as a function of thermal treatment. The lines are a guide for the eyes.

normal to the substrate. In several cases the low-temperature symmetry has been identified as a body-centered cubic structure (BCC) with space group $Im\bar{3}m$, arranged with the (110) face parallel to the substrate³. If the mesophase in our as-deposited film had $Im\bar{3}m$ symmetry with such orientation, after the thermal contraction we would observe, instead of tetragonal, an orthorhombic symmetry in the calcined samples. On the other hand, the BCT structure observed in samples treated at high temperature requires the starting mesophase to have equal or higher symmetry. Therefore, it is necessary to suppose that the as-deposited film has a different in-planar mesophase disposition on the substrate. The condition of coplanarity of the (001) face with the substrate implies the contraction of the c axis only, in accordance with the supposed symmetry of the shrunked mesophase. The CMPR simulated spots, generated on the basis of an $I4/mmm$ space group, were also in good agreement with the GI-SAXS image of the sample treated at 60°C.

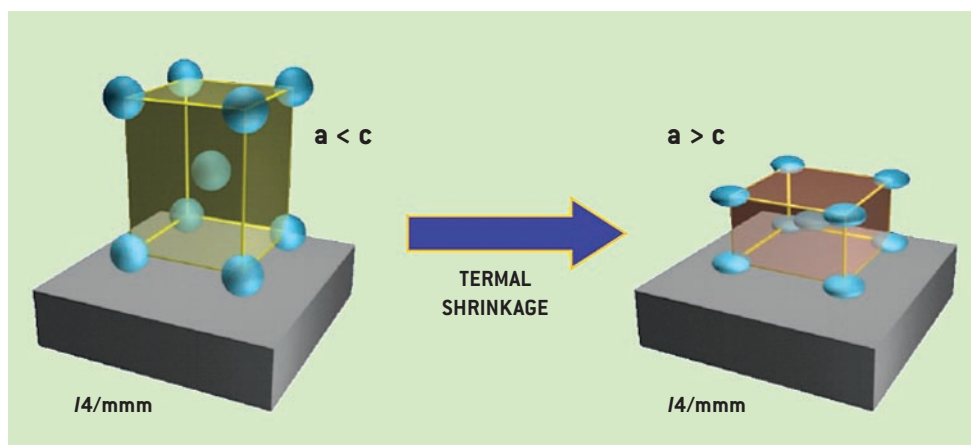
To support our phase identification, we have calculated the lattice constants of the different samples. The transition affecting the BCT cell ($I4/mmm$) with $a < c$, to a structure having the same symmetry but with $a > c$ is illustrated in Figure 2. The tetragonal cell is oriented with the (001) plane parallel to the substrate (c axis normal to the substrate); a decrease of the cell parameters takes place

as a function of the thermal treatment, markedly in the [001] direction perpendicular to the substrate, causing the shrinkage of the structure along this direction.

The effect of the shrinkage on the mesophase has been previously reported but, in this case, the different chemical composition of the starting solution implies fundamental differences in symmetry transition and in the thermal evolution³ of the deposited films. The presence of the methyl groups seems to play a fundamental role during the self-assembly process, modifying the packing of micelles inside the as-deposited film. The decrease of the cell parameters with increasing calcination temperatures (Figure 1b) is in accordance with the transition suggested: the a and b axes do not vary significantly within the experimental error, while the c axis shows a decrease from 23.4 nm at 60°C to 14.3 nm at 600°C, corresponding to a shrinkage of 39%.

The high degree of order reached in the MTES-derived self-assembled mesostructured films can be directly observed by TEM images. Dark-field cross-section STEM images of a sample treated at 350°C are shown in Figure 3a and 3b. The silicon substrate appears as a dark layer in the bottom part of the figure; the thickness of the film is 370 nm (± 5 nm). The film appears highly ordered with elliptical pores, due to the thermally induced shrinkage along the direction normal to the substrate. The extension

Figure 2. Sketch of the shrinkage observed in the $I4/mmm$ structure upon thermal treatment from 60°C to 600°C. The c axis is normal to the substrate.



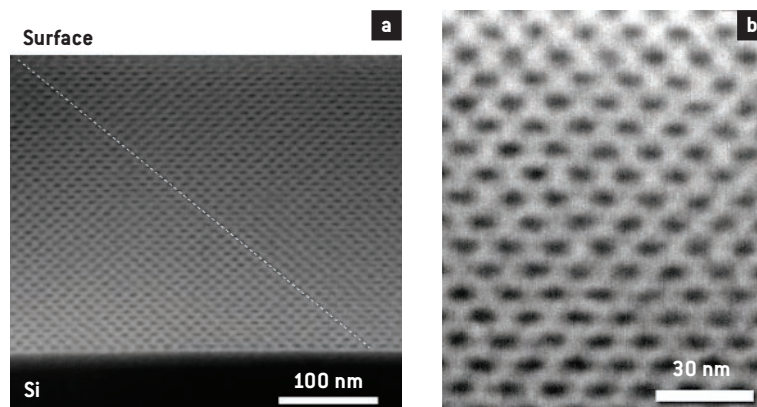


Figure 3. (a) Dark-field cross section STEM image of a sample treated at 350°C. The dotted line, oriented in the [011] direction, evidences the lack of defects in the investigated region. (b) Enlargement of a highly ordered area of the same sample.

of the ordered domains can be estimated in a micrometer scale. The structural order and the elliptical shape are clearly observed. The pore dimensions measured from the TEM images are 8.8 nm ($\sigma = \pm 0.9$ nm) along the major axis, parallel to the surface, and 4.8 nm ($\sigma = \pm 0.5$ nm) along the minor axis, perpendicular to the substrate, with a 1.8 ($\sigma = \pm 0.3$) ratio between the longer and shorter axes.

CONCLUSIONS

The reported one-pot synthetic strategy results in a simple and efficient way to obtain highly ordered hybrid silica films, with micron-scale domains. The use of MTES in the precursor solution yields films having a new tetragonal $I4/mmm$ periodic porosity, which is very well ordered throughout the whole thickness of the film. The approach that we have developed for structural data analysis, based on the combination of TEM, SAXS and diffraction pattern simulation, has revealed to be a very effective tool for unambiguous phase identification of mesoporous films.

References

- [1] De Theije F.K., Balkenende A.R., Verheijen M.A., Baklanov M.R., Mogilnikov K.P., and Furukawa Y., *Journal of Physical Chemistry B* **107**, 4280 (2003)
- [2] Falcaro P., Costacurta S., Mattei G., Amenitsch H., Marcelli A., Cestelli Guidi M., Piccinini M., Nucara A., Malfatti L., Kidchob T. and Innocenzi P., *Journal of American Chemical Society* **127**, 3838 (2005)
- [3] Falcaro P., Grosso D., Amenistch H. and Innocenzi P., *Journal of Physical Chemistry B* **108**, 10942 (2004)

PERIODICALLY ORDERED MESOPOROUS FILMS COMPOSED OF NANOCRYSTALLINE MULTIMETALLIC OXIDES

> David Grosso, Cédric Boissière, Clément Sanchez.

Chimie de la Matière Condensée, UMR UPMC-CNRS 7574, 4 place Jussieu, 75252 Paris 05, FRANCE

> Bernd Smarsly, Torsten Brezesinski, Nicola Pinna, Markus Antonietti

Max Planck Institute of Colloids and Interfaces, Research Campus Golm, 14424 Potsdam, GERMANY

> Pierre A. Albouy

Laboratoire de Physique des Solides, Université Paris-Sud, 91405 Orsay, FRANCE

> Heinz Amenitsch

Institute of Biophysics and X-ray Structure Research, Austrian Academy of Sciences, Schmiedlstr. 6, 8042 Graz, AUSTRIA

The integration of functional oxides into devices often requires the deposition into the form of thin crystalline films with a perfect control of the interfaces where electronic or spintronic exchange occurs. This control could be achieved through the preparation of mesoporous materials. In the present study, mesoporous thin films exhibiting crystalline walls of multimetallic solid state phases, have been prepared. Among these, perovskites as SrTiO_3 , $\text{Ba}_x\text{Sr}_{(1-x)}\text{TiO}_3$ or PbZrTiO_3 (PZT), $\text{Co}_x\text{Ti}_{1-x}\text{O}_{2-x}$, TiO_2 and MgTa_2O_6 are highly interesting in many “high-tech” domains (e.g. spintronics, piezoelectrics, nanomechanical adjustment, data storage, oxidic fuel cells, advanced photodecomposition devices or fuel-cells combustion). Since the preparation of these multimetallic oxides is already complicated (as accurate stoichiometry, highly mixable precursors, specific chemistry for each phase and high temperature of crystallisation are required), an additional control of the morphology at the mesoscopic level has turned out to be difficult to master. Here, we report on the synthesis of SrTiO_3 , MgTa_2O_6 and $\text{Co}_x\text{Ti}_{1-x}\text{O}_{2-x}$ ($0 < x < 0.30$) thin films with high homogeneity (optical transparency), distorted cubic based mesostructure, 35 vol% porosity (evaluated by ellipsometry) and close to 100 % nanocrystalline network with large available interfaces of about $100 \text{ m}^2/\text{g}$. These “ M_3NF ” materials were realised by following a simple and robust method combining the Chemical Solution Deposition

(CSD) technique with the EISA [1] approach in presence of a specific block-copolymer. Eventually, a careful crystallisation step allows a precise control of scaffolding and nanocrystal intergrowth. The mechanisms were carefully studied through specially designed X-ray synchrotron experiments.

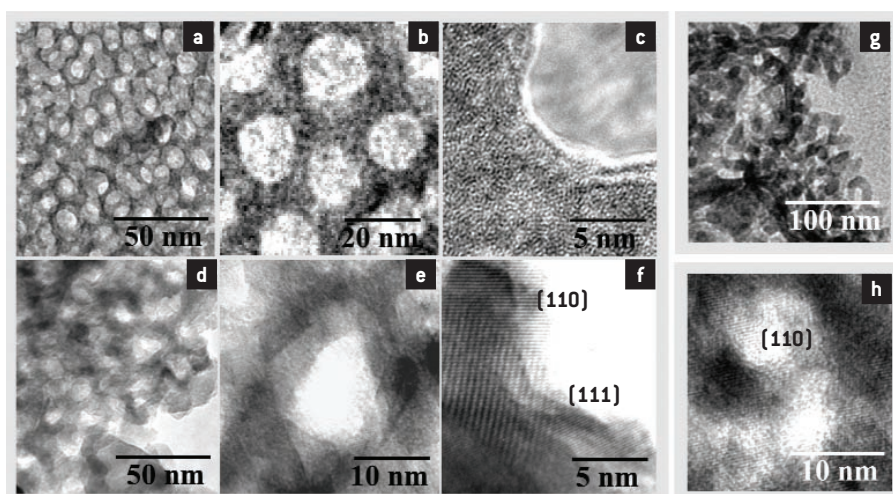
The structural evolution of the mesoporous networks during crystallisation is illustrated by HRTEM images in Figure 1 for SrTiO_3 , and by in-situ time-resolved simultaneous SAXS and WAXS investigations for SrTiO_3 , MgTa_2O_6 and $\text{Co}_{0.15}\text{Ti}_{0.85}\text{O}_{1.85}$ in Figure 2. The amorphous starting materials exhibit the typical 3D-structure of spherical pores, with diameters of around 12 nm, arranged into 3D arrays. Figures 1(b) also indicates a cubic-like arrangement, which is supported by SAXS patterns in Figures 2(a) (b) (c) and inset of (d) and (e). Prior to crystallisation, diffraction patterns are characteristic of a distorted body-centred-cubic organisation contracted in the direction normal to the substrate. The cubic structure is deduced by analogy to those always encountered with this special KLE surfactant. Moreover, the $\text{Co}_x\text{Ti}_{1-x}\text{O}_{2-x}$ system shows the typical $\text{Im}\bar{3}\text{m}$ derived patterns in Figures 2(a), (b), and (c) obtained after the distortion associated to the treatment. This distortion is more accentuated for systems that require fast evaporation processing, such as SrTiO_3 , or encounter fast condensation such as MgTa_2O_6 . After crystallisation, materials present an organised arrangement of nano-

crystalline particles that preserves the pristine initial network. The formerly curved pore interfaces have been flattened out and are now composed of reticular atomic planes (see Figure 1(e) and (f)). SAXS patterns ((c) and inset (e) and (f)) confirm that crystallisation induces the loss of in-plane order accompanying the off-plane order enhancement, characteristic of the transformation by diffusive sintering. They confirm that M_3NF retain their mesopore structure.

HRTEM images showed that the walls are composed of practically 100% of nanoparticles (10–20 nm in size) showing crystalline perovskite structure without preferential orientation. These images are representative of the whole sample and are faithful to all of the compositions under study, before and after nanocrystallisation. The results give evidence that amorphous mesoporous networks can be crystallised without extensive degradation of the meso-organisation by stopping the annealing just after reaching the temperature of crystallisation. Porosities of these M_3NF systems were evaluated to be 35%vol for $Co_{0.15}Ti_{0.85}O_{1.85}$, 31%vol for $SrTiO_3$, and 26%vol for $MgTa_2O_6$ using the Bruggeman Effective Medium Approximation (BEMA) model applied to ellipsometric data. EDX elementary analyses showed that the atomic ratio Sr:Ti within these crystalline regions is 1:0.98 – 1:1.02, as to be expected for clean $SrTiO_3$. Rutherford Back Scattering (RBS) investigations further confirmed this stoi-

chiometry and additionally revealed that both atomic concentration depth profiles remained homogeneous throughout the film thickness. This latter confirmation is extremely important since strict homogeneous dispersion of cationic centres within the walls is necessary to allow homogeneous nucleation and crystalline nanoparticle growth, which leads to the high quality M_3NF . Moreover, it is an important prerequisite of the process that this nucleation rate, defined by the material and the tempering procedure, fits to the structural design, i.e. the mesopore structure is only preserved when the wall thickness is of the order or larger than the nanocrystals' size. Therefore, the appropriate choice of a sufficiently large block copolymer template is crucial, and the present template (KLE3739) was selected also with respect to a sufficient size of the units of mesoscale assembly. It is also important to limit the time at high temperatures to prevent extensive sintering leading to the destruction of the ordered mesoscopic architecture as illustrated in Figure 1(g). The temperature range for optimal “ M_3NF ” materials formation (given in Table 1) is deduced from simultaneous in-situ SAXS and WAXS data. It has to be emphasised that the simultaneous study of SAXS and WAXS on these films is a particularly pertinent tool for this optimisation, despite of the low amount of matter involved. Nanocrystalline structured films of the perovskite $SrTiO_3$ and tetragonal $MgTa_2O_6$

Figure 1. HRTEM images showing the typical morphology of a $SrTiO_3$ mesoporous ordered network before [(a), (b) and (c)] obtained at 590°C and after [(d), (e) and (f)] obtained at 630°C crystallization into M_3NF . Image (g) represents the same $SrTiO_3$ system but calcined at 660°C where prolonged sintering leads to elongated particles responsible for the mesoscale order degradation. Characteristic reticular planes of $SrTiO_3$ perovskite [630°C] and of tetragonal $MgTa_2O_6$ [780°C] are clearly visible in images (e) and (f), and (h) respectively, where crystalline nanoparticles surround mesopores.

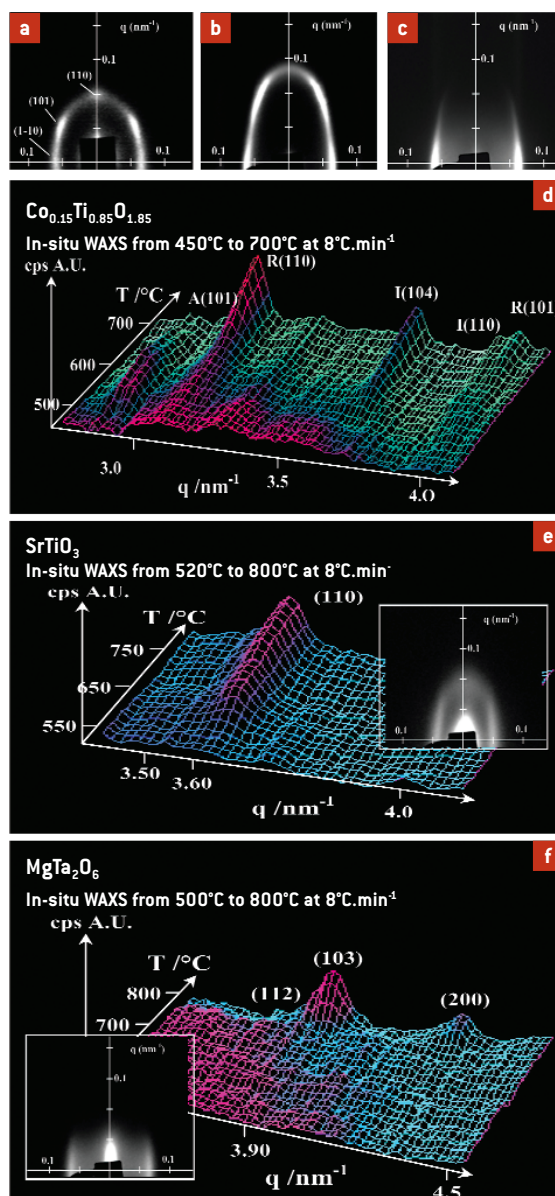


were optimally obtained at 610°C and 760°C, respectively, when using an 8°C·min⁻¹ heating ramp. For Co_xTi_{1-x}O_{2-x} compositions, either pure crystalline cobalt-doped Anatase (or Rutile), or binanocrystalline mesoporous materials with appearance of Ilmenite CoTiO₃ phases can be obtained. The mono- or bicrystallinity depends on the thermal treatment attending that each phase is formed at a different temperature (for thermodynamic stability reasons). According to the WAXS data, ferromagnetic semi-conducting Co-doped Anatase is present within

the mesostructure between 500 and 570°C. Ilmenite is formed after 570°C and Co-doped Anatase transforms into Co-doped Rutile above 650°C. Since the mesostructure is lost at 660°C, one can select the optimal temperature to prepare mesostructured porous Co-doped Anatase or Ilmenite coexisting with Titania nanoparticles thin layers. This was verified for cobalt compositions ranging from 0 to 0.30, except that the temperature of Rutile formation decreases with x since divalent cations are known to catalyse this transformation [2].

Figure 2. In-situ time-resolved simultaneous SAXS and WAXS investigations: WAXS evolution is represented for SrTiO₃ **(e)**, MgTa₂O₆ **(f)**, and Co_xTi_{1-x}O_{2-x} **(d)** (A, R, and I stand for Anatase, Rutile and Ilmenite respectively) during annealing at 8°C·min⁻¹ under air (in-set of **(e)** and **(f)** are the corresponding SAXS patterns obtained at 630°C for SrTiO₃ and 780°C for MgTa₂O₆). Typical mesoorder evolution is represented by the 2D-SAXS patterns for Co_xTi_{1-x}O_{2-x} systems

(a) dried at 100°C, **(b)** just before Anatase crystallisation, and **(c)** after Anatase crystallisation. They revealed that the mesoorder with nanocrystalline structure is retained if extended sintering is disabled at the pore interface just after nucleation. All mesostructures are bcc Im3m-derived and the degree of ordering is lower for MgTa₂O₆ and SrTiO₃ than for Co-containing Titania phases as a result of required processing conditions.



	SrTiO ₃	MgTa ₂ O ₆	Co _{0.15} Ti _{0.85} O _{1.85}
KLE 3739	0.125g	0.075g	0.05g
M1	0.347g [SrCl ₂ ·6H ₂ O]	0.029g [Mg(OH) ₂]	0.025g [CoCl ₂]
M2	0.265g [TiCl ₄]	0.42g [Ta(OEt) ₅]	0.185g [TiCl ₄]
EtOH	7.25g	6g	3g
THF	2g	1g	1g
H₂O	1.5g	-	0.2g
HCl 37% conc	-	1.5g	-
Crystallisation	610°C	760°C	500°C*-570°C*-650°C*
Deconstruction	660°C	800°C	660°C

METHODS

In the first step, isotropic solutions containing the stoichiometric ratio (x and y) of different metallic M1 and M2 precursors, and a certain volume fraction (ϕ) of the block copolymer KLE3739 (PBH₇₉-b-PEO₈₉, (PBH = hydrogenated poly(butadiene)) template, are dissolved in a highly volatile medium and are stabilised within an appropriate pH range (see Figure 1(a) and Table 1). Because of the very different solubilities and sol-gel chemistries of the different cations involved, the choice of the metallic precursors and sol composition is crucial. Here, SrCl₂·6H₂O, TiCl₄, CoCl₂, Mg(OH)₂ and Ta(OC₂H₅)₅ precursors were dissolved in a mixture of THF, EtOH and H₂O (see Table 1 for the details). Extended condensation of metallic species was inhibited by promoting high hydrochloric acid content in the solution, either added when using alkoxide precursors or created by transalcoholysis and hydrolysis of chlorides precursors [3]. Ultrasonic vibrations and moderate heating are used to homogenise the solution before deposition. In the second step, films were prepared by dip-coating silicon wafers substrate in a controlled atmosphere at a constant withdrawal rate. Typically, optimal dip-coating conditions were obtained for 30% relative humidity (RH) and 25°C up to evaporation completion for all compositions. For Co_{0.15}Ti_{0.85}O_{1.85} and MgTa₂O₆ a higher degree of meso-ordering is achieved by applying 60% RH at 25°C for several hours after deposition. For SrTiO₃, it is necessary to apply saturated humidity atmosphere (RH = 100% at 25°C)

for 1 min right after completion of the evaporation, followed by a fast transfer to 100°C. These latter conditions are necessary to prevent local crystallisation of SrCl₂ before rigidification of the network. Further stabilisation of the network before crystallisation was achieved by thermal consolidation (dehydration) at 300°C under air for 30 min. “M₃NF” materials were obtained through controlled nanocrystallisation provided by heating with a ramp of 8°C·min⁻¹ under air up to 500°C for Anatase Co_{0.15}Ti_{0.85}O_{1.85}, 610°C for SrTiO₃, and 760°C for MgTa₂O₆.

References

- [1] Grosso D., Cagnol F., Soller-Illia G.J. de A.A., Brunet-Bruneau A., Bourgeois A., Amenitsch H., & Sanchez C., *Adv. Funct. Mater.*, **14**, 309 (2004)
- [2] Grosso D., Boissiere C., Smarsly B., Brezesinski T., Pinna N., Albouy P.A., Amenitsch H., Antonietti M., & Sanchez C., *Nature Materials*, **3**, 787 (2004).
- [3] Grosso D., Soler Illia G.J.A.A., Babonneau F., & Sanchez C., *Adv. Mater.* **13**, 1085 (2001). Crepaldi E.L., Soler-Illia G.J.A.A., Grosso D., Cagnol F., Ribot F., & Sanchez C., *J. Am. Chem. Soc.* **125**, 9770 (2003)

Table 1.

Chemical compositions of the initial solutions used for the preparation of M₃NF (for procedure, see Method's section). The critical temperatures of crystallisation and mesostructure degradation are also reported [*Co-doped Anatase, Ilmenite and Co-doped Rutile crystallise into the given order].

STRUCTURAL BIOLOGY

The field of structural biology continues to flourish and the 3D structural information obtained supports much of modern molecular biology, medicine, biotechnology and pharmaceutical drug design.

The external scientific Programme supported nearly 100 separate experimental sessions, at the XRD1 beamline, with more than 300 visiting scientists (1st July 2004 – 30th June 2005), providing research highlights resulting in publications in Journals of the highest quality and impact. Some selected examples follow.

Capaldi *et al.* (page 70), report the crystal structure of the C-terminal domain of the insulin-like growth factor-binding protein-1 (IGFBP-1) from human amniotic fluid. IGFBP-1 regulates the activity of the insulin growth factors in early pregnancy and is, thus, thought, to play a key role at the fetal-maternal interface. The studied fragment folds as a thyroglobulin type I domain and was found to bind Fe²⁺.

Vallone *et al.* (page 73), summarise the investigations of ligand-linked conformational changes, discovered by crystallography, in the structure of neuroglobin, a globin expressed in the nervous system of humans and other organisms that is involved in the protection of the brain from ischemic damage. A heme-sliding mechanism of affinity control has been disclosed. It may account for the involvement of neuroglobin in controlling the activation of a protective signal.

The structural basis for the interaction between a tomato fruit pectin methylesterase and a specific inhibitor protein from kiwi is reported by Di Matteo *et al.*, (page 76). The structure of the complex provides an insight into the specificity of the inhibitor toward plant pectin methylesterases and the mechanism of regulation of these enzymes.

Cyclin-dependent kinases (CDKs) regulate the cell cycle, apoptosis, neural functions, transcription, and exocytosis. The observation of CDK deregulations in various pathological situations suggests that CDK inhibitors may have a therapeutic value. Hardcastle *et al.* (page 79), outline the results obtained for key compounds in a structure-based drug discovery program in the search of potent CDK1 and -2 inhibitors.

In order to keep pace with this rapidly evolving field, the close collaboration with the International School for Advanced Studies and the International Centre for Genetic Engineering and Biotechnology, in Trieste, plays an important role for providing to the *in house* structural biology programme at ELETTRA an excellent infrastructure and partnership.

Furthermore, in order to satisfy the structural biology community requests for beam time, beamline brilliance, user friendly high-throughput data acquisition and processing, a full upgrade and refurbishing of the XRD1 beamline has been scheduled (August 2006 - January 2007). The design and construction of a second protein crystallography beamline has been planned to start for late next year. This project has been funded by grants (FIRB) of the Italian Ministry for Research and Education MIUR.

*Doriano Lamba and Maurizio Polentarutti
on behalf of the Structural Biology and XRD1 Beamline Research Team*

X-RAY STRUCTURE OF THE C-TERMINAL DOMAIN OF HUMAN INSULIN-LIKE GROWTH FACTOR BINDING PROTEIN-1

> **Stefano Capaldi, Beniamino Faggion, Massimiliano Perduca, Maria E. Carrizo, Hugo L. Monaco**
Biocrystallography Laboratory, Department of Science and Technology, University of Verona, Ca Vignal 1, strada Le Grazie 15, 37134 Verona, ITALY

> **Alberto Sala, Monica Campagnoli, Sara Labò, Assunta Romano, Maurizia Valli, Livia Visai, Lorenzo Minchiotti, Monica Galliano**
Department of Biochemistry "A. Castellani", University of Pavia, via Taramelli 3b, 27100 Pavia, ITALY

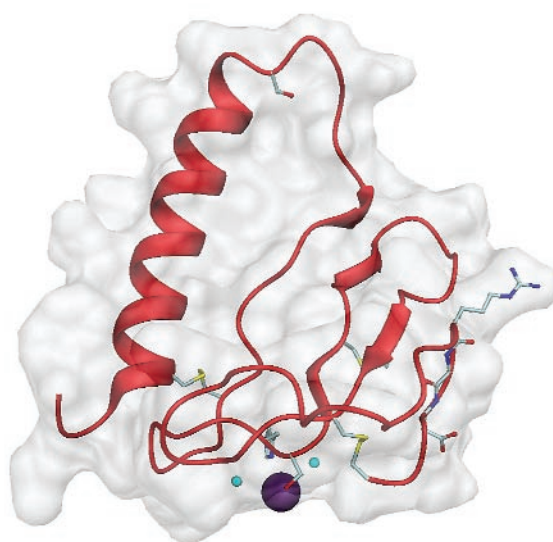
Insulin-like growth factor binding protein-1 is a member of a family comprising six secreted proteins (designated IGFBP-1 to IGFBP-6) that can modulate upon binding the availability and thus the biological effects of insulin-like growth factors I and II (IGF-I and IGF-II). Both inhibition and enhancement of the hormone action have been described and several mechanisms, including binding of IGFBPs to the extracellular matrix, phosphorylation and proteolysis, have been shown to modulate their affinity for IGFs. Moreover, an increasing number of reports indicate that IGFBPs can regulate cellular functions independently of

their ability to interact with IGFs [1,2]. Each IGFBP polypeptide chain, ranging in length from 216 to 289 amino acids, may be divided into three distinct domains of approximately equal size. The N- and C-terminal portions exhibit a high primary sequence identity across the six IGFBPs and contain spatially conserved cysteine residues that form intra-domain disulfide bonds.

The three dimensional structure of the C-terminal domain of IGFBP-1 was determined by X-ray crystallography to 1.8 Å resolution using data collected at ELETTRA and phasing the structure factors with the multiple isomorphous replacement method with

Figure 1. Ribbon diagram and molecular surface of the C-terminal domain of human IGFBP-1. The three disulfide bridges are shown in yellow. The diagram shows the phosphorylated serine

[Ser 194] and the RGD motif [Arg 246-Gly 247-Asp 248] as ball and stick models. The Fe^{2+} ion is represented as a dark blue sphere and the water molecules are light blue.



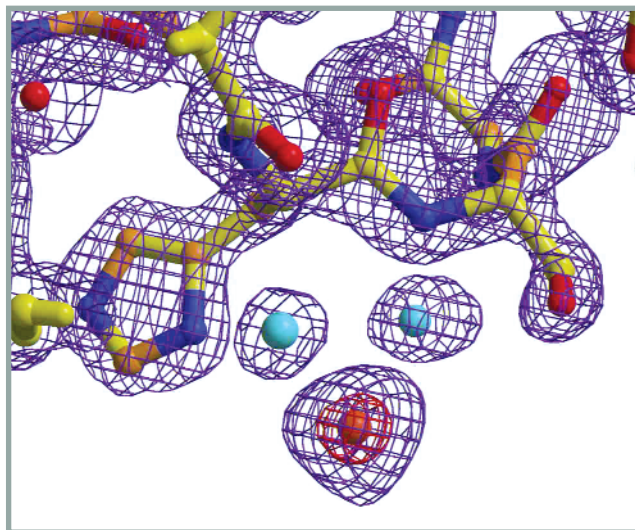


Figure 2. Electron density of the Fe^{2+} ion in the co-crystals of the C-terminal domain of IGFBP-1. The red density of the Fobs-Fc map is contoured at a 7σ level; the blue electron density of the 2Fobs-Fc map is contoured at a 1.5σ level.

two derivatives: K_2PtCl_4 and $\text{C}_2\text{H}_5\text{HgOH PO}_2$. Two platinum sites were located in a difference Patterson map and refined using the program MLPHARE. The S.I.R. phases were used to locate the most significant mercury site in the difference Fourier map. The two major sites (one site from each of the two derivatives) were used as input for the program autoSHARP that was used to locate the minor sites of the two derivatives, and for density modification and final phasing. The electron density map thus produced was of excellent quality and could be readily interpreted. The initial model was built in the high quality map using the program O and was subsequently refined with the program REFMAC. During the process of refinement and model building, the quality of the model was controlled with the program PROCHECK. Solvent molecules were added to the model in the final stages of refinement according to hydrogen-bond criteria and only if their B factors refined to reasonable values and if they improved the R_{free} . The final model contains 642 non hydrogen protein atoms and has very reasonable geometry, with 87.5% of the residues in the most favored regions of the Ramachandran plot and the remaining 12.5% in the additionally allowed region. The overall R factor is 21.6% and the R_{free} is 27.1%.

The fragment folds as a thyroglobulin type I domain. The first element of secondary structure of the domain is a beta turn spanning residues 172-175 (we follow the numbering of the full-length precursor, SWISSPROT accession number P08833), the second is an alpha helix which spans 19 residues, from Pro 175 to Thr 193. The next four residues in the sequence: Ser 194, Gly 195, Asp 196 and Asp 197 are disordered in the maps. Ser 194 was phosphorylated in the protein used to prepare the crystals that were used in all the X-ray diffraction experiments but no clear electron density for the phosphate group was present in the maps. The rest of the domain contains four very short strands of anti-parallel beta sheet and five additional beta turns. The four strands span the following residues: 200-201 and 219-220 and 215-217 and 228-230. A total of 10 residues are thus found in beta strands and 24 in the six beta turns. A gamma turn of the inverse type is formed by residues Ile 245-Arg 246-Gly 247, where two of the three residues are part of the RGD motif that binds to integrins. The three disulfide bridges are formed by Cys 176 and Cys 206, by Cys 217 and Cys 228 and by Cys 230 and Cys 251, the last residue that is clearly defined in the maps. The electron density of the three bridges is very clear in all the maps.

Figure 3. Diagram representing the groups coordinated to the Fe^{2+} ion.

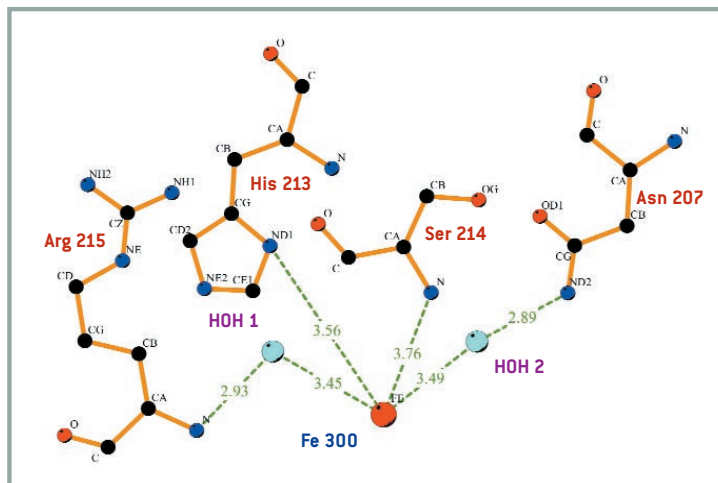


Figure 1 is a cartoon representation of the C-terminal domain of IGFBP-1. Notice the position of the RGD motif (Arg 246-Gly 247-Asp 248), represented in the figure as ball and stick models, on the opposite side of the alpha helix. The figure shows also the position of the Fe^{2+} binding site (see below).

Crystals of the C-terminal domain of IGFBP-1 were soaked in 10 mM solutions of the following metal compounds: CaCl_2 , FeSO_4 , FeCl_3 , CoCl_2 , NiSO_4 and MnCl_2 . X-ray data were collected and difference Fourier maps were calculated and examined. The crystals soaked in FeCl_3 were found not to diffract at all while, the crystals soaked in the other metals did not show any significant extra electron density with only one exception: FeSO_4 that presented a very high peak, clearly visible with a cutoff of 7 sigma in the Fobs-Fc map, and present in a position of the molecule where it could be easily interpreted in chemical terms. Figure 2 shows the electron density of the Fe^{2+} ion in the co-crystals of the C-terminal domain of IGFBP-1 in both an Fobs-Fc and a 2Fobs-Fc maps. The red density of the Fobs-Fc map is contoured at a 7 σ level and the blue electron density of the 2Fobs-Fc map is contoured at a 1.5 σ level. The diagram in Figure 3 represents the side chains coordinated to the bivalent ion. The Fe^{2+} ion is coordinated tetrahedrally to a nitrogen

atom of the ring of the only histidine present in the polypeptide chain, His 213, and to the OG of Ser 214. The other two positions are occupied by two water molecules that are also bound to the polypeptide chain nitrogens of residues 207 and 215. Of the four coordination positions two involve side chains, those of His 213 and Ser 214, while the other two are dependent on two polypeptide chain nitrogens.

ELISA experiments have shown that Iron (II) decreases the binding of intact IGFBP-1 and the C-terminal domain to IGF-II suggesting that the metal binding site is close to or part of the surface of interaction of the two molecules. A more detailed description of this structure and the metal-binding site is given in reference [3].

References

- [1] Baxter R.C. *Am J Physiol Endocrinol Metab.* **278**:E967-E976 (2000)
- [2] Firth S.M. and Baxter R.C. *Endocr Rev.* **23**:824-254 (2002)
- [3] Sala A., Capaldi S., Campagnoli M., Faggion B., Labo S., Perduca M., Romano A., Carrizo M.E., Valli M., Visai L., Minchiotti L., Galliano M. and Monaco H.L. *J Biol Chem.* **280**:29812-29819 (2005)

THE STRUCTURE OF CARBONMONOXY NEUROGLOBIN: A NOVEL MECHANISM FOR CONTROL IN LIGAND AFFINITY

> B. Vallone, M. Brunori

Department of Biochemical Sciences and Istituto Pasteur-Fondazione Cenci Bolognetti University of Rome "La Sapienza", P.le A. Moro 5, 00185 Rome, ITALY

> K. Nienhaus, A. Matthes

Department of Biophysics, University of Ulm, Albert-Einstein-Allee 11, 89081 Ulm, GERMANY

> G. Ulrich Nienhaus

Department of Biophysics, University of Ulm, Albert-Einstein-Allee 11, 89081 Ulm, GERMANY

Department of Physics University of Illinois at Urbana-Champaign, 1110 W. Green St. Urbana, IL 61801, USA

INTRODUCTION

Neuroglobin (Ngb) is a vertebrate heme protein expressed in the brain. It displays the canonical globin fold (1,2). In contrast to hemoglobins (Hbs) and myoglobins (Mbs), the heme iron in human and murine ferric Ngb (metNgb) is hexacoordinated by the distal and proximal histidines, His64 and His96, in the absence of an exogenous ligand. MetNgb displays a huge internal tunnel (~287 Å³) that connects the distal and proximal sides of the heme. Hexacoordination has been proposed as a novel mechanism to regulate ligand affinity in heme proteins because the covalent bond between the heme iron and His64 has to be broken for an exogenous ligand to bind.

The physiological role of Ngb is intriguing but as yet unclear. Its low expression level in the micromolar range suggests a physiological function different from simple O₂ storage and transport. In recent studies, up-regulation of Ngb expression was observed under conditions of hypoxia or ischemia in vitro and in vivo (3), which may foster neuronal survival after a stroke. Other possible functions, such as NO scavenging or NADH oxidase activity, have also been discussed.

RESULTS

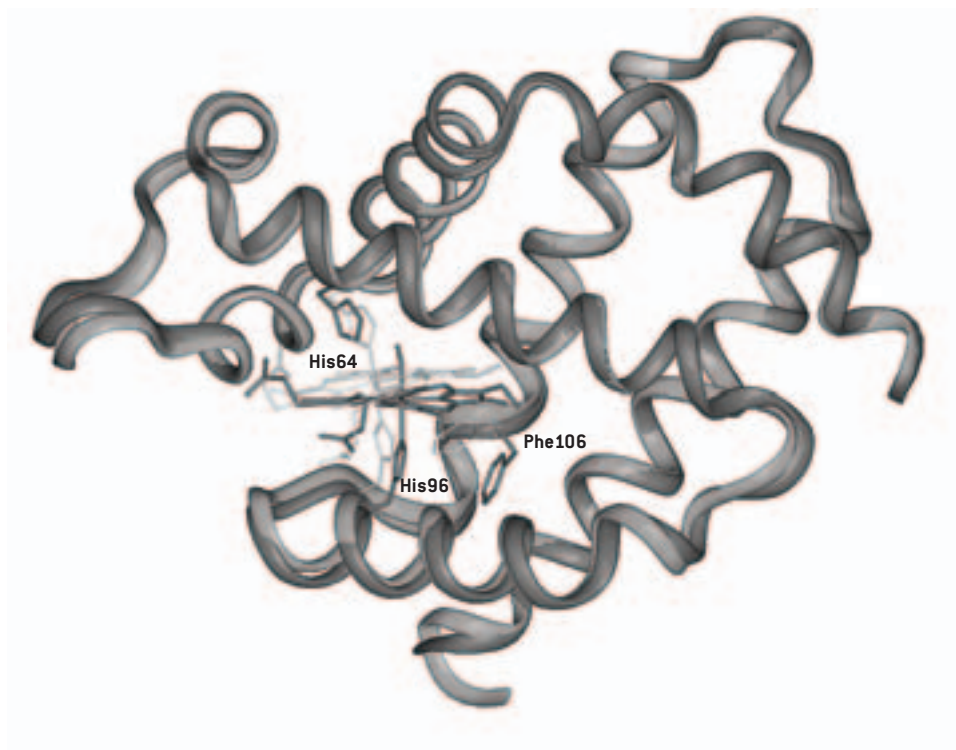
The overall tertiary fold of murine Ngb is only moderately affected by iron reduction and CO binding (Figure 1), which is in line with observations on swMb and other

monomeric globins. CO binding induces a major heme displacement within the frame of the globin fold (Figure 1), which may define a new mechanism for ligand affinity modulation in hexacoordinated globins. Apparently, when CO binding releases the positional constraint imposed by the Fe-His64 distal bond, the heme is free to tilt towards the distal side and slide deeper into its crevice.

In metNgb, the heme internal rim contacts are less extensive than in other globins, to the point of being permissive of heme orientational disorder within its binding pocket (1,2). The NgbCO structure unveils the functional significance of this peculiar feature: the absence of close contacts on the CHC side (opposite to the propionates) is essential to allow the heme sliding movement upon ligand binding. Very unexpectedly, the proximal branch of the large cavity observed in metNgb disappears, and the huge tunnel acquires a partially novel topology. Comparison of the overall B-factors of metNgb and NgbCO suggests that rupture of the Fe-His64 bond and the subsequent docking of the heme in its new position represent a relaxation of Ngb to a more stable structure.

Consequences of Heme Sliding. Repositioning of the heme group coupled to CO binding affects the conformation of some adjacent amino acids (Figure 1). Surprisingly, the distal His64 C_α moves by only 0.5 Å and its side chain N_{epsilon} atom by 0.7 Å.

Figure 1. Ribbon representation of NgbCO (dark gray) and unligated metNgb (light grey). The distal histidine, His64, the proximal histidine His96, Phe106 and the heme group are also given in stick representation.



Consistent with the scenario of heme sliding into a preformed docking site, only Phe106 is drastically repositioned (Figure 1), this shift is accompanied by a rearrangement of the preceding FG loop. The His96 displacement causes a shift of the F helix that is propagated to the EF loop. In addition to these protein rearrangements in the EF-FG region, the CD loop also moves to a more “open” conformation upon ligand binding.

Structural Changes in the Internal Cavities. The large ($\sim 287 \text{ \AA}^3$) internal cavity observed in metNgb (1,2) is reshaped upon CO binding. The branch at the proximal heme side is occupied by the heme and Phe106, leaving only a small niche (8.2 \AA^3) close to the proximal His96. The distal cavity branch is deepened and forms a small open space (13.3 \AA^3) lined by residue Ser55 (a Cys in wt Ngb). Reshaping of the large tunnel causes a miniscule increase of its total volume to 306 \AA^3 . It still connects to the surface of the protein via a channel lined by Leu70, Val71, Ala74, Leu85 and Tyr88, as in metNgb.

Structural Mechanism of Ligand Control. The structure of NgbCO reveals how the unusual cytochrome-like iron-distal His coordination is made sufficiently labile to allow binding of exogenous ligands. A primary factor that counterbalances the presence of internal coordination (which a priori should be fairly stable) seems to be the docking of the heme in a new position, leading to an overall more stable protein conformation with drastically reduced Bfactors in the EF loop. The coupling of heme relocation to reshaping of the large internal tunnel, accompanied by a substantial restriction of the connecting path to the bulk, might be relevant to more complex functions of Ngb. The conformational changes coupled to ligand binding may allow internal trapping of further, possibly different, exogenous ligands to enhance multiple collisions and possibly more complex chemistry.

Physiological Implications. Ngb, with its P_{50} 2 torr, is most likely reduced and ligated by O_2 under physiological conditions (normoxia). Under O_2 deficiency, Ngb will release its heme-bound ligand and adopt the hexa-

coordinate deoxy structure; the same coordination change is expected upon autoxidation and release of O₂. The B factor increase indicates that exogenous ligand release will be accompanied by a pronounced increase in the mobility of the EF loop. The loosening of the structural constraints in the EF loop may be the signal encoding the information 'low oxygen'. This signal may be transmitted further by interaction with GDP-bound G_{αi}, thereby liberating G_{βγ}, which protects the cell against neuronal death.

CONCLUSIONS

The three-dimensional structure of murine NgbCO, together with the metNgb structure from the same species reported previously, allows us to assess the conformational changes that accompany exogenous ligand binding in Ngb. Based on this comparison, some conclusions can be drawn regarding the mechanism of ligand affinity regulation in hexacoordinate heme proteins. Given that the distal histidine efficiently blocks the binding site in the unligated state, we believe that the major heme displacement occurring upon exogenous ligand binding, will assist rupture of the distal His-iron coordination bond, facilitating O₂ binding. Moreover heme sliding is accompanied by a dramatic topological reorganization of the large internal cavity and a marked decrease of the overall B factors. This pronounced change in flexibility and conformation could represent the molecular basis of the signaling function of Ngb in the case of hypoxia.

METHODS

Crystallization. Crystals of metNgb double mutant C55S-C120S were grown using the hanging-drop vapor-diffusion method. To prepare the CO derivative, crystals were transferred into vials containing mother liquor with 25% glycerol added as cryoprotectant. The heme iron was reduced by adding sodium dithionite to a final concentration of 5 mM. Afterwards, the N₂ gas in the vials was replaced by CO. Finally, the CO-ligated crystals were frozen and stored in liquid N₂ until data collection.

Structure determination. X-ray diffraction data were collected at the ELETTRA Syn-

chrotron source (Trieste, Italy) using an X-ray wavelength $\lambda = 1.2 \text{ \AA}$. At 100 K, the NgbCO crystals diffracted up to 1.7 \AA resolution on a MAR CCD detector. The crystals were isomorphous with the metNgb crystals measured previously (1). The structure of NgbCO was determined by Fourier difference methods using the metNgb structure at 1.5 \AA . The final model contains most of the protein sequence (amino acids 3-148) and 116 water molecules (Table 1). Careful visual inspection of the electron density maps of NgbCO indicates that a minor fraction (<10%) is still in the unligated state. This is only evident from a clear positive density observed at 3 σ , centered at the position occupied by the iron in the unligated structure. Corresponding features from the lighter atoms remain undetected in the electron density map because of their lower electron densities.

References

- [1] Pesce A., Dewilde S., Nardini M., Moens L., Ascenzi P., Hankeln T., Burmester T. & Bolognesi M., *Structure (Camb)* **11**, 1087-1095. (2003)
- [2] Vallone B., Nienhaus K., Matthes A., Brunori M., Nienhaus G.U., *Proc Natl Acad Sci USA* **101**, 17351-6 (2004)
- [3] Sun Y., Jin K., Peel A., Mao X.O., Xie L. & Greenberg D.A., *Proc. Natl. Acad. Sci. USA* **100**, 3497-3500 (2003)

CRYSTAL STRUCTURE OF THE COMPLEX BETWEEN PECTIN METHYLESTERASE AND ITS INHIBITOR PROTEIN

> A. Di Matteo, D. Bonivento, D. Tsernoglou

Dept. of Biochemical Science, University of Rome, P.le Aldo Moro 5, 00185 Rome, ITALY

> D. Bellincampi, F. Cervone, G. De Lorenzo, A. Raiola

Dept. of Plant Biology, University of Rome, P.le Aldo Moro 5, 00185 Rome, ITALY

> A. Giovane

Department of Biochemistry and Biophysics, Second University of Naples, 80138, Naples, ITALY

> L. Camardella

Institute of Protein Biochemistry, Consiglio Nazionale delle Ricerche, 80125, Naples, ITALY

Pectin, one of the main components of the plant cell wall, is secreted as a highly methyl-esterified form and subsequently demethylated in muro by pectin methylesterases (PMEs). The level and pattern of pectin esterification changes during cell expansion, growth and fruit ripening as well as during infection by phytopathogenic microorganisms [1].

PMEs produced by plants take part in important physiological processes, such as pollen growth, seed germination and root development. They are also proposed to play a role in response to fungal pathogen infection and are required for the systemic spread of the *Tobacco mosaic virus*. In plants various PMEs isoforms differing by pI, molecular weight and biochemical activity are encoded by gene families and are either constitutively expressed or differentially regulated in specific tissues and developmental stages. PMEs are produced not only by plants but also by pathogenic fungi and bacteria during their interaction with plants; deesterification of pectin, in fact, may help the action of hydrolytic enzymes produced by pathogens to degrade the plant cell wall [1].

Specific protein inhibitors of the PME activity have been recently characterised in kiwi (*Actinidia deliçosa*) fruit and *Arabidopsis thaliana* plants [2]. In order to clarify the structural features of the PME-PMEI interaction, we solved the crystal structure of the complex between a PME from tomato fruit

(PME-1) and a PMEI from kiwi fruit (AcPMEI) [3]. AcPMEI is a strong inhibitor of PME ($K_D = 5$ nM at pH 5.5) and forms a 1:1 non-covalent complex.

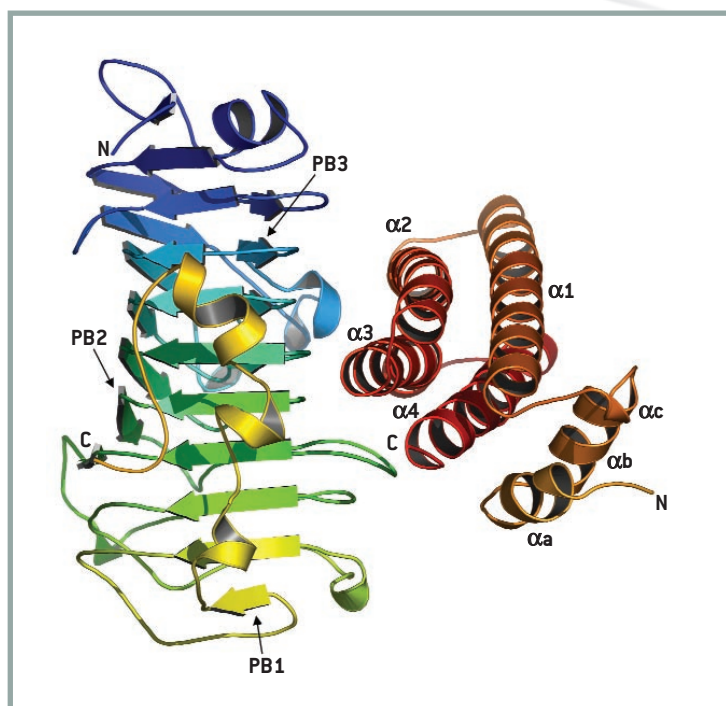
The enzyme was mixed with a molar excess of the inhibitor and the complex was purified by ionic exchange chromatography. The PME-PMEI complex was crystallised into two forms (named form A and form B herein). The X-ray diffraction data for the native crystals of both form A and form B were collected at the ELETTRA synchrotron (Trieste, Italy) at 2.8 Å and 1.9 Å resolution, respectively. Form A crystal belongs to the space group P41212 with unit cell dimensions of $a=b=120.26$ Å, $c=97.29$ Å, and $\alpha=\beta=\gamma=90^\circ$. Form B crystal belongs to the space group P3221 with the following unit cell dimensions: $a=b=90.38$ Å, $c=149.1$ Å, $\alpha=\beta=90^\circ$ and $\gamma=120^\circ$. The 3D-structure of the complex was determined using a combination of single isomorphous replacement and molecular replacement methods. Initial phases were determined by SIRAS method, using a data set from a form A crystal soaked with 1mM K_2OsO_4 . Diffraction data for the osmium derivative were collected at the DESY Synchrotron (Hamburg, Germany). The program SOLVE/RESOLVE was used to obtain an initial electron density map at 2.8 Å resolution in which we were able to build only a partial model of the complex. The incomplete model was utilised as a template to perform a molecular replacement

using native data from form B with the program AMORE. We obtained a clear electron density map at 1.9 Å resolution that was used to complete the tracing. The model was refined using iteratively REFMAC5 and simulating annealing procedure as implemented in CNS. The final structure consists of PME-1 (residues 1 to 317) Ac-PMEI (residues 0 to 150) and 462 water residues (PDB ID 1XG2).

PME-1 folds in a right-handed parallel β helix typical of pectic enzymes, composed of three extended β -sheets (PB1, PB2 and PB3). Residues hypothesised to be responsible for catalysis (Asp132, Asp153 and Arg221) as well as residues thought to be involved in substrate binding (Phe80, Tyr135, Phe156, Tyr218, Trp223, and Trp248) are located in a shallow cleft within the PB3 sheet.

AcPMEI fold in an up-and-down four helical bundle in which the helices (α 1, α 2, α 3 and α 4) align in an antiparallel manner. An N-terminal helical region extends outside the central domain.

PME and PMEI form a complex in which the inhibitor covers the shallow cleft of the enzyme where the putative active site is located. PMEI packs perpendicular to the PME β -helix by interacting with three (α 2, α 3 and α 4) out of the four helices of the bundle (Figure 1 and 2). The protein-protein interface is fairly large (Δ ASA=2208 Å²) and displays a highly polar character. The formation of the complex is mediated by a



high number of direct and water-mediated H-bonds. Fifty residues (23 on PME and 27 on PMEI) establish intermolecular contacts: twenty-two of these residues are engaged in H-bonds, and four form salt bridges.

Putative catalytic residues (Asp132, Asp153, and Arg221) do not establish contacts with the inhibitor, while three (Phe80, Tyr135 and Trp223) of the residues responsible for substrate binding, interact with the inhibitor. Therefore, consistently with the competitive mode of inhibition observed,

Figure 1. Ribbon representation of the PME-PMEI complex. The enzyme is shown in green-blue on the left side. The inhibitor is represented in yellow-red on the right side.

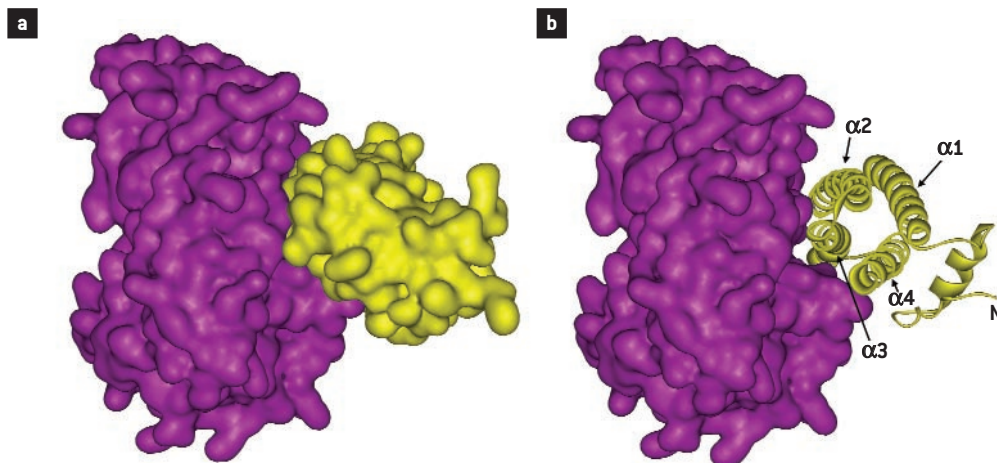
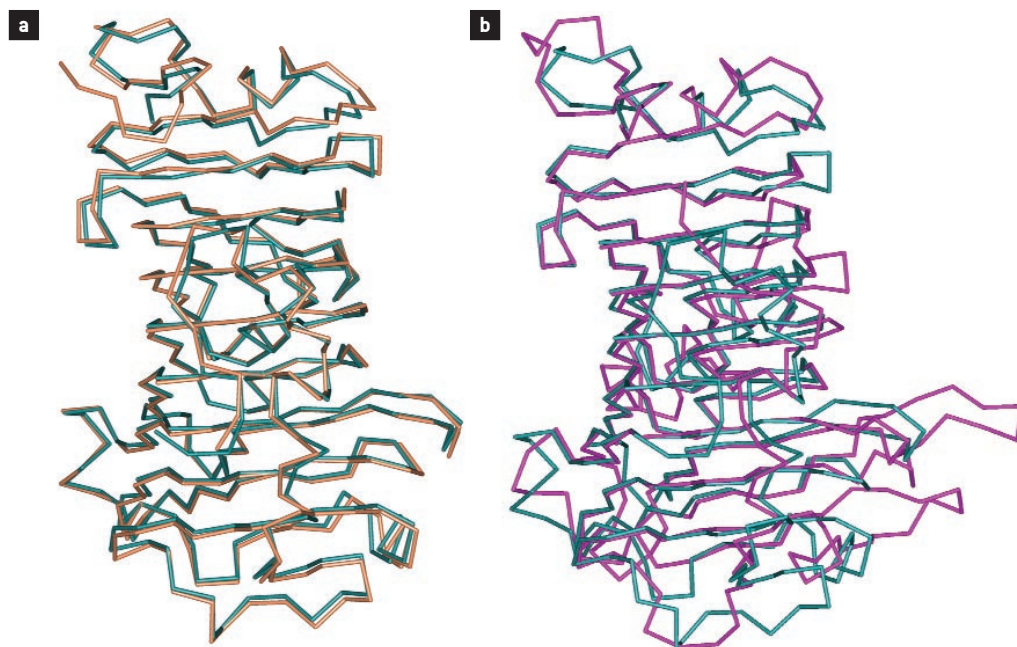


Figure 2. (a) Representation of the molecular surface of the enzyme (violet) and the inhibitor (yellow) in the complex. (b) Same view of the complex as in (a), showing the molecular surface of the PME and a ribbon diagram of PMEI.

Figure 3. Comparison of the known structures of PME.

(a) Overlay of the C α trace of PME from tomato (green) and PME from carrot (orange).

(b) Superimposition of PME from tomato (green) and PME from *E. chrysanthemi* (violet). Although the β -helices are completely superimposable, main differences are located in the length of the turns protruding out from the β -helix in proximity of the putative active site cleft.



the inhibitor covers the active site cleft of the enzyme preventing the substrate access; the formation of the complex impedes the interactions that are necessary for binding the substrate to the enzyme.

Interestingly, PMEIs inhibit PMEs of plant origin and do not affect the activity of microbial enzymes. The structure of the PME-PMEI complex provides a possible explanation for the lack of inhibition of PMEIs on non plant-derived PMEs analysed so far. Superimposition of the known structures of PME from carrot and from the bacterium *Erwinia chrysanthemi* with the PME-1 from tomato reveals that the plant-derived PMEs are almost identical, whereas in the bacterial enzyme the active site cleft in which the putative active site is located, is much deeper than in the enzymes of plant origin (Figure 3). It is likely that the external loops of the bacterial enzyme create a steric hindrance that prevents the interaction with the inhibitor. Furthermore PMEI is inactive towards PME form the phytopathogenic fungus *Aspergillus aculeatus*. Interestingly, almost all of the residues important for the interaction of tomato PME with the inhibitor are conserved in

plant PMEs but not in the fungal enzyme thus providing a reason for the observed lack of interaction.

In conclusion the results presented here allow a detailed analysis of the mode of interaction between PME and its inhibitor protein in terms of specificity and shed light into the regulation of pectin deesterification in plants.

References

- [1] Micheli F, *Trends Plant Sci* **6**, 414-419 (2001)
- [2] Raiola A., Camardella L., Giovane A., Mattei B., De Lorenzo G., Cervone F., and Bellincami D., *FEBS Lett.* **557**, 199-203 (2004)
- [3] Di Matteo A., Giovane A., Raiola, A., Camardella L., Bonivento D., De Lorenzo G., Cervone F., Bellincampi D., Tsernoglou D., *Plant Cell* **17**, 849 (2005)

N²-SUBSTITUTED-O⁶-CYCLOHEXYLMETHYLGUANINE DERIVATIVES: POTENT INHIBITORS OF CDKs 1 AND 2

> I.R. Hardcastle, C.E. Arris, J. Bentley, Y. Chen, N.J. Curtin, A.E. Gibson, B.T. Golding, R.J. Griffin, J. Menyerol, V. Mesguiche, D.R. Newell, L.-Z. Wang, H.J. Whitfield

Northern Institute for Cancer Research, University of Newcastle, Newcastle upon Tyne, UK

> F.T. Boyle, P. Jewsbury

AstraZeneca Pharmaceuticals, Alderley Park, Cheshire, UK

> J.A. Endicott, M.E.M. Noble, D.J. Pratt

Laboratory of Molecular Biophysics and Department of Biochemistry, University of Oxford, Oxford, UK

The cyclin-dependent kinases (CDKs) play an essential role in regulating eukaryotic cell-cycle progression. Sequential activation of CDK4/6 and CDK2 controls progression from G1 into S phase, and activation of CDK1 is essential for progression from G2 into M phase. Many cell-cycle regulatory mechanisms that control CDK activity are altered in tumors. For example, mutation, deletion or epigenetic silencing of the p16^{INK4a} CDK inhibitor protein, loss of p53 and hence reduced p21^{Cip1} expression, lowered expression of p27^{Kip1}, over-expression of cyclin D, and mutation of CDK4 have all been reported.

A large number of ATP-competitive protein kinase inhibitors from a variety of chemical classes have been identified and are beginning to make a clinical impact [1]. First generation CDK inhibitors have entered clinical trials, but it is already apparent that significant complexities will be encountered in the development of this drug class. In particular, inhibitor specificity for CDKs over other kinases, and selectivity for a specific target CDK within the CDK family of enzymes, remain major challenges.

We initially identified compounds based on O⁶-cyclohexylmethylpurine (NU2058), as competitive inhibitors of both CDK1 and CDK2 with respect to ATP, and which also displayed good selectivity over CDK4 [2]. Crystallographic analysis of NU2058 bound to monomeric CDK2 and to the fully activated phosphorylated CDK2/cyclin A complex revealed that it forms a triplet of hydrogen bonds within the ATP binding site:

NH-9 acts as a hydrogen bond donor to the backbone carbonyl group of Glu81, and N-3 and 2-NH₂ accept and donate a hydrogen bond to the backbone carbonyl and amide groups, respectively, of Leu83. The O⁶-cyclohexylmethyl group occupies the CDK2 ribose-binding pocket.

A comparison of the structures of NU2058 and the CDK inhibitor purvalanol B bound to CDK2 revealed that the two purine derivatives adopt different binding modes within the CDK2 active site (Figure 1). Starting with the structure of NU2058 bound to CDK2 and guided by the CDK2/purvalanol B structure we have previously utilised structure-based development and iterative biological evaluation to rapidly optimise CDK1 and CDK2 inhibition. This study identified O⁶-cyclohexylmethoxy-2-(4'-sulphamoylanilino)purine (NU6102) as a potent and selective CDK2 inhibitor [3]. We have now extended this study and explored the SAR for this series by the synthesis and evaluation of 45 N²-substituted analogues of NU2058.

Our present studies have confirmed the requirement in this series for the hydrogen bonding N²-NH group, and for an aromatic N²-substituent to confer potency against CDK2. Previous X-ray crystallographic studies of NU6094 (2-anilino-6-cyclohexylmethoxypurine) bound to CDK2/cyclin A showed that its N²-aniline group packs against the CDK2 specificity surface on the CDK2 C-terminal domain just beyond the ATP binding site. Its potency derives in part from binding of the aniline ring to the CDK2

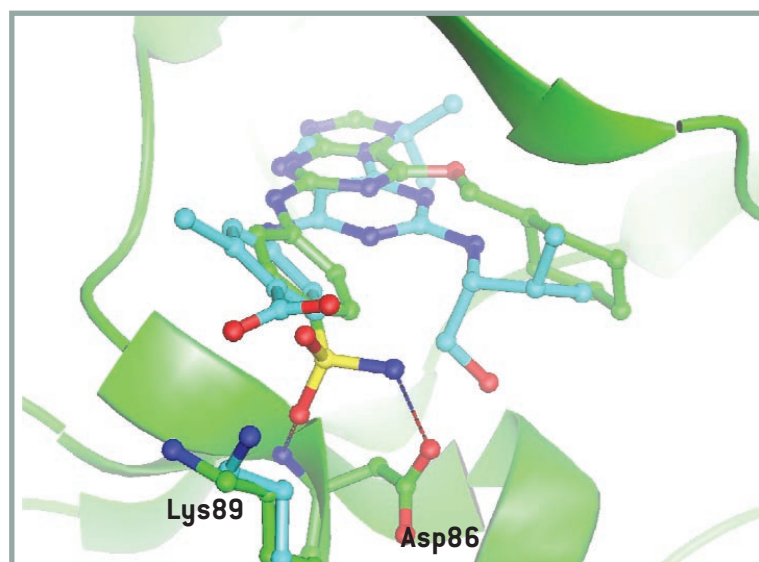
surface through a π - π stacking interaction with the peptide backbone between Asn 85 and Asp 86 (IC_{50} = 1.6 μ M and 1.0 μ M vs CDK1/cyclin B and CDK2/cyclin A [3]).

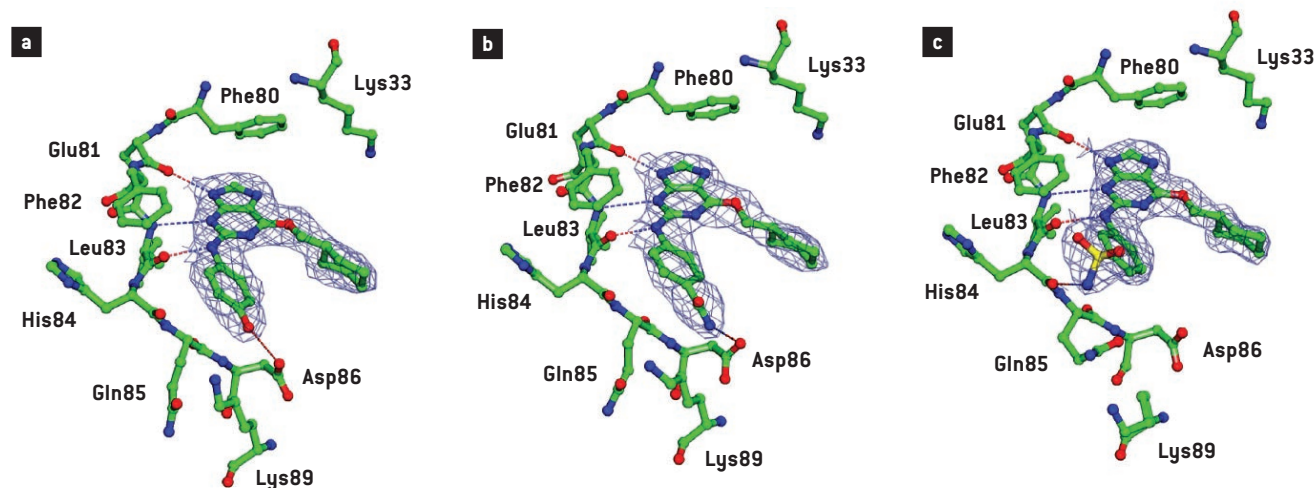
In this paper we have probed the effect of substitutions at the 3'- and 4'-positions on the aniline ring on inhibitor potency. The X-ray structure of purvalanol B bound to CDK2 showed that a favourable interaction between the inhibitor's 3'-chloro group and the enzyme is formed. The analogous N²-substituted 3'-chloro-anilino compound was prepared in our series but its activity was found to be no greater than that of the parent compound, NU6094. Similarly, the 3'-fluoro, 3'-bromo and 3', 5'-dichloro derivatives were no more active than NU6094 and the 3'-ethyl derivative was markedly less active. However, the 3'-hydroxymethyl derivative was more potent than NU6094 against both CDK 1 and 2. Given the poor activity of the 3'-ethyl derivative, the most persuasive explanation for the enhanced activity of the 3'-hydroxymethyl derivative in our series is that it is able to form a hydrogen bond with CDK2, presumably at a site conserved in CDK1 and CDK2. This residue could potentially be Asp86. Consistent with the need for a hydrogen bond donor at the 3'-position for enhanced activity, we found that both the 3'-methoxyanilino and 3'-methylmercaptoanilino compounds displayed similar activity to the 3'-chloro compound and the parent aniline.

Our structural studies suggested that additional potency could be derived by addition of a group at the 4'-position capable of donating a hydrogen bond. In the present study a number of derivatives with hydrogen bond donating groups at C-4 have been synthesised and characterised. Notably the 4'-hydroxy derivative (IC_{50} = 94 nM and 69 nM vs CDK1/cyclinB and CDK2/cyclinA3, respectively), 4'-monomethylsulfonamide derivative (IC_{50} = 9 nM and 7.0 nM vs CDK1/cyclinB and CDK2/cyclinA3, respectively), and the 4'-carboxamide derivative (IC_{50} = 67 nM and 64 nM vs CDK1/cyclinB and CDK2/cyclinA3, respectively) are particularly potent. To probe this site further, the 4'-methoxyanilino derivative was synthesised and, as predicted, this compound was markedly less active than the 4'-hydroxy derivative, showing approximately 10-fold less activity against both CDK1 and CDK2. The corresponding 4'-methylmercaptoanilino derivative was essentially inactive at 10 μ M. The corresponding 3'-methoxyanilino and 3'-methylmercaptoanilino derivatives were equipotent, but less active than the 4'-methoxy derivative.

In our original study a sulphamoyl group was substituted on the aniline ring at C-4 to generate NU6102, the most potent inhibitor in the series (IC_{50} = 9.5 nM and 5.4 nM vs CDK1/cyclinB and CDK2/cyclinA3, respectively). The NH₂ group of the sulfonamide donates a hydrogen bond to a side-chain oxygen of Asp86 (N26 to Asp86 OD2 = 2.9 Å) and one sulfonamide oxygen accepts a hydrogen bond from the backbone nitrogen of Asp86 (O24 to Asp86 NH = 3.1 Å). Hence compounds were synthesised to define in more detail the contributions of these two hydrogen bonds to activity against CDK1 and CDK2. The N-monomethyl derivative displayed similar activity to NU6102, whereas the *N,N*-dimethylsulfonamide was an order of magnitude less potent. These results strongly suggest that a single sulfonamide N-H is sufficient for optimal binding to the enzyme. The 4-methylsulfone derivative, which would also be unable to donate a hydrogen bond to a side-chain oxygen of Asp86, displayed similar activity to the *N,N*-dimethylsulfonamide, again consistent with the hypothesis that the activity of NU6102 is due to the

Figure 1. Comparison of the binding modes of NU6102 and Purvalanol B to monomeric CDK2. CDK2 bound to NU6102 is rendered in ribbon representation. The carbon atoms of Purvalanol B (PDB code 1CKP) and NU6102 are coloured cyan and green respectively. The side chains of Asp86 and Lys89 are included to highlight the interactions made between the NU6102 sulfonamide group and the side chain and backbone carbonyl group of Asp86 and between the Purvalanol B carboxyl group and the side chain of Lys89.





two H-bonds formed with Asp86. The 4'-methylsulfoxide was less active again than the 4-methyl sulfone derivative, suggesting that in addition to the loss of the NH hydrogen bond, the remaining sulphonyl oxygen can no longer adopt an optimal geometry for binding to the backbone NH of Asp86.

The targeting of Asp86 in CDK2 by hydrogen bonding groups has been observed in a number of other series of CDK inhibitors. In the quinazoline series H-bonding between a 3-anilino group and the side-chain carboxyl group of Asp 86 was observed. Interestingly, the oxindoles show a different pattern of activity to the anilino-purines. In this case, the unsubstituted sulfonamide, mono-, and disubstituted sulfonamides were found to be equipotent whilst cyclic sulfone derivatives suffered a small drop in activity, suggesting that a single H-bond formed between an aryl sulfonamide S=O to the backbone NH of Asp 86 was responsible for the gain in potency observed. The Asp86 residue has also been targeted in the flavopiridol mimicking benzilidene-benzofuran-3-one series, where a 10-fold gain in potency was observed on the introduction of a sulfonamide group at the position suggested by molecular modelling.

In general, the gains in potency observed for the anilino-purine series described here result from favourable hydrophobic packing between the aromatic aniline ring and an

area outside the ATP binding site of the CDK enzyme. Additional gains in potency are dependent on the formation of hydrogen bonds between carboxamide and sulfonamide groups, and Asp86, resulting in the identification of inhibitors with nanomolar potency. No direct interactions with Lys89, the residue originally targeted in the design of NU6102 have yet been seen. However, we have observed interactions with other areas of the protein that show sequence differences between CDK2 and CDK4 and these may offer further avenues to explore for gains in potency and selectivity beyond the often-targeted Asp86/Lys89 pair.

References

- [1] Noble M.E.M., Endicott J.A. and Johnson L.N., *Science*, **303**, 1800 (2004)
- [2] Arris C.E. *et al. J. Med. Chem.* **43**, 2797 (2000)
- [3] Davies T.G. *et al. Nat. Struct. Biol.* **9**, 745 (2002)

Figure 2. Binding of 4'- and 3'-substituted C²-anilino-O⁶-cyclohexylmethyl-purines to T160pCDK2/cyclinA3. Selected CDK2 residues are labelled and drawn in ball-and-stick representation. The final 2F_o-F_c density for each of the inhibitors is shown as a blue grid. Hydrogen bonds are indicated by dashed lines. **(a)**, **(b)** and **(c)**, 4'-hydroxy, 4'-carboxamide and 3'-sulfonamide substituted derivatives.



**MACHINE & PHOTON
SOURCE DEVELOPMENTS**

ELETTRA STATUS AND PROSPECTS

> D. Bulfone

Sincrotrone Trieste S.C.p.A., S.S. 14 km 163.5, in AREA Science Park, 34012 Trieste, ITALY

OPERATIONS

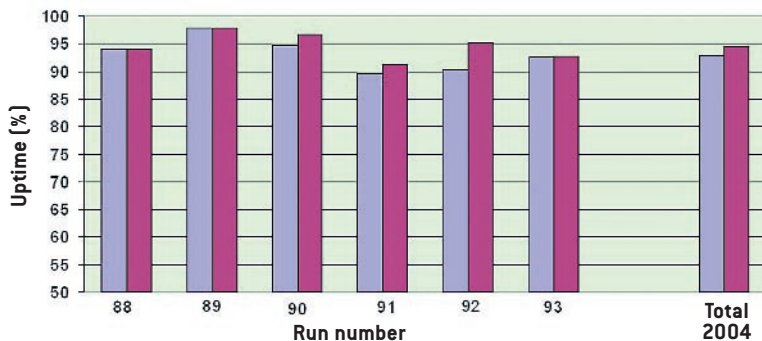
During 2004 ELETTRA operated for 6216 hours, of which 4664 (75%) dedicated to user experiments, with a user uptime (Figure 1) of 93% (94.5% excluding beam losses due to storms). In addition to storms, the major causes of downtime were due to delays during the injection phase and to magnet power supply faults. The machine was operated at 2 GeV (320 mA injected current) for 73.6% of its user time whereas the 26.4% was at 2.4 GeV (140 mA injected current). Each of the six 2004 runs started with some days of machine physics and storage ring FEL shifts, which preluded to the 2.4 GeV operation periods. Switching between 2.4 to 2.0 GeV also occurred during a day of machine physics studies. The standard operation mode was multi-bunch with 95% contiguous filling. The superconducting third harmonic cavity and the transverse multi-bunch feedback systems were routinely active so that an electron beam completely free of coupled bunch instabilities with enhanced lifetime was produced, which resulted in a high brightness photon beam with increased integrated flux for the users. A complete realignment of the machine was performed in 2004. The outcome showed an overall improvement on operability due to minimization of the linear coupling and reduction of optical asym-

metries. The few-bunch operational mode was also requested in 2004 for about 5% of the user-dedicated time. The few-bunch mode consists of four equidistant bunches at 2 GeV with a total initial current of 32 mA and a few hours lifetime. In this mode of operation the ring is refilled every eight hours.

6168 hours of operations are foreseen in 2005, of which 4832 dedicated to user experiments, with 72.7% and 27.3% relative amount of 2 and 2.4 GeV shifts respectively. A similar quota of few-bunch shifts has been requested as in 2004. The user uptime for the first half of 2005 is 94.7% (96% excluding beam losses due to storms).

In parallel to improved operations, the continuous development of the machine and the refinement of the quality of the delivered beam are supported by major upgrades and by specific projects. The radio frequency (RF) plant upgrade (see these Highlights for more information), the global orbit feedback and the full energy injector projects are the most significant.

Figure 1. Blue: user uptime in 2004, with partial uptime during the six runs of the year. Red: user uptime excluding beam losses due to storms.



GLOBAL ORBIT FEEDBACK

After the cure of coupled bunch instabilities, which, as described above, led to an increase of the photon beam brightness, efforts are focusing on orbit stability issues. Fast local feedback systems using dedicated low-gap Beam Position Monitors (BPM) have been developed and installed in straight section 2 and 7 to improve the stability of the electron beam at the Insertion Device (ID) source points. Remarkable sub-micron/sub-microrad beam stability has been achieved in a 0-250 Hz frequency range by combining a PID (Proportional Integral Derivative) regulator together with dedicated selective filters centered on the periodic components of the noise spectrum.

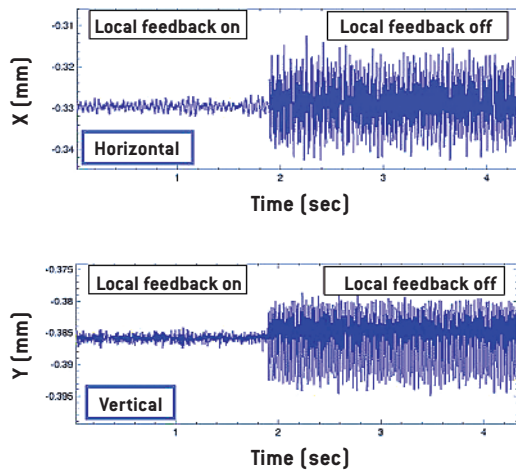


Figure 2. Horizontal and vertical beam position (low-pass filtered at 250 Hz) measured by a low-gap BPM in section 2 with local feedback on/off.

The feedback reduces the *rms* of the beam angle at the ID center below $0.2 \mu\text{rad}$ in both the horizontal and vertical plane.

Figure 2 shows the effect of the local feedback when the loop is closed.

Although several local feedback systems may be installed, they would only correct the orbit at ID but not at bending magnet source points; moreover, cross talk between local control loops could become an issue with many local feedbacks installed. A global orbit correction scheme has therefore been adopted, which has the additional advantage of being more effective in correcting orbit distortions with optimized corrector strengths. A global feedback system employing an opportunely inverted response matrix offers more flexibility in the implementation of correction algorithms, being able to perform “flat” global correction, weighted correction, local closed bump correction and even more sophisticated schemes, if necessary.

The designed fast global orbit feedback [1] will take advantage of all of the 96 existing rhomboidal BPMs and 82 corrector magnets (each equipped with horizontal and vertical coils) of the ELETTRA storage ring. The existing BPM electronics will be upgraded with digital detectors providing position measurements with sub-micron resolution and fast data acquisition rate. A distributed processing system based on twelve local stations equipped with general purpose VME CPU boards will share beam position data by means of a real-time fiber optic network and set the calculated correc-

tion values on the corrector power supplies through dedicated analog links. Each local station manages the BPMs and correctors of one machine sector. A 10 kHz feedback repetition rate has been chosen, which minimizes latency time.

The Singular Value Decomposition (SVD) algorithm will be used to invert the 96×82 response matrix in the global correction scheme. Simulations are under way to study the correction efficiency with different variants of the basic SVD algorithm, including BPM weighting and singular values reduction. Both the measured and the theoretical matrices have been determined. The plot of the singular values in descending order (Figure 3a) suggests that a number of them can be neglected at the cost of a slight reduction of the correction efficiency. Figure 3b reports the simulated correction efficiency as a function of the number of singular values retained in the matrix inversion. The vertical axis is the ratio between the *rms* of the residual and the original orbit distortion.

The upgrade of the BPM electronics will be completed by the end of 2006. The commissioning of the fast global orbit feedback will follow in the first quarter of 2007.

FULL ENERGY INJECTOR

The construction phase of the ELETTRA full energy injector has started. During 2004

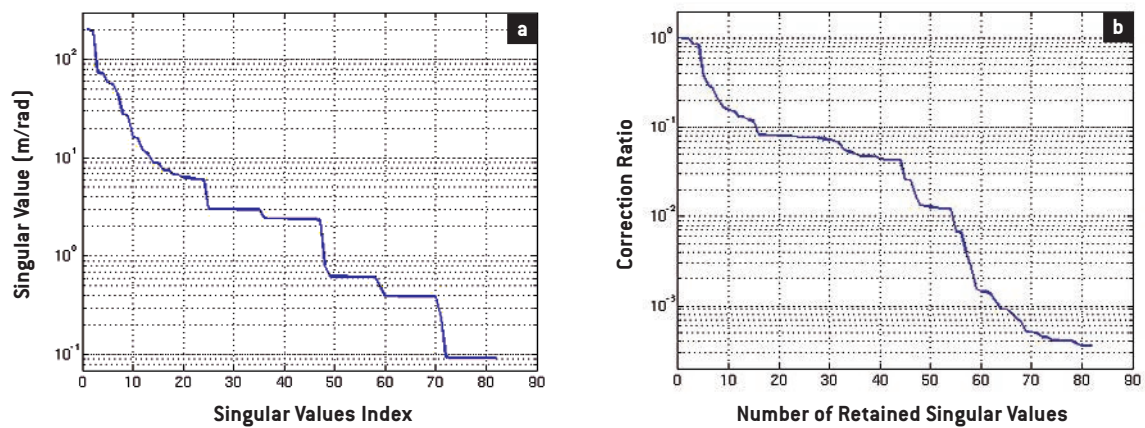


Figure 3. Singular values of the response matrix in descending order **(a)**, ratio between the *rms* of the residual and the original orbit distortion as a function of the number of singular values retained in the SVD matrix inversion **(b)**.

a general design review took place, which led to a new, cost effective concept of the accelerator building and technical facilities.

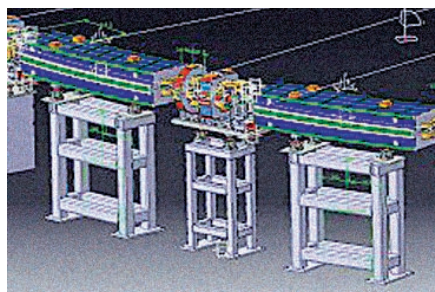
The booster synchrotron is the core component of the new injector, which is made up of a pre-injector linac where the beam is accelerated to 100 MeV, a transfer line from the linac to the booster, the booster itself where the beam energy is ramped from 100 MeV up to a maximum value of 2.5 GeV and finally the extraction transfer line that takes the beam from the booster to the injection point into the ELETTRA storage ring. The maximum booster energy ramping frequency is 3.125 Hz. The magnetic lattice of the booster has a FODO structure with missing magnets; the circumference is 118.8 m. There are 28 dipole, 36 quadrupole, 24 sextupole and 22 steerer magnets. Figure 4 shows a view of the different booster magnet types mounted on girders. In order to minimize the equilibrium emittance at 2.5 GeV, the length of the bending magnets has been

increased, with respect to the initial design, up to 2.0 m. With the normal optics the equilibrium emittance value at 2.5 GeV is then equal to 226 nmrad, which can be further reduced to 166 nmrad by adopting the low emittance optics.

The new injector complex will be hosted in a building at the center of the existing storage ring facility. The building has been significantly simplified with the unification of the accelerator tunnel and the technical gallery. This also allowed simplifying the cooling and air conditioning plants, with an important cost reduction. Building construction started in September 2005.

The booster magnets, ordered in Summer 2005, will be delivered during the last quarter of 2006. Booster commissioning will start in Spring 2007. During the following summer the ELETTRA storage ring will be connected to the transfer line coming from the booster. In Autumn 2007 ELETTRA will be filled, for the first time, with electrons at the nominal energies of 2.0 or 2.4 GeV. It will then be possible to operate in top-up mode, keeping the beam current in the storage ring constant within, for instance, a dead band of ± 1.0 mA over a 330 mA nominal value. The required injected electron charge is expected to be about 0.1 nC in a single bunch. Top-up will provide infinite beam lifetime, stable flux and excellent thermal stability to the beamlines.

Figure 4. View of the different booster magnet types mounted on girders.



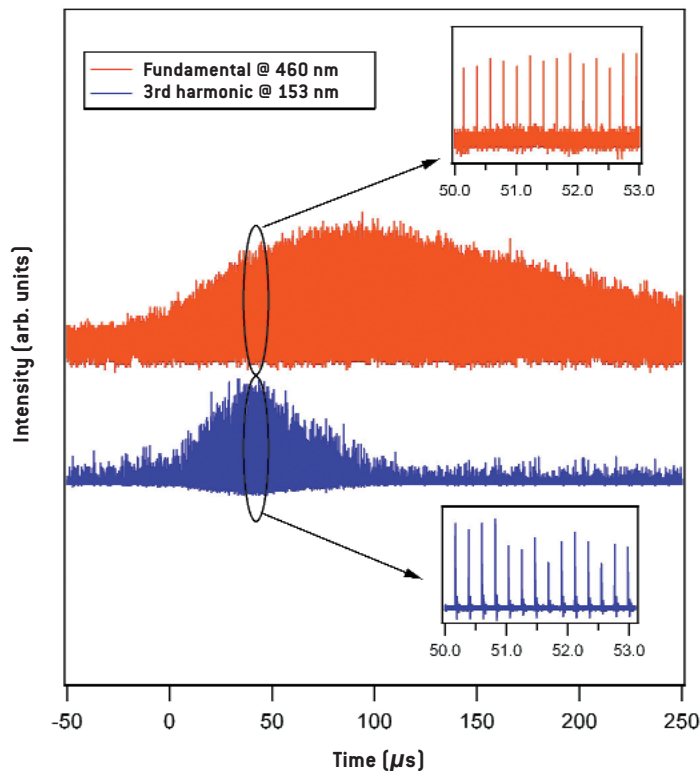


Figure 5. Correlated evolution of the fundamental (**upper trace**) and third harmonic (**lower trace**) FEL macro pulses.

STORAGE RING FEL

A significant improvement in the fabrication technique of the optical cavity mirrors allowed for producing FEL radiation down to 177 nm, which is the shortest wavelength ever obtained by a FEL in an oscillator configuration.

Further studies of coherent harmonic generation were performed, successfully generating 160 nm radiation in the third harmonic of the FEL operated in Q-switched mode (Figure 5). Similarly to what observed at 220 nm (see Highlights '03-'04), the harmonic was measured to grow about three times faster than the fundamental, in agreement with the theoretical predictions. This can be now considered a viable method to reach the shortest wavelengths in the VUV spectral range. However, the actual power emitted by the FEL in this configuration proved to be difficult to measure, due to strong contamination from the more intense fundamental component.

In order to improve the Q-switching setup [2], plans were developed to obtain this

operating regime using optical switching instead of detuning the FEL by RF modulation. A rotating disk (chopper) was designed, built and installed. The first observation of the giant-pulses generated by this setup confirmed the principle. It is believed that the intensity of the optically-generated pulses will be higher than achieved with the RF-modulation technique, since no perturbation is induced to the electron beam. Enhancements in the stabilization of the FEL intensity by the use of closed-loop feedback systems are described in these Highlights.

References

- [1] M. Lonza et al., *Design of a Fast Global Orbit Feedback System for the ELETTRA Storage Ring*, Proc. International Conference on Accelerator and Large Experimental Physics Control Systems, Geneva, Switzerland (2005)
- [2] G. De Ninno et al., *Nucl. Instr. And Meth. A* **528**, 278 (2004)

LONGITUDINAL BEAM DYNAMICS WITH MICROBUNCHING INSTABILITY IN THE FERMI LINAC

> S. Di Mitri

Sincrotrone Trieste S.C.p.A., S.S. 14 km 163.5, in AREA Science Park, 34012 Trieste, ITALY

MICROBUNCHING INSTABILITY

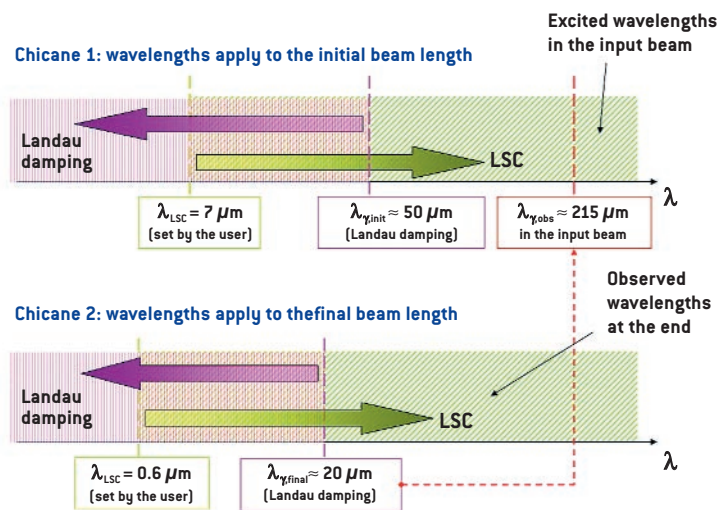
The FERMI@ELETTRA project [1] relies on the acceleration of an electron beam with reduced beam sizes in the upgraded 1.2 GeV ELETTRA linac. The numerical code Elegant allows simulating the longitudinal beam dynamics, taking into account collective effects like longitudinal space charge (LSC) and coherent synchrotron radiation (CSR) [2].

LSC is driven by high charge density. It modulates the beam energy distribution, which transforms into spatial modulation and vice versa during the beam motion. LSC can be an important issue for the beam dynamics in Fermi, even at high energy, because the beam transverse and longitudinal dimensions are quite small in order to make the free electron laser (FEL) process more efficient - it requires small transverse beam size, divergence and high current.

CSR is synchrotron radiation emitted by the electrons at wavelengths comparable with the beam length. The emission happens in the two chicanes, each made of four dipoles, inserted in the Fermi linac that compress the beam length and therefore increase the current. CSR emission is enhanced by current spikes, which grow during the compression and originate from three different sources: (i) statistical noise in the particle distribution; (ii) spatial modulation generated by LSC through energy-spatial oscillations; (iii) energy modulation generated by LSC, which transforms into spatial modulation when the beam travels in a dipole (the motion on a curved path couples the momentum of an electron with its longitudinal position along the bunch). Then, the radiation emitted by current spikes modulates the energy distribution of the electron beam itself - tailing electrons

Figure 1. Mechanism of growth and suppression of MBI through Landau damping in the first and second chicane of the Fermi linac. Predictions from linear theory. λ_{LSC} is the *minimum* wavelength amplified by LSC, while λ_{γ} is the *maximum* wavelength suppressed by Landau damping. As a result, all $\lambda \geq \lambda_{\gamma}$ will be enhanced by LSC after the compression and thus visible in the resulting

energy and spatial distributions. Note that after the second chicane only $\lambda \geq 20 \mu\text{m}$ can be amplified and thus observed in the final beam. Actually, they correspond to perturbations in the distributions of the initial (uncompressed) beam characterized by wavelengths equal to $\lambda_{\gamma,final}$ multiplied by the total compression factor 10.5, that is $\lambda_{\gamma,obs} \approx 215 \mu\text{m}$ in the input beam.



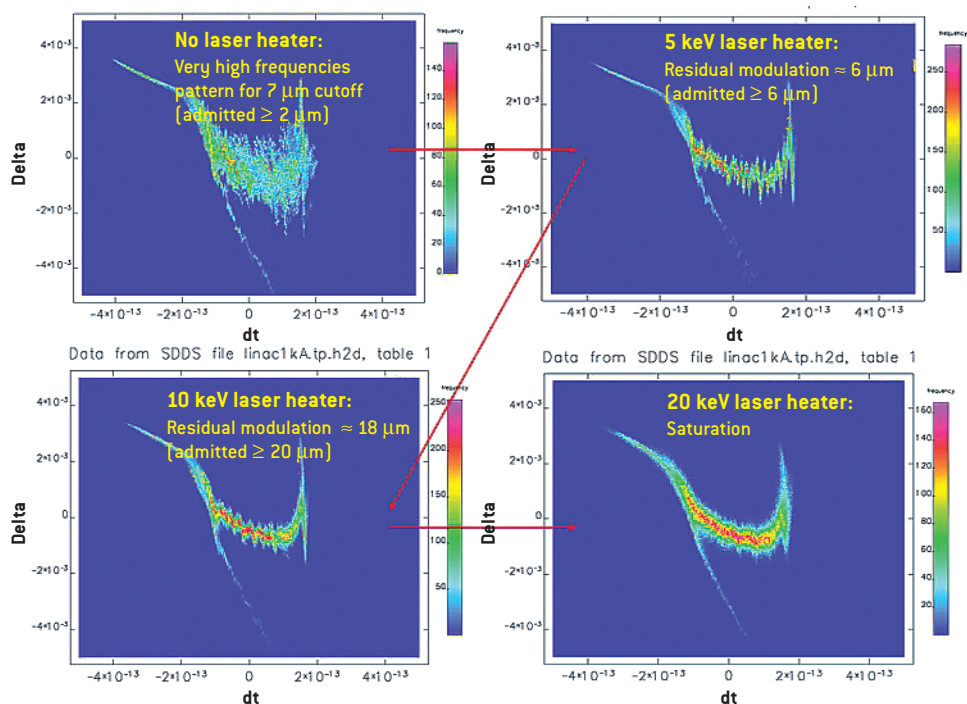


Figure 2. Output beam longitudinal phase space, tracked in Elegant. Contour plot of the relative momentum spread vs. temporal position along the bunch of 10^6 macro particles at the end of the linac (after two compressions). As the energy spread provided by the laser heater increases, suppression of MBI covers longer wavelengths of modulation. Shorter wavelengths [upper left and upper right plots] degrade more the phase space, increasing the energy spread and strongly modulating the current distribution. Spectral analysis applied to the tracking output (reported in the plots) agrees with theoretical predictions of the linear approximation [admitted values]. As a result, a 20 keV rms laser heater is sufficient to completely damp the instability [saturation], but it provides a final uncorrelated energy spread of about 200 keV.

emit radiation that hurts leading electrons - or enhances an already existent energy modulation. Finally, the curved path in a dipole contributes to transform again energy modulation into spatial modulation (*microbunching*), providing the growth of the modulation amplitudes that is the microbunching instability (MBI).

LANDAU DAMPING

MBI starts from and finally degrades the energy (or momentum) distribution of the electron beam. The beam affected by MBI shows a modulation in the space of coordinates defined by the relative momentum spread vs. longitudinal position in the bunch, called *longitudinal phase space*. For this reason, MBI can be counteracted just by increasing the uncorrelated momentum spread of the electron beam (the thickness of the beam phase space plots in Figure 2). If the uncorrelated momentum spread is sufficiently larger than the amplitude of modulation due to the instability, the amplitude cannot grow anymore and the instability is effectively damped. This kind of instability suppression is a specific application of

a more general process called *Landau damping*. Actually, Landau damping is a spontaneous effect already acting during the beam compression, since the uncorrelated energy spread naturally increases when longitudinal dimension converts into longitudinal momentum. Thus, beam compression contributes to the microbunching with CSR, but at the same time it sets a limit to the growth of the instability. The disadvantage of Landau damping is that the resulting beam may have quite a large momentum spread, in contrast with the FEL requirements. A compromise is needed between small energy spread and instability suppression.

In most cases, the natural increase of the energy spread during compression is not sufficient to suppress the instability at the desired level. For this reason, a *laser heater* is foreseen in the Fermi linac just before the first chicane in order to further increase the energy spread. A laser heater essentially consists of an undulator, in which the electron beam interacts with the electromagnetic radiation, resulting in an increase of the momentum spread by the desired amount.

Figure 3. Result of Elegant tracking with 10^6 macro particles. Longitudinal phase space (upper left), energy distribution (upper right, energy spread vs. number of particles) and current distribution (bottom left) at the end of the linac, after two compressions and 8 keV rms laser heater added at the beginning. LSC is not implemented, while CSR is. Simulation gives resulting beam parameters usable for FEL where laser heater performance is based on analytical predictions.

SUPPRESSION OF THE INSTABILITY

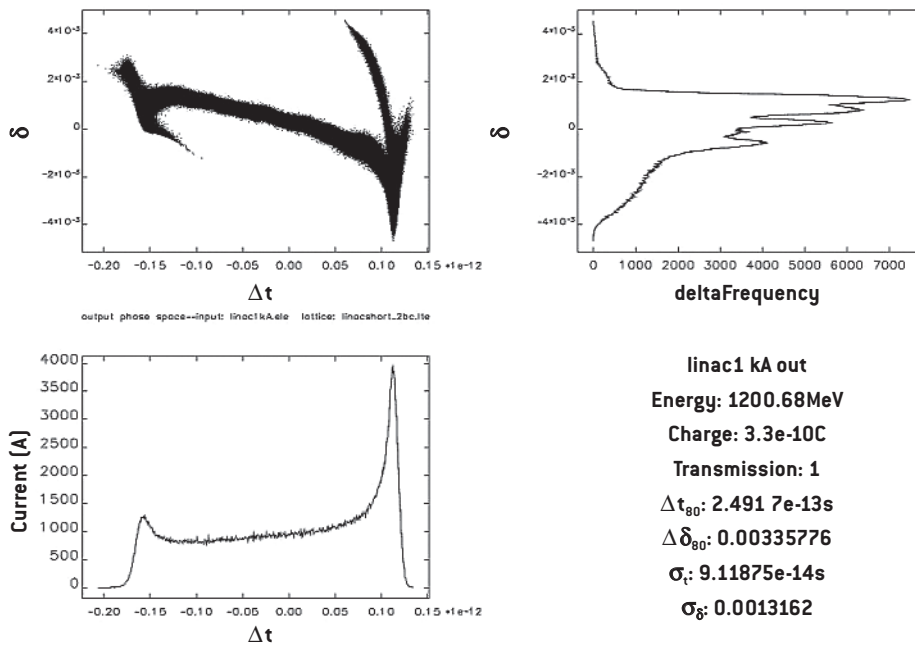
LSC is treated as a longitudinal impedance characterized by a lower threshold (set by the user) in wavelength of the amplified modulation [2]. In practice, it is a low pass filter that amplifies all wavelengths *longer* than λ_{LSC} (Figure 1). On the other hand, the uncorrelated energy spread of the electron beam suppresses by Landau damping all modulations with wavelengths *shorter* than λ_γ (Figure 1), where λ_γ is a threshold depending on the beam compression parameters of the chicane [3]:

$$\lambda_g = (2\pi \cdot R_{56} \cdot \sigma_{\delta,uncorr}) / (1 + h \cdot R_{56})$$

In particular, R_{56} is a term describing the optical properties of the chicane: it links the momentum spread of an electron to its longitudinal position in the bunch; $[1/(1 + h \cdot R_{56})]$ is the *compression factor* in the linear approximation, while $[\sigma_{\delta,uncorr} / (1 + h \cdot R_{56})]$ is the linearly transformed (compressed) energy spread at the end of the chicane.

Figure 1 illustrates the mechanism of growth and suppression of MBI according to the linear theory [3]. The effect of a laser heater adding 7 keV rms to the uncorrelated energy spread of the electron beam is

included. When the beam passes in the first chicane (upper plot), LSC has already amplified all $\lambda_{LSC} \geq 7 \mu\text{m}$ (very small wavelengths compared to the initial bunch length of 1.8 mm). During compression, $\sigma_{\delta,uncorr}$ increases and suppresses all spatial modulations with $\lambda_\gamma \leq 50 \mu\text{m}$. Actually, wavelengths observed after compression are themselves compressed by the same compression factor applied to the beam, i.e. 3.5 for the first chicane. Thus, only $\lambda \geq 50 \mu\text{m}$ in the input beam are allowed through the chicane and observed at wavelengths $\lambda_{obs} \geq (50 \mu\text{m} / 3.5) \approx 14 \mu\text{m}$. Analogous considerations apply to the second chicane (lower plot), where only modulations of wavelengths $\lambda_{obs} \geq 20 \mu\text{m}$ (compressed value) are allowed, given the compression factor of ten. They correspond to spatial modulations in the initial uncompressed beam of about 215 μm . By comparing the two cases, the second chicane has a stronger effect in suppressing the instability: only $\lambda_{LSC} \geq 215 \mu\text{m}$ in the input beam are allowed by the second chicane (they overcome the provided Landau damping), corresponding to output wavelengths $\lambda_{obs} \geq 20 \mu\text{m}$ observed at the end of the linac.



Bunch charge	330	pC
Bunch duration (full width)	6	ps
Peak current	75	A
Uncorrelated energy spread	3	keV
Normalised emittance (rms)	0.8	μm
Laser heater energy spread (rms)	8	keV
Compression factor in 1st chicane	3.5	
Compression factor in 2nd chicane	3.0	

Table 1. Parameters of the input beam and dynamics for the “short bunch” option in the two-compression scheme of the FERMI@ELETTRA project. All values, with the exception of the bunch

duration, refer to the beam core that is the central part of the beam used for the FEL process.

Beam final energy	1.2	GeV
Bunch duration (full width)	200	fs
Peak current	900	A
Slice energy spread (rms)	130	keV
Normalised emittance (rms)	0.9	μm

Table 2. Parameters of the output beam for the “short bunch” option in the two-compression scheme of the FERMI@ELETTRA project. All values refer to the beam core. Slice energy spread is the uncorrelated one but

includes a small contribution from the correlation between particles momentum and longitudinal position. The electron beam parameters satisfy the requirements for the FEL process.

APPLICATION TO THE “SHORT BUNCH” OPTION IN THE FERMI@ELETTRA PROJECT

Studies performed through theoretical calculations and Elegant tracking have been applied to the “short bunch” option foreseen in the Fermi project [1]. Parameters of the input beam are listed in Table1. Elegant simulation of the MBI results difficult, because tracking is limited to a relatively small number of macro particles with respect to the actual number of electrons in the beam. This artificially increases the shot noise in the tracking beyond the level it is in the real beam and, as a consequence, the effect of LSC is overestimated. For this reason, it was decided to use analytical calculations to predict the necessary contribution of uncorrelated energy spread from the laser heater that can at the same time effectively suppress MBI and optimize the energy spread at the end of the linac. Figure 3 shows the longitudinal phase space and its projections on the energy and current distributions after two compressions; laser heater furnishes 8 keV rms to the uncom-

pressed beam. The resulting characteristics of the beam core (*slice* parameters) are listed in Table 2. They satisfy the requirements for the FEL process.

References

[1] Bocchetta C. J. *et al.*, *FERMI@ELETTRA: A Seeded Harmonic Cascade FEL for EUV and Soft X-Rays*, Proceedings of the 2005 Free-Electron Laser Conference, Stanford, CA, FEL2005 (2005), to be published
 [2] Borland M., *Elegant: A Flexible SDDS-Compliant Code for Accelerator Simulation*, APS LS-287 (2000)
 [3] Huang Z. *et al.*, *Phys. Rev. ST-AB*, **7**, 074401 (2004)

THE RADIO FREQUENCY (RF) UPGRADE PROJECT

> A. Fabris, C. Pasotti

Sincrotrone Trieste S.C.p.A., S.S. 14 km 163.5, in AREA Science Park, 34012 Trieste, ITALY

The existing ELETTRA storage ring RF system has had no major upgrades since its initial installation in 1993. It is composed of four independent 500 MHz 60 kW cw plants, each one powering a single cell ELETTRA type cavity. Each power amplifier is equipped with a 60 kW klystron.

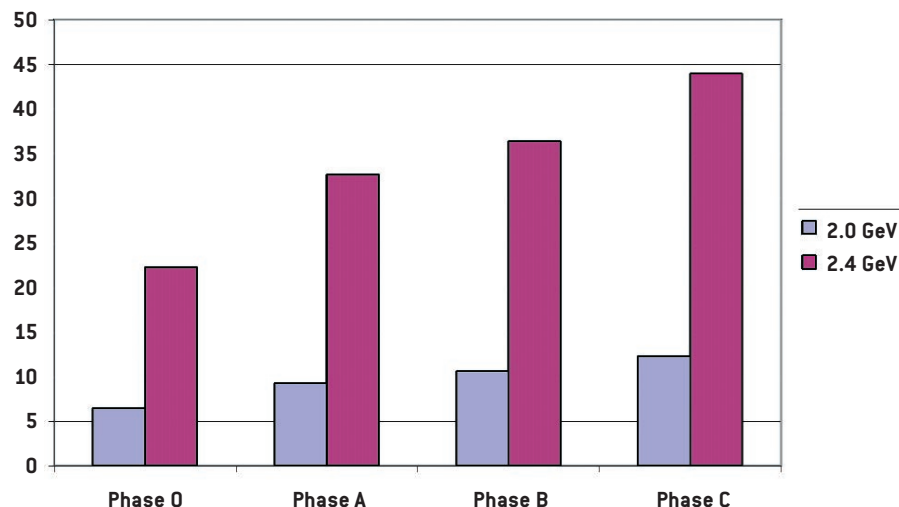
The increase in the number of insertion devices during the last years has considerably raised the demand of RF power compared to the original requirements, spoiling the safety margins of the RF system. The project of upgrade of the existing storage ring RF system will provide the necessary safety margins, when all the insertion devices are operational (with a slight increase in the Touschek lifetime) and in view of the possible increase of beam current and energy. The design strategy has taken into account the need of minimizing the interference with the operation of the machine and the requirement of keeping unchanged the space for the RF components in the storage ring. Reliability, long time between

failures and short repairing time have been fundamental issues in the design philosophy. All these considerations have led to a multi-stage approach [1].

The first phase (phase A) foresees the upgrade to 150 kW of one of the existing 60 kW plants. During the following stages the same activities will be repeated for one plant (phase B) and for the remaining two plants (phase C). At the end 600 kW of RF power will be available, with a consequent increase of the total RF voltage and power available to compensate beam losses. The evolution of Touschek lifetime in the different phases is shown in Figure 1.

Phase A is now in progress. It requires basically the replacement of one 60 kW amplifier with a 150 kW one and the replacement (already performed) of the associated cavity with a similar ELETTRA type one equipped with an upgraded cooling system. Afterwards, the old 60 kW amplifier will be used to build the new booster RF power plant.

Figure 1. Evolution of Touschek lifetime at the usual operating currents and energies (vertical scale in hours). Phase 0 is the present situation, before the upgrade. The effect of the third harmonic superconducting cavity is not included.



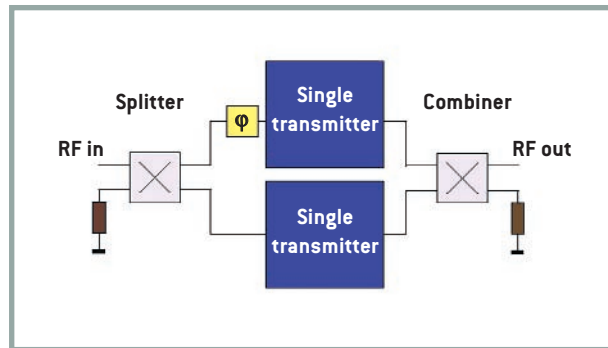


Figure 2. Block diagram of the 150 kW amplifier.

For the 150 kW amplifier, being the RF frequency (500 MHz) well in the UHF range, one could take advantage of the solutions adopted in professional broadcasting, profiting of their return of experience. For this reason, the power amplifier will be acquired as a turnkey system from industry. It will combine two 80 kW IOTs (inductive output tubes) transmitters (Figure 2). This is a novel solution for a light source although it has been adopted for new machines in construction, as DIAMOND in the UK. Each of the two IOTs will have the possibility to work standalone, thus increasing operational flexibility.

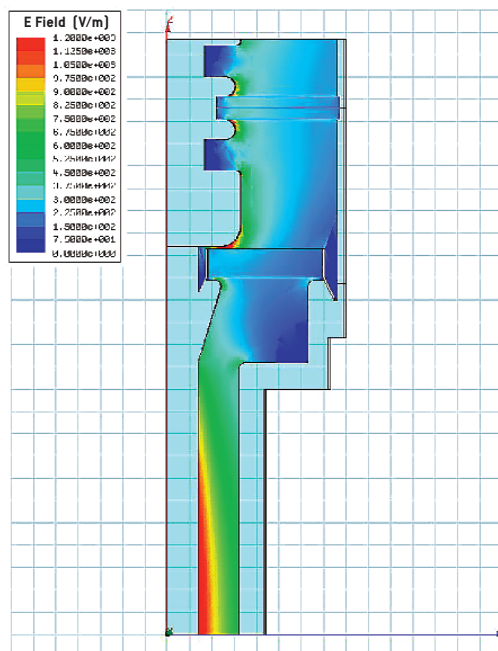
The IOT combines aspects of gridded tube and klystron technology. The main difference compared to klystrons is that the electron beam is density modulated, while in a klystron it is velocity modulated. IOTs are widely used in UHF TV applications where they have almost completely replaced klystrons as the preferred tube for the final amplifying stage. This is mainly due to their basic higher efficiency and moderate loss of efficiency at reduced power levels. Efficiency is typically in the range from 65 to 70% and for drive modulation it does not drop significantly in the power range of interest for ELETTRA (generally 2 to 3 dB). Compared to klystrons, IOTs also offer other advantages in terms of electrical and cooling requirements, physical dimensions, maintenance and replacement time. The main disadvantage is related to the lower gain, which requires a higher power solid-state preamplifier.

The high voltage power supply for each IOT will be a switched mode power supply. The main advantages of such solution are the lower ripple and the stabilization of the beam voltage independently of output power and mains input variations. This reflects on the phase stability of the output RF power, which could influence the quality of the beam stored in ELETTRA. A further advantage of the solution adopted for the power supply is that the use of oil filled components (such as transformers or capacitors) and of crowbar protecting devices is avoided.

The combining system will consist of a switchless combiner. This device is made of two hybrids and a variable phase shifter. It gives the advantage of only 3 dB losses in case one tube is out of service and allows four modes of operation, giving the possibility of the so called hot adjustment of the system. This means that, for example, the maintenance of one tube could be done while the other is in operation, without interference. These types of combiners have been used for years and their principle of operation is now completely understood.

Due to the power level, the transmission of RF power from the amplifier to the cavity will have to be performed using a waveguide system instead of the coaxial one now in use. Beside the standard waveguide components, such as high power circulator and waveguide lines, a transition from waveguide to coaxial is necessary to interface to the cavity input power coupler. This coaxial to waveguide transition has been studied,

Figure 3. Input power coupler peak electric field at 500 MHz.



together with the coaxial input power coupler and the adapter element to the standard coaxial size, in order to improve the performance of the whole system both at the fundamental and higher order modes (HOMs) frequencies [2]. The input power coupler was successfully tested a few years ago at 200 kW 500 MHz at DESY, even though not in its final layout. A controlled coupled bunch longitudinal instability, in fact, is routinely excited during the injection and ramping procedures of the storage ring to smooth operations and relax requirements on the optics. This is achieved using a cavity HOM. In addition to the power from the amplifier, the analysis has therefore to take into account the possible extra power induced by the beam at HOM frequencies.

The three elements (input power coupler, adapter element to standard coaxial size, waveguide to coax transition) have been studied as a self-consistent system and simulated with the simulation code Ansoft HFSS v.9.1 (Figure 3). The performances of the structure are then optimized to lower as much as possible the impact of the HOMs field and to increase the efficiency of the

cooling of the inner conductor in order to improve the power transmission at the fundamental frequency. The feasibility study is almost completed and the interaction with industries for the construction of a prototype is going on.

As for the time schedule of the RF upgrade project, the first phase is now in the construction stage. The installation of the power amplifier is planned in the second quarter of 2006. The connection of the amplifier to the cavity and the completion of the first phase will be performed by the end of 2006.

References

- [1] A. Fabris et al., *ELETTRA RF System Upgrade Project*, Proc. European Particle Accelerator Conference, Paris, France, pp. 2142-2144, (2002)
- [2] C. Pasotti et al., *500 MHz Coaxial Transition between the ELETTRA Input Power Coupler and the Transmission Waveguide*, Proc. Particle Accelerator Conference, Knoxville, USA, (2005)

TOWARDS THE STABILIZATION OF THE ELETTRA STORAGE-RING FREE-ELECTRON LASER

> G. De Ninno, E. Allaria, F. Curbis, B. Diviacco, M. Trovò

Sincrotrone Trieste S.C.p.A., S.S. 14 km 163.5, in AREA Science Park, 34012 Trieste, ITALY

> A. Antoniazzi, D. Fanelli

Dipartimento di Energetica, Università di Firenze, 50139 Firenze, ITALY

ABSTRACT

The ultimate performance of a storage-ring free-electron laser depends on the possibility of understanding and controlling the coupled electron-beam and laser dynamics. For this purpose, we have developed a simple theoretical model, which proved to be able to provide insight into the evolution of the laser intensity. In this framework, we have proposed the possibility of utilizing different kind of control systems to create or enlarge the region of stable signal. A derivative closed-loop feedback has been implemented on the ELETTRA storage-ring free-electron laser. We review the obtained results, which fully confirm our predictions.

1. THE NATURAL REGIME OF THE ELETTRA STORAGE-RING FREE-ELECTRON LASER

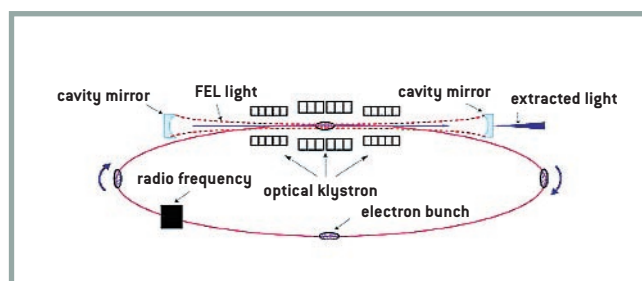
In a storage-ring free-electron laser (SRFEL) the light emitted by electrons when passing through the static and periodic magnetic field generated by an optical klystron [1] is stored in an optical cavity and amplified during successive interactions with the electron beam (Figure 1). The amplification is obtained to the detriment of the electron beam energy, whose spread increases with the growth of the intra-cavity power. This heating effect leads to the reduction of the amplification gain until the latter reaches the level of the cavity losses (laser saturation). The electron beam energy is turn-by-turn recovered by means of the radio frequency cavities, which supply the electrons with the energy they lose due to synchrotron and FEL radiation.

Since it originates from synchrotron radiation, the laser temporal structure is naturally characterized by a train of micro-pulses (whose duration is of the order of tens of ps)

separated by the inter-bunch temporal distance (hundred of ns). On a larger (millisecond) temporal scale, the FEL dynamics depends strongly on the longitudinal overlap between the electron bunch(es) and the laser pulses at each pass inside the optical klystron. A given temporal detuning, i.e. a difference between the electron beam revolution period and the photons round trip inside the optical cavity, leads to a cumulative delay between the electrons and the laser pulses. In the ideal conditions, i.e. with a perfectly stable electron beam, the laser intensity appears “continuous wave” (“cw”) for a weak or strong detuning, and shows a stable pulsed behavior for an intermediate detuning amount [2,3].

Thanks to the combination of high-quality electron beam (i.e. low emittance, short bunch length) [4], adjustable undulator parameters [5] and robustness of the high-reflectivity mirrors of the optical cavity [6], the SRFEL at ELETTRA can be operated in the large electron beam energy range from 0.9 to 1.5 GeV, the latter being the highest energy used so far for a SRFEL. This flexibility allowed to extend the accessible spectral range down to the VUV and to improve the FEL compatibility with other synchrotron radiation users interested in a few bunch filling of the storage ring.

Figure 1. Schematic layout of a storage-ring free-electron laser.



However, due to its high sensitivity to different kind of instabilities (coupled-bunch instabilities, main-induced modulations, mechanical vibrations, etc.), the ELETTRA SRFEL generally shows a noisy behavior over the whole detuning region (Figure 2a). The analysis of the spectrum (Figure 2b) brings into evidence the strong influence of electron beam instabilities on the laser dynamics. The noisy behavior is characterized by four strong components. The two peaks at 300 and 350 Hz are induced by the “natural” laser response to detuning. The fact that two different frequencies are observed may result from a variation of the detuning during the period of signal acquisition (100 ms). The peaks at 50 and 100 Hz are systematically observed and can be related to instabilities perturbing the dynamics of the electron beam.

Figure 2. [a]: Typical temporal behavior of the ELETTRA SRFEL intensity close to the perfect laser electron synchronism; **[b]:** Fourier analysis of the signal shown in [a].

Figure 3. [a]: Temporal behavior of the ELETTRA SRFEL intensity without (left part) and with (right part) derivative feedback; **[b]:** Fourier analysis of the signal shown in left part of Figure [a]; **[c]:** Fourier analysis of the signal shown in right part of Figure [a]. FEL operated with a detuning of few femtoseconds.

2. THE MODEL

As a result of a deep theoretical investigation of the system dynamics we proposed different methods for improving the SRFEL stability. The study is based on the following model. A system of three rate equations is used to describe the coupled evolution of the electromagnetic field and the electron beam [7]. At each passage inside the optical cavity, the laser intensity profile, $I_n(\tau)$, is modified according to:

$$I_{n+1}(\tau) = R^2 I_n(\tau - \varepsilon) [1 + g_n(\tau)] + i_s(\tau) \quad (1)$$

where τ is the temporal position with respect to the centroid of the electron bunch; $R (< 1)$ is the reflectivity of the optical cavity mirrors; ε is the detuning parameter, i.e. the dif-

ference between the period of the photons inside the cavity and the electron revolution period divided by the numbers of bunches; $i_s(\tau)$ accounts for the profile of the spontaneous emission of the optical klystron. The gain $g_n(\tau)$ is given by:

$$g_n(\tau) = g_i \frac{\sigma_0}{\sigma_n} \exp\left[-\frac{\sigma_n^2 - \sigma_0^2}{2\sigma_0^2}\right] \exp\left[-\frac{\tau^2}{2\sigma_{\tau,n}}\right] \quad (2)$$

where g_i and σ_0 are, respectively, the initial (laser-off) peak gain and beam energy spread; σ_n and $\sigma_{\tau,n}$ are the energy spread and bunch length after the n th interaction. The first exponential in the right-hand side of equation (2) accounts for the modulation rate of the optical-klystron spectrum, while the second one reproduces the temporal profile of the electron bunch distribution, assumed to be Gaussian. The equation that governs the evolution of the laser-induced energy spread is:

$$\sigma_{n+1}^2 = \sigma_n^2 + \frac{2\Delta T'}{\tau_s} (\gamma I_n + \sigma_0^2 - \sigma_n^2) \quad (3)$$

where $\gamma = \sigma_e^2 - \sigma_0^2$. Here σ_e is the equilibrium value (i.e. that reached at the laser saturation) of the energy spread at the perfect tuning and

$$I_n = \int_{-\infty}^{+\infty} I_n(\tau) d\tau$$

is the laser intensity normalized to its equilibrium value (i.e. the saturation value for $\varepsilon=0$); $\Delta T'$ is the revolution period of the electrons in the ring divided by the number of bunches and τ_s is the synchrotron damping time.

Despite the simplicity, results obtained with this model show a remarkable agreement with experiments [8].

3. STABILIZATION

The formulation above allowed us to derive closed expressions for the main statistical parameters of the system - beam energy spread, intensity, centroid position and rms value of the laser distribution - as a function of the detuning. Moreover, the transition between the “cw” and the pulsed regimes has been shown to be a Hopf bifurcation [9].

This opened up the perspective of inducing a “cw” behavior of the laser intensity on the millisecond temporal scale using a

FIGURE 2

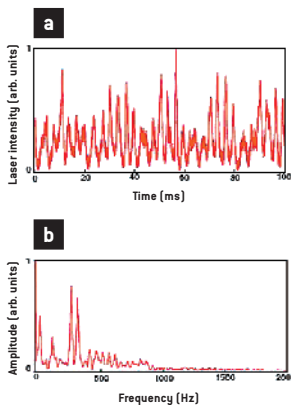
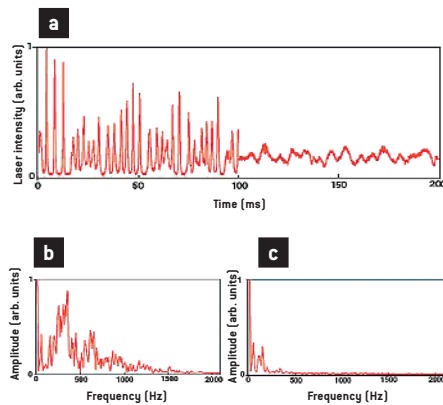


FIGURE 3



closed-loop derivative feedback [10]. The experimental procedure is as follows. A signal proportional to the FEL output power produced, for instance, by a photodiode is sent to the stabilization system, which is made of a simple device to obtain the signal derivative followed by an inverting amplifier with a variable gain. The obtained output is then used to modify the electron beam revolution period by acting on the storage ring radio frequency, which corresponds to varying the value of the detuning ε . From a theoretical point of view, the detuning ε is replaced by the time-dependent quantity

$$\varepsilon_n = \varepsilon_0 + \beta(I_n - I_{n-1}), \quad (4)$$

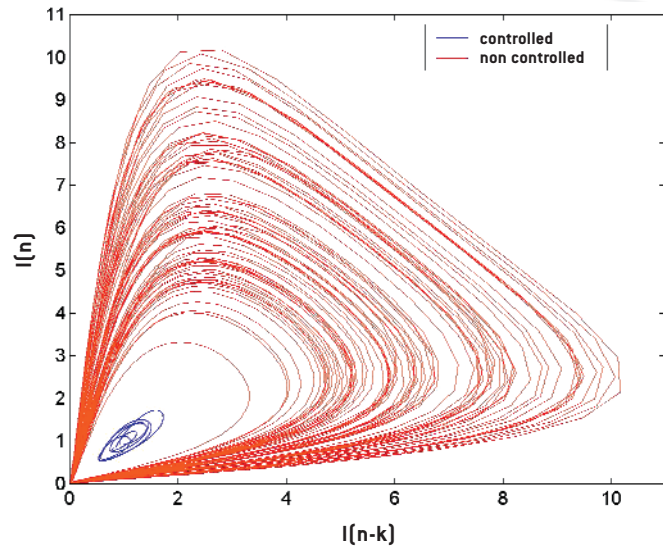
where ε_0 is an offset that can be modulated due the electron beam instabilities, and $\beta \geq 0$ is the loop gain. According to equation (4), the detuning change driven by the derivative feedback tends to counteract any variation of the laser intensity. When the intensity grows (i.e. $I_n < I_{n-1}$), the system responds by increasing the detuning. This pushes the laser pulse towards the tail of the electron beam distribution causing the gain and therefore the intensity to decrease. Vice versa, when $I_n > I_{n-1}$, the detuning is reduced, the gain becomes larger and the intensity tends to grow. Hence the feedback acts against any modulation of the laser intensity, regardless of its intrinsic dynamical origin.

A feedback of this type has been implemented on the ELETTRA SRFEL [8]. Results, shown in Figure 3, confirm the theoretical predictions: the derivative feedback is able to invert the Hopf bifurcation and, at the same time, to counteract the effect of the time-dependent detuning due to the electron beam instabilities.

An alternative strategy based on a multi-delayed feedback [11] is presently under study. Such a method can be considered as a generalization of the one presented above. In this case the laser-electron detuning is modulated according to

$$\varepsilon_n = A_1(I_n - I_{n-l}) + A_2(I_n - I_{n-m}) \quad (5)$$

where $l, m < n$ and $l \neq m$. Numerical results shown in Figure 4 give evidence of the stabilizing effect obtained with a suitable choice of l and m .



4. CONCLUSION

Starting from a simple theoretical model we proposed different strategies for stabilizing the temporal dynamics of a SRFEL. A closed-loop derivative feedback has been successfully implemented on the ELETTRA SRFEL. A more general method based on a multi-delayed feedback has been numerically simulated and will become operational in the next few months.

References

- [1] N.A. Vinokurov et al., Preprint INP77-59 Novosibirsk (1977)
- [2] M.E. Couprie et al., *Nucl. Instr. and Meth.* **331** (1993) 37
- [3] H. Hama et al, *Nucl. Instr. and Meth.* **375** (1996) 32
- [4] R.P. Walker et al. *Nucl. Instr. and Meth.* **429** (1999) 179
- [5] B. Diviacco et al. *Proceedings EPAC 2000*, 2322
- [6] A. Gatto et al., *Nucl. Instr. and Meth. A* **483** (2002) 357.
- [7] M. Billardon et al., *Phys. Rev. Lett.* **69** (1992) 2368
- [8] G. De Ninno et al., *Phys. Rev. E*, (2005) 3276
- [9] G. De Ninno and D. Fanelli, *Phys. Rev. Lett.* **92** (2004) 094801
- [10] S. Bielawski et al., *Phys. Rev. A* **47**, (1993) 3276
- [11] A. Ahlborn and U. Parlitz et al., *Phys. Rev. E* **93** (2004) 264101

Figure 4. Phase space attractor of the dynamics of the laser without (**red**) and with (**blue**) the delayed control signal. The attractor is reconstructed by an embedding technique plotting the FEL intensity at passage n as a function of the FEL intensity at a time $n-k$, where $k (<n)$ is a suitable integer number.



INSTRUMENTATION
& TECHNOLOGY

A NEW DEVICE FOR BIMORPH MIRRORS TECHNOLOGY: THE SY900S/A1902BS BIPOLAR HIGH VOLTAGE POWER SUPPLY SYSTEM

> F. Billè, R. Borghes, G. Cautero, M. Cautero, D. Cocco, L. Iviani, B. Krastanov, R. Pugliese and G. Sostero
Sincrotrone Trieste S.C.p.A., S.S. 14 km 163.5, in AREA Science Park, 34012 Trieste, ITALY

> R. Signorato

Accel Instruments GmbH, Friedrich-Ebert-Straße 1, 51429 Bergisch-Gladbach, GERMANY

An important feature of X-ray mirror substrates is the possibility to continuously vary their curvature (dynamical bending) in order to be able to precisely adjust their optical properties to different beamline geometries, to permit, for instance, the variation of the grazing angle of incidence (to define a proper energy cut off) or to change (or optimize) the focal spot dimensions in the experimental chamber. An innovative device which incorporates the bending mechanism in the mirror substrate itself and effectively combines a very precise adaptive zonal control with an overall extreme simplicity and easiness of use has been developed during the last few years and is currently manufactured by the French company SESO: the Piezoelectric Bimorph Mirror (PBM) [1]. The working principle of a PBM is fairly simple. One can think of it as

a mirror in whose substrate several piezo electrodes are embedded. In reality the mirror body is made of bi-layers of electrically active elements (zirconate lead titanate ceramic), with parallel polarization. An inert reflecting plate (typically fused silica or Silicon) which is then polished, is glued on top of it. When a driving voltage is applied at a particular position of the mirror, one of the piezo plates shrinks while the other one expands. This differential expansion results in a purely spherical bending of the whole device if the same voltage is applied to all control electrodes. The big advantage of this system with respect to a mechanical bender is that it allows not only the possibility to control the overall mirror shape (spherical radius of curvature) but also to compensate the local figure errors of the mirror or the incoming X-ray wave front deformation

Figure 1. Long Trace Profiler set up for the measurement of a bimorph mirror facing down. The mirror with its 32 channel (property of BIO-CAT) is supported on an adjustable holder. The moving pentaprism of the LTP is rotated of 90° to deflect the beam up, towards the mirror surface.



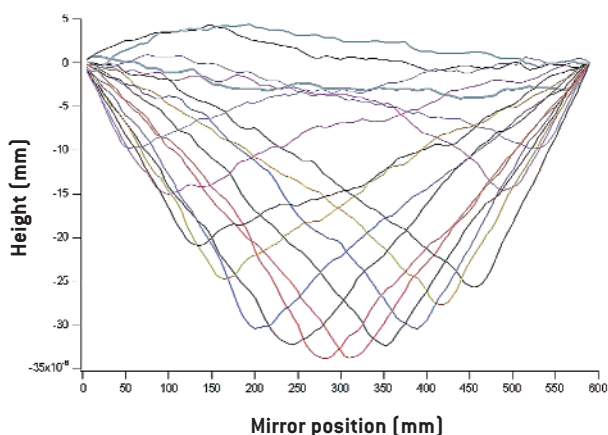


Figure 2. Effect of a +50 V pulse applied sequentially at each electrode. This voltage produces a local bump which propagates along the mirror.

These results are used by the correction tool to estimate the necessary voltage to apply at each electrode to optimize the mirror shape

(typically due to previous mirrors slope errors or thermal bumps). For example, one of the mirrors we have tested (Figure 1) was 600 mm long with 32 electrodes. This means that a local control with spatial cut-off frequency of 18 mm was possible. This mirror is property of the National Institutes of Health-supported Research Center Bio-CAT RR-08630 (at the Advanced Photons Source, Argonne National Lab. IL). Several similar mirrors have been measured recently in the optical metrology laboratory of ELETTRA. This laboratory is equipped with a long trace profiler (LTP, also visible in Figure 1), which is a direct slope measuring device, capable of detecting slope variations of the mirror well below the 1 microradian rms level, which typically correspond to a few nanometers local variation of the profile. The LTP is located in a thermo-stabilized room which completely isolates the instrument from the rest of the metrology laboratory. So it is possible to perform very long measuring sessions, like the one necessary for this kind of mirrors, without losing precision because of uncontrolled temperature drifts. Testing such a kind of mirror is, in fact, a quite long and very challenging task. The first part of the test consists in the characterization of the response of the mirror at a given voltage applied to each single electrode. In Figure 2, it is reported the graph obtained after this test. Each line corresponds to the effect of a +50V pulse applied at a particular electrode

on the mirror. The final goal of this procedure is the creation of a “Correction Matrix” that allows knowing the correct voltages that must be supplied to the piezoelectric bimorph mirrors to achieve the needed shape. The control of the mirror power supplies and the creation of the Correction Matrix is performed through an instrument developed exactly for this purpose at ELETTRA: the High Voltage Bipolar Power Supply System.

This system consists of a power supplies module (A1902BS), that will be described later, controlled by an Intel SBC board (SY900s controller) that is accessible via Ethernet through any common web browser (see Figure 3) or using a LabVIEW client or some of the most popular synchrotron

Figure 3. One of the web pages that allows the control of the power supply system through traditional web browser (GUI)

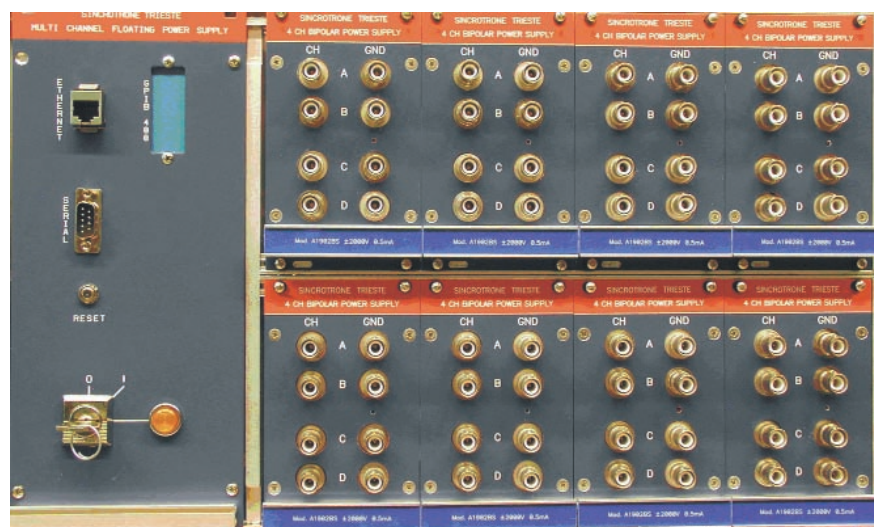


facility control systems (i.e.: Epics, Tango). It is based on XCS architecture, the core of the ELETTRA Beamline Control System, and appears like a Network Attached Device (NAD), so that it can be easily interfaced to any computer through a Local Area Network. When it works for characterizing the response of the mirrors, it elaborates the line profile data that receives as a result of the voltages supplied to each piezoelectric electrode and from these data, a set of matrices “voltage – position – profile”, it produces the required correction matrix. Once this characterization is performed, one can, in principle, obtain any mirror profile (within the given dynamical bending limits) reducing all the shape errors with spatial frequency larger than the electrode spacing.

A very important factor is that, to change from one radius of curvature to another, the applied voltage can change of as much several hundred volts, (from -600 to +600 or even more) but the necessary precision to correct even small local defects is still of the order of some tens of meV and these voltages have to be maintained in an extremely stable way on a very long time scale (weeks or even months). For this reason, the performance and the general behaviour of the mirror is strongly dependent on the power supply used to drive the embedded piezo systems.

In order to meet these very demanding requirements a new family of bipolar power supplies (A1902BS) has been developed at ELETTRA in collaboration with the Italian company C.A.E.N. S.p.A. These power supplies are connected to the previously described PC embedded (“SY900s controller”) by means of a standard CAN bus (see picture 4), following the well tested SY900 architecture of the previously developed A90XS modules. Each module, encased in a standard 3U high-15TE wide aluminium box, hosts four fully independent bipolar supplies and presents four pairs of SHV output voltage connectors (the live terminals and the relative grounds). The voltage swing that each channel can stand is 4000V, from -2000V to +2000V continuous range (zero crossing). The maximum drain and source capabilities are equal and up to 500uA per channel and each channel has its own calibration settings stored in an onboard Eeprom memory. Voltage monitoring is achieved by sensing the real output after a high stability, high voltage divider and feeding it to a multiplexer, which puts it through to a true 16-bit analogue to digital converter. The 16-bit output value is then transferred to a micro controller, which sends the information to the user application via Ethernet as previously described. On a 2kV bipolar module the

Figure 4. Photograph of the Bipolar Power Supply System; 32 A190BS bipolar power supplies (right side) and SY900s controller (left side)



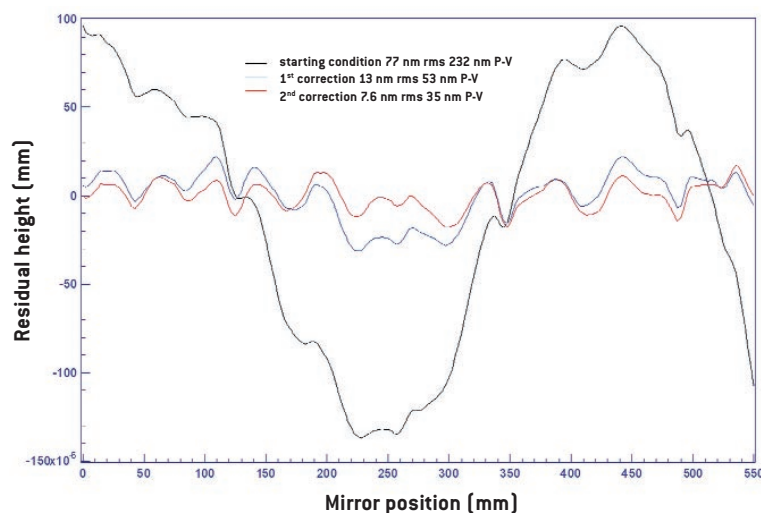


Figure 5. Mirror profile before and after correction. The starting residual error is represented by the black curve. After the first correction a clear improvement is obtained. A further iteration produce a residual error, as in the red curve, with a total error reduction of a factor of 10.

resolution achieved is about 60 mV while the current resolution is about 60 nA.

Noise and residual ripple rms values at the output of these modules are better than 15ppm/FS and, what is most important, the long term stability (1 week observation) of the module is better than 100ppm/FS. This performance, if necessary, can be also improved by thermostating the system, as it was observed that the ambient temperature modifications are the most important factors that affect long term stability.

In Figure 5 an example of mirror shape optimisation is shown. The request was to create an almost perfectly flat mirror, i.e. with a radius of curvature close to ∞ . The first LTP measurement gave a residual shape error of 232 nm peak to valley (P-V) and 77nm rms (black curve). Just after the first iteration, i.e. adopting the voltages given by the correction tool, the shape errors went down to 52 nm P-V and 13 nm rms (blue curve) with an effective error reduction of a factor 6. A second iteration produced a residual error of just 35 nm P-V and 7.6 rms (red curve) equivalent to a factor 10 in the error reduction.

The High Voltage power supply also includes an algorithm that allows, through individual calibration of each mirror, to minimize the effect of creep and hysteresis of the piezo actuators, leading to extremely

high level of repeatability and absolute accuracy in the shaping of the mirror.

CONCLUSION

We presented a new high voltage power supply setup developed and customized to control the Piezoelectric Bimorph Mirrors system manufactured by SESO[1]. It allows to continuously vary the mirrors curvature (dynamical bending) controlling the voltage applied to the piezoelectric elements that constitute the mirrors substrate. The architecture and the most important features of the system, 1) precision and long term stability, 2) Ethernet accessibility through the most popular communication protocols and 3) the automation of the calibration procedure have been depicted. Finally, the results obtained applying the correction procedure to one of the mirrors measured in the optical metrology laboratory of ELETTRA have been shown.

References

- [1] Signorato R., Hignette O., Goulon J., *J. Synchrotron Rad.* (1998). 5, 797-800

THE ELETTRA VIRTUAL COLLABORATORY: THE EVOLUTION OF A VIRTUAL LABORATORY SOFTWARE

> F. Asnicar, F. Billè, R. Borghes, A. Busato, V. Chenda, A. Curri, L. Del Caño, D. Favretto, L. Iviani, E. Mariotti, R. Pugliese, M. Turcinovich
Sincrotrone Trieste S.C.p.A., S.S. 14 km 163.5, in AREA Science Park, 34012 Trieste, ITALY

Science is a collaborative activity and the traditional environment for scientific collaboration is the laboratory, where collaborations still rely heavily on face-to-face interactions, group meetings, individual action, and hands-on experimentation. Electronic collaborative environments that support scientific activities, or laboratories (a term coined by William Wulf [1]) aim at giving scientists all over the world the opportunity of remotely controlling and operating instrumentation, accessing datasets, and easily interacting with colleagues. In particular, the core capabilities that constitute a laboratory can be seen as technologies to link:

- People to people (e.g., familiar applications, such as electronic mail, and tools for

data conferencing), to make remote scientists more visible to one another, and therefore, allow them to recognize common interests and concerns that can form the basis for future collaborations.

- People to information (e.g., the World Wide Web and digital libraries), to provide faster and less-restricted availability of data and results.

- People to facilities (e.g., data viewers that display the current modes and status of remote instruments as well as services that provide scientifically critical data), to enhance utilization of scarce scientific resources, by expanding access to these resources.

The ELETTRA Virtual Collaboratory (EVC) is an example of a virtual laboratory, a system which allows a team of researchers

Figure 1. Remote Operations@ELETTRA.



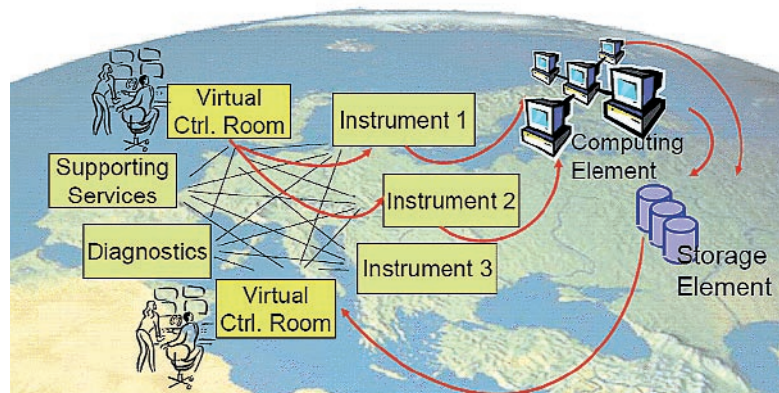


Figure 2. Virtual Control Rooms.

distributed anywhere in the world to perform a complete experiment on the beamlines and experimental stations of ELETTRA [2]. The creation and introduction of effective Computer Supported Collaborative Work (CSCW) systems aims at bringing the following main advantages: provide remote access to expensive and hard-to-duplicate equipment; increase the effectiveness of the experimental activity, since more experts can participate to experiments, give useful hints and solve problems; facilitate multi-institutional consortia collaborations on large-scale projects.

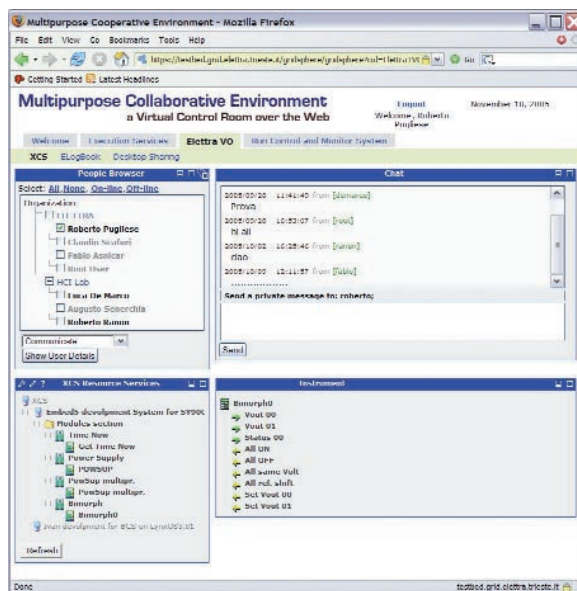
Experience and know-how acquired during the development of EVC is being exploited in the FP6 EU funded projects in which ELETTRA is currently involved. In the BIOXHIT project, which will develop an integrated platform for high-throughput structure determination, ELETTRA is developing the Virtual Collaboratory System (VCS), a Virtual Organization (VO) connecting all the European laboratories doing research in the field of structural genomics. In the EUROTeV project, the design study of the International Linear Collider, ELETTRA is developing the Multipurpose Virtual Laboratory (MVL), the core tool to implement the Global Accelerator Network, a VO connecting all the international laboratories doing research in the field of Accelerators. Remote control of an accelerator facility has the potential of

revolutionizing the mode of operation and the degree of exploitation of large experimental physics facilities.

VCS and MVL have in common the requirement to support integration of «fabric» resources located in different institutions and inside completely separated and geographically dispersed networks. This means that it is not acceptable any more to use ad-hoc solutions, which generally do not take seriously into account security aspects, but in turn results in an overall improvement of the system.

The MVL prototype was tested during a remote operation session and a remote measurement session in June 2005. These events have been also reported in the website www.lightsources.org as shown in Figure 1. The MVL prototype seems architecturally suitable to support far remote operations, maintenance of the accelerator and its trouble-shooting, the repair of delicate equipment and to perform collaborative machine physics measurements with other laboratories. The prototype architecture seems also suitable to implement the «Global Accelerator Network» and to act as glue between the teams doing research in the field of accelerators. In this architecture, every institute in the GAN should have a MVL Node. The node can support more stations (e.g. a control room station, a mobile or semi mobile station etc). Stations can share resources and tools.

Figure 3. MCE Portal Virtual Organization Workspace.



Experience and know-how acquired during the development of EVC will also be used in the GRIDCC project [3], which will extend the use of Grid computing to include access to and control of distributed instrumentation. Access to the instruments will be via an interface to a Virtual Instrument Grid Service (VIGS). VIGS is a new concept and its design and implementation together with middleware that can provide the appropriate quality of service is a key part of the GRIDCC development plan. Recent developments in Grid technologies have concentrated on providing batch access to distributed computational and storage resources. GRIDCC is extending this to include access to and control of distributed instruments. Instruments work in real-time and their successful operation often requires rapid interaction with conventional computing/storage resources and/or other instruments. The control of instruments is often an interactive process. The real-time and interactive nature of instrument control provides a critical requirement for the definition of acceptable Quality of Service (QoS) constraints for interactions between the different Grid components.

GRIDCC is developing these definitions, where appropriate, building on work that is being carried out in the various standards organizations. In order to meet these defined QoS constraints it is often necessary to provide mechanisms for reserving the instruments, and subsequently the compute and storage elements they will require. GRIDCC will run a representative set of applications in order to validate the software produced by the project. The applications are: the High-Energy Physics experiment CMS [4], the particle accelerator ELETTRA, monitoring of distributed electrical power generators [5] meteorology, analysis of neurophysiologic data for migraine detection, and a geophysical monitoring network. These applications will control and monitor different types of instrument, acquire data from these instruments and then analyze this data on existing Grid test-beds. This will demonstrate integration of this project with existing European wide Grid projects.

The Multipurpose Cooperative Environment (MCE) is a groupware which provides general-purpose services to control remote instrumentation, manage experimental activity and allows the implantation of

the different testbed applications through customization and integration with application specific services. The system will be used to implement the VCR for the different applications of the GRIDCC project.

The MCE will be based on a core groupware application, which solves common problems (e.g., authentication, management of the users and instrument resources, management of the Virtual Organizations, monitor of the instrument status, job control, etc) and a set of plug-ins, part of which will be general (e.g., chat, file browser, notebook, video conference), and others specific to the particular application (e.g., accelerator control, instrument control).

The MCE will be a uniform and unique environment providing support for general distance collaboration and, at the same time, access to remote control and monitoring of scientific instrumentation in the context of experimental activities. The general groupware functionalities of the MCE will be extended to support different virtual instruments coming from specific pilot applications of the GRIDCC project.

Figure 2 describes how the MCE instantiated in a specific control room integrates with the other components of the GRIDCC project while Figure 3 shows a screenshot of the early prototypes of the MCE.

References

- [1] R.T. Kouzes, J.D. Myers, and A.D. Wulf, «Collaboratories: Doing Science on the Internet», *IEEE Computers*, Volume 29, Number 8 (1996)
- [2] R. Ranon, L. Chittaro, R. Pugliese, «The ELETTRA Virtual Collaboratory: a CSCW System for Scientific Experiments with Ultra-Bright Light Sources», Proceedings of HCITALY 2003, Symposium on Human-Computer Interaction, Torino (2003)
- [3] <http://www.gridcc.org>
- [4] http://cmsdoc.cern.ch/cms/TRIDAS/Temp/CMS_DAQ_TDR.pdf
- [5] M. Irving, G. Taylor, P. Hobson, *IEEE Power & Energy Magazine* March/April 2004

NOVEL INSTRUMENT FOR SYNCHROTRON LIGHT APPLICATION

> E. Busetto, G. Bortoletto, I. Cudin, and S. Grulja

Sincrotrone Trieste S.C.p.A., S.S. 14 km 163.5, in AREA Science Park, 34012 Trieste, ITALY

The second version of the double crystal monochromator prototype, shown in Figure 1a and 1b, has been tested by using the autocollimator and X-ray beam at the 11.2 front-end at ELETTRA.

With this new design we want to simplify the internal mechanics as much as possible without losing the general performance requested for the instrument. Three independent stepping motors have been used, one for the first crystal rotation and other two for the rotation and translation of the second one. A five reflection set-up has been adopted to measure the parallelism error in the vertical and horizontal plane by using a precise autocollimator.

The residual pitch and the roll errors in parallelism between the two crystals, along the complete angular scan, have been evaluated and identified.

A feedback system based on the current of

an ion chamber has been integrated to correct the angular position of the second dispersive element and maximise the total flux.

In Figure 2 a summary of the results has been depicted.

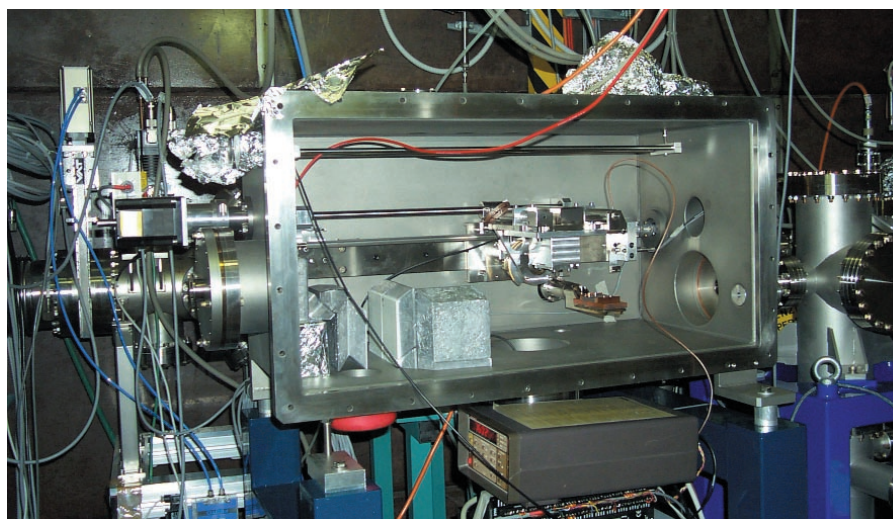
The red curve represents the parallelism error in arcsec of the couple of crystals during the energy scan. This error is due to the residual eccentricity in the second goniometer coupling.

The yellow curve represents the piezo-translator correction induced by the feedback system in arcsec.

The blue curve is the ion chamber current in Ampere. Each point of the curve represents the maximum value of the flux at the given energy.

The monochromator internal movement has been patented and completely redesigned. The final version should be tested along the first half of the 2006.

Figure 1. (a) The double crystal monochromator prototype.



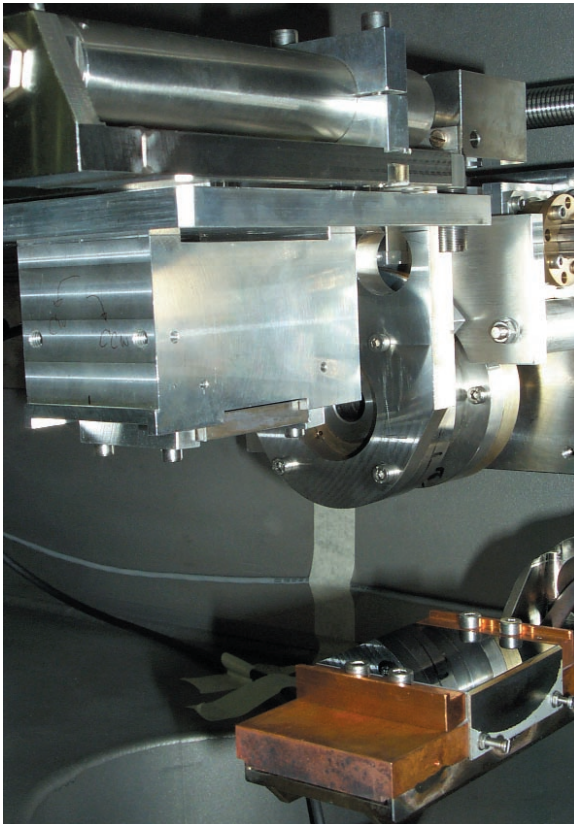


Figure 1. (b) Particular of the mechanical mounting of the double crystal monochromator prototype.

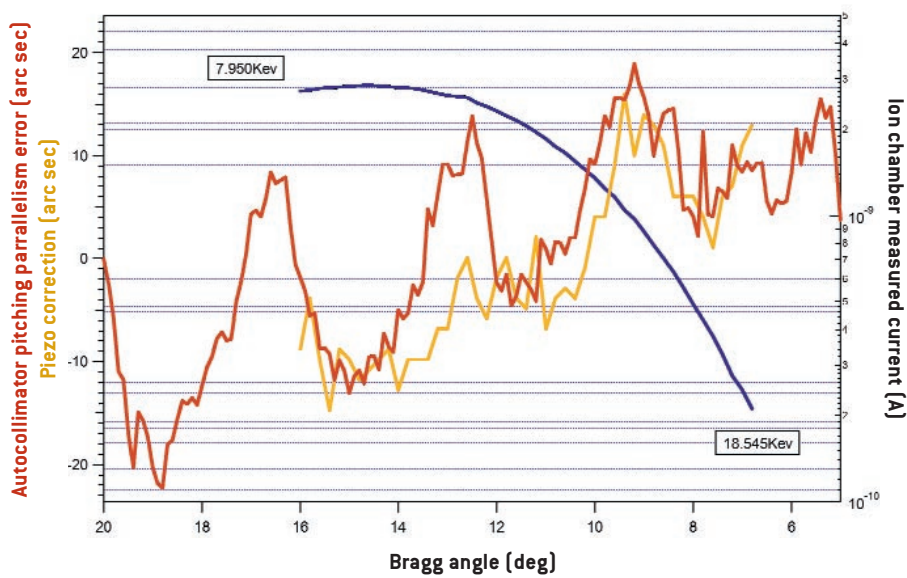


Figure 2. Optical and X-ray tests the red curve represents the parallelism error of the couple of crystals during the energy scan. The yellow curve represents the piezotranslator correction induced by the feedback system in arcsec. The blue curve is the ion chamber current in Ampere. Each point of the curve represents the maximum value of the flux at the given energy.

SCIENCE WITH FERMI@ELETTRA: AN EUV SOFT X-RAY FREE ELECTRON LASER

> **F. Parmigiani**

*Sincrotrone Trieste S.C.p.A., S.S. 14 km 163.5, in AREA Science Park, 34012 Trieste, ITALY
Università degli Studi di Trieste, Via A. Valerio 4, 34127 Trieste, ITALY*

> **C.J. Bocchetta**

Sincrotrone Trieste S.C.p.A., S.S. 14 km 163.5, in AREA Science Park, 34012 Trieste, ITALY

This paper presents the status of the Free Electron Laser at ELETTRA (FERMI@ELETTRA) and a brief description of the first two beamlines so far selected for funding.

The project represents the first user facility in the EUV and soft X-ray range based on seeded harmonic cascade FELs, providing controlled, high peak-power pulses. Beginning with a high-brightness photocathode gun, and using the existing 1.2 GeV LINAC upgraded to FEL use, the facility is designed to provide a tunable output, over a range from ~ 100 nm to ~ 10 nm, a pulse duration from ~ 40 fs to ~ 1 ps, a peak power of ~ 1 GW and fully variable output polarization (linear vertical/horizontal and circular left/right). Initially, two FEL cascades are planned. The first FEL is based on a single-stage harmonic generation scheme to produce wavelengths longer than 40 nm, while the second FEL is a two-stage cascade operating over the range ~ 40 nm to ~ 10 nm. The photon pulse is expected to be transform limited with a peak power in the GW range. In the present scheme, conventional lasers are used extensively, in particular to modulate the electron beam, to drive the photocathode and as a second photon source on the beamlines, for pump-probe experiments. For this reason, laser systems are an integral and fundamental part of the accelerator infrastructure, and the optical timing system will synchronize RF signals, lasers, X-ray pulses and beamline lasers (e.g. for pump-probe experiments). Most of the future scientific activities will be devoted to the structural and spectroscopic studies of low-density matter, inelastic scattering and inelastic resonant EUV and soft X-ray scattering, non-linear

optics, physics of mass selected clusters and bio-molecules, EUV-lithography and the design of an attosecond facility as a branch-line of the FELs. This year has seen intensive studies performed for the optimization of the technical parameters of the facility. Close interaction between the user community and machine designers has been essential and has determined many of the machine characteristics and challenges. The technical optimization study will conclude in the early part of 2006 and will be followed by extensive engineering and construction.

OVERVIEW OF THE FACILITY

The FERMI@ELETTRA facility will make use of the existing GeV LINAC of ELETTRA, which will become available for dedicated FEL applications following the completion of construction of a new injector booster. The present thermoionic source will be replaced by a new RF photocathode injector, and some additional accelerating sections will be added, so that this LINAC will be capable of providing high brightness bunches at 1.2 GeV with up to 50 Hz repetition rate.

The planned facility will see a backward extension of the linac and klystron gallery, the construction of an undulator hall and attached to this a new experimental hall (see Figure 1 for a schematic layout). The backward extension of the linac will permit the assembly and testing of the photoinjector and accelerating sections to the first bunch compressor. These tests of critical systems will be done without disrupting normal refill operations for ELETTRA. Adjacent to the linac tunnel extension a large laser hall

will also be constructed for the photoinjector, laser heater and diagnostics.

The gun is based on an S-band RF photocathode gun, with spatial and temporal control given by the photocathode laser system, and will provide high brightness electron bunches. The system's design will incorporate a degree of flexibility in the bunch parameters.

Accelerating sections will increase the beam energy to ~100 MeV at the exit of the injector, after which a laser heater system will provide control of the uncorrelated energy spread and possible micro-bunching instability. The laser heater will also be useful for implementing diagnostics systems. Two magnetic bunch compressors are planned, at 230 MeV and at 650 MeV. The final energy of the beam, 1.2 GeV, is determined by the maximum gradient of the accelerating sections, the available RF power (with provision for overhead and de-rating for reliable operation) and off-crest operation for control of energy chirp.

The entire LINAC is installed in a tunnel about 5 m below ground level. In the undulator hall, the electron beam will be directed to the longer-wavelength FEL (FEL-I, $\lambda > 40$ nm), by a horizontally deflecting transport system, or directly to the short-wavelength FEL (FEL-II, $10 < \lambda < 40$ nm).

A timing system based on transmission of optical signals over a highly stabilized fiber optic system will distribute timing signals throughout the facility. This provides synchronization of the photocathode laser to the RF gun phase, stabilized drive signals to RF systems in the facility, and synchronization of the FEL seed laser with the arrival time of the electron beam. A major area of research on the FERMI beamlines will be pump-probe experiments and the optical timing signal provided is fundamental for this.

The seeded FEL process occurs in one stage of harmonic generation for FEL-I and in a two-stage cascade for FEL-II. In the former, the optical seeding pulse bunches the electrons before they enter the radiator (final undulator) after which they radiate. In the second scheme, the electron bunches emit radiation that is used to bunch electrons with a shorter separation and thus emit radiation with even shorter wavelength. For FEL-II, both a fresh-bunch approach and a whole-bunch seeding technique are being developed. The X-ray pulse duration is determined by the seed laser and both short-pulse (~40-100 fs) and long pulse (~0.5-1.0 ps) schemes are under development.

The photon beams from the FELs are transported via beamlines to hutches in the experimental hall. The electron beams are

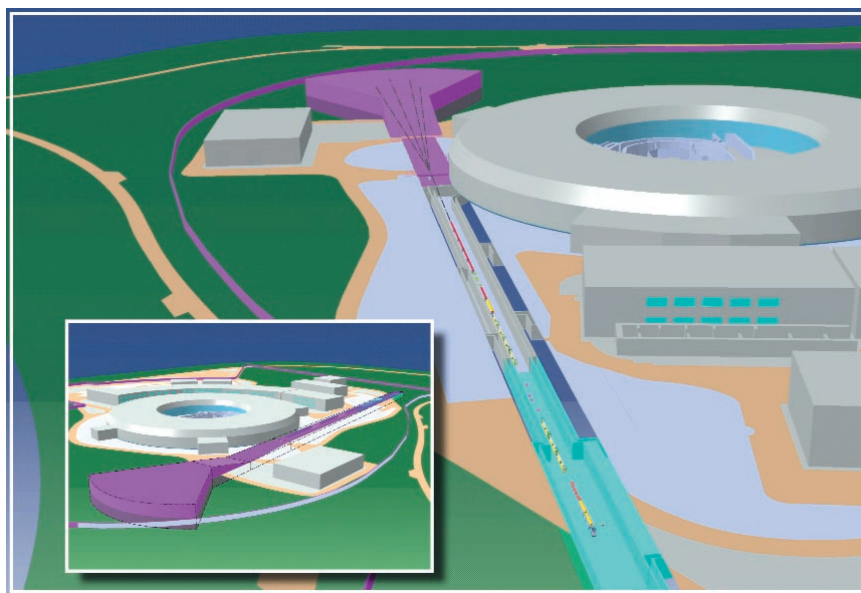


Figure 1. Layout of the FERMI FEL facility

dumped following the final radiating undulator. Laser systems in the experimental area are synchronized to the FEL output using the stabilized optical timing system distributed around the facility. Table 1 and Table 2 give the main parameters of the light pulses.

STATUS OF BEAMLINE PROPOSALS

In an intensive workshop held in Trieste, the machine builders and the future experimentalists exchanged views on the directions in which the FEL could and should go. This provided clear indications of the parameters that were most desired by users and at the same time gave a good overview to the users of what was actually possible. The interac-

tion was particularly productive, stimulating both ideas for new experiments and innovative ideas for machine design. After a formal call for proposals, another workshop was held in Trieste in which extended presentations before a prestigious international Review Panel were given. After a selection procedure, the committee recommended that two of the ten proposals presented be selected for funding. These are «Resonant Inelastic X-ray Scattering Instrument for the FERMI Soft X-ray Laser User Facility», presented by David Moncton of MIT, and «Atomic, Molecular and Optical Science beamline» presented by Kevin Prince of ELETTRA. Of course, FERMI will not have only two beamlines: another call for pro-

Table 1. FEL I main parameters

FEL I		
Parameter	Value	Unit
Photon energy range	[100-40] 12-31	[nm] eV
Pulse length	40-500	fs
Bandwidth	transform limited	
Polarization	variable	
Repetition rate	50	Hz
Peak power (*)	2.5	GW
Harmonic peak power	few percent of fundamental	GW
Photons per pulse (*)	$\sim 10^{14}$	
Peak brightness (*)	$\sim 10^{31}$ [at 31 eV]	ph/s/mm ² /mrad ² /0.1%bw
Pulse-to-pulse stability	work towards 10-15 %	
Pointing stability	< 20	μ rad
Spot size (intensity)	280	μ m
Divergence (intensity)	50 [at 31 eV]	μ rad

(*) 200 fs pulse length

Table 2. FEL II main parameters

FEL II		
Parameter	Value	Unit
Photon energy range	[40-10] 31-124	[nm] eV
Pulse length	40-1000	fs
Bandwidth	transform limited	
Polarization	variable	
Repetition rate	50	Hz
Peak power (*)	1.5	GW
Harmonic peak power	few percent of fundamental	GW
Photons per pulse (*)	$\sim 7.5 \cdot 10^{12}$	
Peak brightness (*)	$\sim 5 \cdot 10^{31}$ [at 124 eV]	ph/s/mm ² /mrad ² /0.1%bw
Pulse-to-pulse stability	work towards 15-20 %	
Pointing stability	< 20	μ rad
Spot size (intensity)	210	μ m
Divergence (intensity)	15 [at 124 eV]	μ rad

(*) 100 fs pulse length

posals will be open in 2005, and there will be others in future.

RESONANT INELASTIC X-RAY SCATTERING INSTRUMENT FOR THE FERMI SOFT X-RAY LASER USER FACILITY

– Coordinated by David Moncton, MIT (USA)
Inelastic X-ray scattering (IXS) is a «photon in/photon out» technique that probes charge-neutral excitations, like phonons, diffusive modes, orbitons, superconducting gaps, excitons, plasmons, particle-hole creation, and interband transitions [1]. It complements existing techniques like ARPES, INS, EELS and Raman scattering (see Figure 2). Since energy and time domain methods are highly complementary, FERMI presents a major opportunity with transform-limited pulses to access wide and partially overlapping temporal ranges to probe dynamics in a comprehensive way.

Many fields can be studied by TRIXS Science:

- **Correlated solids.** Many highly correlated solids are de-facto insulators, and difficult to study using photoemission. RIXS will allow easy access to information on the elementary excitations in these systems, and indeed some significant results concerning dipole forbidden excitations and Zhang-Rice singlets have already been obtained using existing low transmission spectrometers on systems such as the spin-Peierls insulators CuGeO_3 and NaV_2O_5 .
- **High temperature superconductors.** The need for conducting single crystals is a significant restriction for photoemission studies of high T_c superconductors. RIXS will allow studies of excitations in a variety of environments. Current data exist for oxide and diboride superconductors, and indicates that this will be a fruitful area of study.
- **Magnetic systems.** An obvious application of RIXS will be to samples in external magnetic fields. Although not a trivial experiment, the data obtained will be unique and application to both particulate and thin film systems can be envisaged. In combination with conventional magnetic circular dichroism experiments, the RIXS measurements would provide a comprehensive picture of electronic structure in complex non-crystalline magnetic systems.

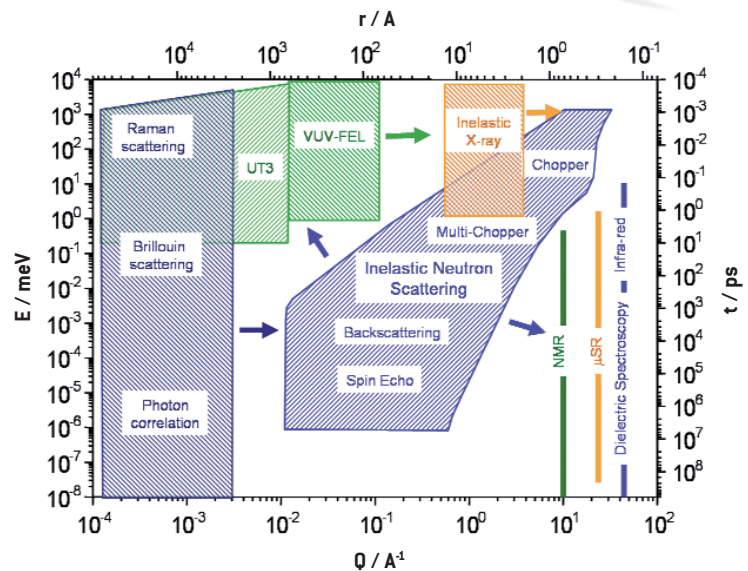


Figure 2. Dynamics in condensed matter

- **Nano-scaled materials.** A recent breakthrough in the use of SXE has been its successful application to liquid phase samples. This has been achieved by the use of ultra-thin vacuum windows that allow soft X-ray transmission, but maintain vacuum integrity. One exciting prospect opened up by this development is the possibility of making RIXS measurements of nano-sized particles in suspension. SXE has been used successfully to study dispersed nano particles in thin film form, but application to suspended particles would be a major step forward.
- **Buried interfaces and wide band gap materials.** SXE has been used extensively to study the electronic structure of wide band gap materials. It is possible that RIXS may allow study of band gap and interface states in such materials.
- **In-situ studies of electrochemical processes.** As with studies of suspended nano-scale particles, the ability to apply RIXS in liquid environments will allow direct study of electrified interfaces in electrochemical systems. This ability to make detailed measurements of electronic excitations with samples simultaneously in a liquid environment and under applied fields is unprecedented.
- **Biological systems.** An obvious extension of the ability to study samples in suspension is the application of RIXS/SXE to systems of biological interest in suspension. This is a vast field, but proof of principle measurements can be made expeditiously.
- **Organic thin film electronic materials.** Finally in this list of possible experiments,

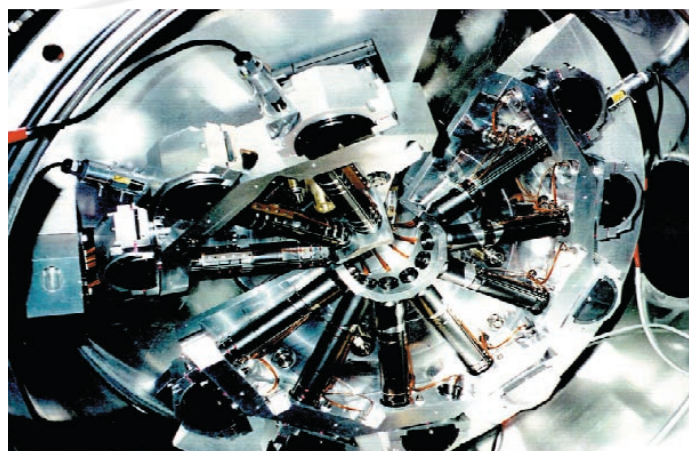


Figure 3. Coincidence spectroscopy apparatus

SXE has been applied recently to a variety of organic thin films grown in-situ. Beam damage is most severe in these systems, but can be minimized by continuous translation of the films during data acquisition. With a high transmission spectrometer, RIXS excitations off of minority elements in these films should be accessible.

ATOMIC, MOLECULAR AND OPTICAL SCIENCE BEAMLIN

– Coordinated by Kevin C. Prince,
Sincrotrone Trieste (Italy)

The proposed beamline will deal with gas phase phenomena, and will allow experimenters to reach a deeper understanding of the interaction between radiation and matter. With this beamline, it will be possible to access a variety of experiments in the field of non-linear optics, in the extreme ultraviolet, where conventional lasers do not reach sufficient peak power levels. For example, doubly photoionization can be studied using the apparatus shown in Figure 3 to perform angle-resolved coincidence spectroscopy. Pump-probe experiments will provide insight into the dynamics of bond breaking, angular momentum sharing, internal energy, and so give a complete description of a chemical reaction. The electronic, structural and chemical properties of highly dilute mesoscopic matter, larger than simple molecules, but smaller than solids, will be investigated. For instance, clusters of metals, oxides, or biomolecules will be studied to understand their structural and electronic properties.

- **Non-linear-optics.** Two-photon absorption allows the probing of states that are forbidden by dipole selection rules in single photon absorption, in particular even states. The doubly excited states of helium are fundamental for our understanding of correlation in this simplest of three-body systems.

In addition helium can be doubly ionized by two photons – only recently has a full understanding been achieved of double ionization of this atom by a single photon. By detecting both electrons in coincidence, it will be possible to study their coherence.

- **Pump-probe.** Using the time structure of Fermi, atoms and molecules can be studied dynamically. Powerful optical lasers will pump the sample to excited states and then the Fermi will probe the electronic structure of these excited molecules. Vice versa, Fermi can pump a molecule to a highly excited electronic state, and the process of fragmentation can be examined with fs resolution by probing with a laser.

- **Nanostructured matter.** Free clusters are a very dilute form of matter and so very difficult to study with third generation light sources. The Milani group within this collaboration has developed a source of clusters, which produces high densities of transition metal clusters with a repetition rate of tens of Hz. This is ideally matched to Fermi, and will allow the characterization of a variety of clusters that are the building blocks for new nanostructured objects.

- **Biomolecules.** The «Flying Proteins» section of this project will produce samples of macromolecules in the gas phase by electrospray techniques, which are again very dilute. However, the high peak power and polarization of Fermi will be sufficient to examine the secondary folding structure of these biomolecules by determining their dichroic properties.

References

- [1] S.M. Butorin et al., *Phys. Rev. Lett.* **77**, 574 (1996)

COORDINATION OF EUROPEAN SCIENCE: THE I3 PROJECT AND THE I3 NETWORK

> M. Bertolo

Sincrotrone Trieste S.C.p.A., S.S. 14 km 163.5, in AREA Science Park, 34012 Trieste, ITALY

ELETTRA is the managing facility of the Integrated Infrastructure Initiative (I3) “Integrating Activity on Synchrotron and Free Electron Laser Science” (IA-SFS), a project supported by the European Community - Research Infrastructure Action under the FP6 “Structuring the European Research Area” Programme (EC contribution: 27 million Euro).

The project started on March 1st, 2004 with the objective of

- supporting transnational users of national facilities in the domain of synchrotron and FEL science
- supporting joint research activities (JRAs) with the purpose of (i) enhancing the effectiveness of the facilities in serving users and in particular transnational users, and (ii) contributing to the development of novel sources in this domain
- complementing the access and research activities by targeted networking activities (support for specialised workshops, meetings and schools and transnational exchanges between facilities and user institutions).

During the first year of the project more than 600 experiments europewide have been supported in the framework of the initiative. A first call for proposals concerning transnational exchanges has been published in autumn 2004; a second call is open at the time of this writing (deadline January 10th, 2006).

A thorough description of the I3 Project IA-SFS and more detailed information about ongoing activities is available on the I3 homepage <http://www.elettra.trieste.it/i3/>

Already in its first year of existence, the I3 Project participated in an initiative aimed at an even higher level of coordination of European science by the launch of the I3



Network, which brings together all existing (18) I3s and 3 Coordination Actions: this initiative encompasses hundreds of large European Research Infrastructures, ranging from telescopes to botanical collections, used by thousands of European scientists.

The I3 Network has five main objectives:

- To exchange good practice in the management and organisation of I3 and CA projects, both ongoing through FP6 and providing feedback to the Commission relating to FP7.

- To exchange information and expertise in areas of common interest, e.g. approaches to Science and Society activities.

- To act as a central information service regarding the role and importance of major research infrastructures in general and to develop common approaches/solutions to common problems.

- To explore possible synergies between I3, including the possibility of joint research activities.

- To act as a central contact point for information concerning the development of a European infrastructures roadmap, through specific links to the European Strategic Forum on Research Infrastructures (ESFRI) and its working groups.

More information about the I3 Network can be found at <http://i3.neutron-eu.net/>

> Stefano Fabris and Stefano Baroni

CNR-INFM DEMOCRITOS National Simulation Center and Scuola Internazionale Superiore di Studi Avanzati,
Via Beirut 2-4, 34014 Trieste, ITALY

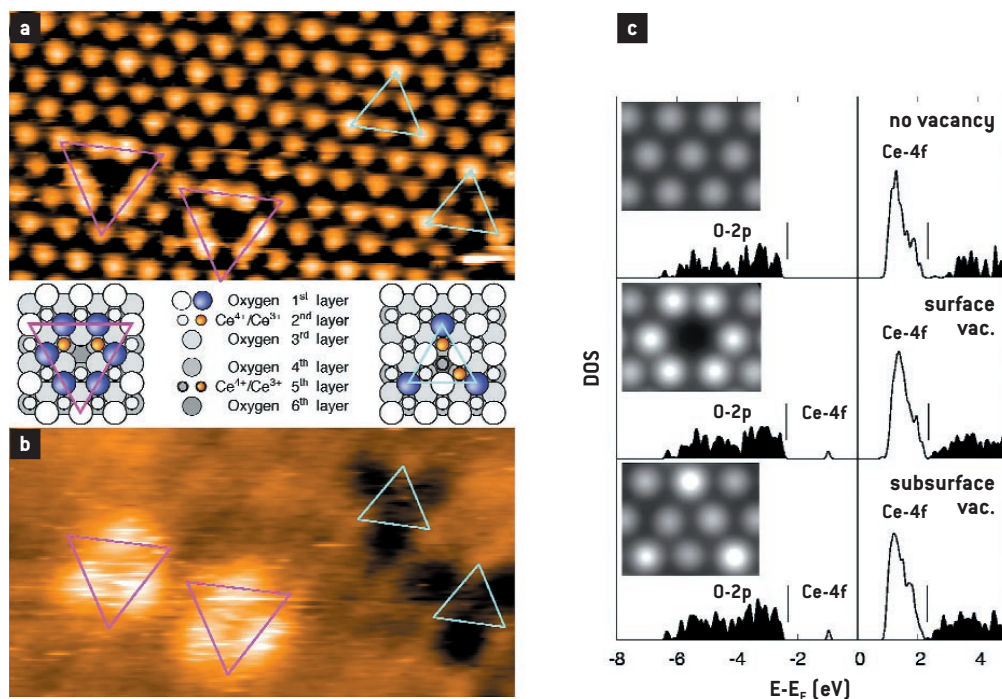
Theory@ELETTRA is a joint project of the *ELETTRA* Synchrotron Radiation Laboratory and the CNR-INFM *DEMOCRITOS* National Simulation Center, aimed at fostering the interaction between the theoretical and experimental scientific communities in Trieste, active in the field of the physics and chemistry of materials, and based in the Miramare and Basovizza areas, respectively. This project builds onto a tradition of successful collaborations between the two communities, so far mainly driven by the initiative of individuals, and it is meant to stimulate new collaborations, as well as to provide a more firm ground for the existing ones. *ELETTRA* is supporting this initiative with the allocation of office space and network infrastructure, while the scientific personnel is at present entirely provided by *DEMOCRITOS*: some of its researchers have moved to the laboratory's premises, and a plan to hire new junior scientific personnel is presently under way. It is hoped that these will be the first steps towards the establishment of a top-class theory group at *ELETTRA*.

A kick-off meeting, jointly organized by *DEMOCRITOS*, *ELETTRA*, and the CNR-INFM *TASC* laboratory, was held on the 5th and 6th of July 2005 (http://www.democritos.it/events/theory_at_elettra.php). As a follow-up of this event, a workshop on the perspectives of theoretical research at *ELETTRA* will be held on December 15 and 16 2005, on the occasion of the XX *ELETTRA* Users' meeting (satellite workshop "Computer Simulation of Surface and Interface Phenomena"). The next section highlights a selection of research lines that have been started following the kick-off meeting.

OVERVIEW OF SELECTED TOPICS IN THE THEORY@ELETTRA PROJECT

Chemical reactivity of oxide surfaces (M. Huang,* S. Fabris, S. de Gironcoli, and S. Baroni, in collaboration with F. Esch, C. Africh, and G. Comelli)

Highly-active catalysts based on precious-metal nano-particles (Au, Pt, Rh, Pd) supported by reducible metal oxides are key-components for abating the emissions from hydrocarbons combustion and are of fundamental importance in the production and purification of hydrogen. The mechanisms responsible for the superior catalytic activity of these devices rely on subtle electronic effects following the creation of oxygen vacancies and on the interaction between the metal nano-particles, the defective surfaces, and the molecular species entering the main chemical reactions to be catalyzed (water-gas shift, steam reforming, CO oxidation). The present project aims at providing a microscopic understanding of these complex highly-active catalysts, mostly based on cerium oxide (CeO₂, ceria). The fundamental processes driving and controlling their catalytic activity depend on the defect chemistry of ceria, which allows for the material to control the oxygen partial pressure at the reaction sites. The most important defects are oxygen vacancies and the compensating Ce³⁺ ions (Figure 1). The first objective of the present project is a clearer characterization of highly reduced ceria structures, including defect clusters and complexes [1]. Secondly, we plan to investigate the molecular adsorption mechanisms on oxide surfaces and the bonding between noble metals and a reducible oxide like CeO₂. This will provide new insight into the charge state of noble-metal adatoms



(which are proposed to be non-metallic when adsorbed on reducible oxides [2]) and will link the change in electronic structure to their high catalytic activity. Finally, the project will shed light on the reaction mechanisms of simple chemical processes occurring on metal nano-particles supported by ceria-based oxides. First-principles density-functional-theory calculations will be the main tool of analysis.

Study of surface charge transfer processes in solar cells

[R. Gebauer, in collaboration with A. Goldoni]

Graetzel solar cells in which a semiconductor surface is sensitized with dye molecules have attracted much attention recently, mostly due their low production costs. A key process in the operation of such photovoltaic devices is the charge injection from the dye molecules at the surface of the semiconductor to the conduction band states within the semiconductor itself. The generally accepted injection mechanism involves photoexcitation to a dye excited state, from which an electron is subsequently trans-

ferred to the semiconductor. Such devices are currently studied at *ELETTRA*, using namely Zn-porphyrin/ C_{70} complexes. The goal of this collaboration is to numerically simulate the charge injection process using time-dependent density-functional theory and to elucidate the connections between the molecular adsorbate, its orientation, and typical charge transfer time scales. Figure 2 shows a surface slab of anatase TiO_2 sensitized with catechol molecules.

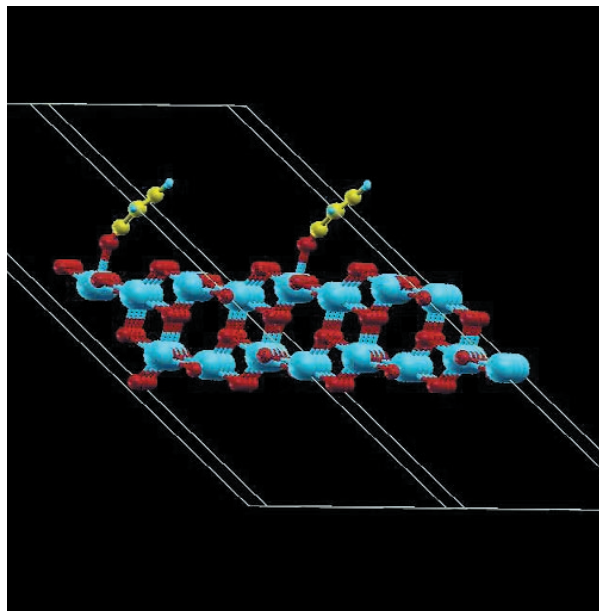
Modeling catalytic reactions on metal surfaces

[X. Ding,* F. Ancilotto, M. Peressi, T. Kokalj,** S. de Gironcoli, A. Dal Corso, D. Alfè, and S. Baroni, in collaboration with E. Vesselli, A. Baraldi, and G. Comelli]

1) The project will be devoted to the study of the catalytic properties of Ni surfaces towards the formation of methanol from carbon monoxide and hydrogen. Copper is one of the most widely used catalysts for this reaction, but recent experiments have pointed out that a Cu/Ni catalyst is 40 times more active. The mechanisms respon-

Figure 1. (a) Filled-state and (b) empty-state STM images of single oxygen vacancies and related structural models (left, surface vacancy; right, subsurface vacancy) on the ceria (111) surface. (c) Calculated density of states [DOS] and simulated filled-state STM images.

Figure 2. Model of a surface slab of anatase TiO_2 sensitized with catechol molecules.



sible for this increased reactivity are still unclear. Moreover, many fundamental aspects of the reaction above need to be clarified, such as the CO_2 configurations on Ni surface. Our long-term goal is the characterization of the stable intermediates of the methanol formation reaction and the identification of a possible reaction path. A combined experimental and theoretical investigation will be essential to shed light on this problem.

2) Within this project we study some elementary steps in important chemical reactions catalyzed on metal surfaces, by means of density-functional-theory calculations. In particular we are investigating the following two topics. *i) Dehydrogenation of methane (CH_4) on transition-metal surfaces.* Tuning the relative reaction rates of the different steps of methane dehydrogenation would allow to optimally design many important reactions such as, *e.g.* the direct conversion of methane to methanol. This work addresses the problem of the dependence of the reaction barriers of the initial stages of methane dehydrogenation on the local atomic structure and chemical composition of the reaction surface sites (Figure 3). *ii) Adsorption of ethylene (C_2H_2) on silver sur-*

faces. The epoxidation of ethylene, catalyzed by silver, is one of the most important selective oxidation processes based on heterogeneous metallic catalysis. This reaction produces ethylene epoxide (oxirane), which is an important intermediate in the fabrication of glycols and polyols. The emphasis of this study is on the influence of surface defects on the energies of the reactants and products, as well as of the transition states.

Metal diffusion on nanotube surfaces

[H. Ustunel,* S. Fabris, S. de Gironcoli, and S. Baroni, in collaboration with A. V. Barinov and M. Kiskinova]

We will study the diffusion mechanisms of metal atoms on the surface and near-surface region of multi-wall carbon nanotubes (MWCNT). The metal of choice is In, since its electro migration on the surface of MWCNTs has been recently observed with transmission electron microscopy [3]. A clear understanding of the diffusion and adsorption processes is however still lacking. We will study the thermal migration of the metal atoms on the MWCNT surfaces by combining Scanning Photoemission Microscopy and Density Functional Theory calculations.

Theoretical methods for simulating spectroscopy

(D. Toffoli,* P. Decleva, G. Fronzoni, M. Stener, D. Di Tommaso and M. De Francesco in collaboration with M. De Simone and S. Turchini; P. Umari,* B. Walker, R. Gebauer, and S. Baroni)

1] This activity is focused on the theoretical description of electronic spectroscopies, notably core absorption (XAS), valence and core photoemission (PES) spectroscopies in finite systems (molecules and clusters). One research line involves the development of time-dependent density-functional-theory (TDDFT) methods for the description of molecular photoemission, including relativistic effects [4,5,6]. Present studies concern the analysis of $\text{Mg}(\text{C}_5\text{H}_5)_2$ (in collaboration with the *ELETTRA GasPhase* beamline) [7] (Figure 4), C_6F_6 , CF_4 , SiF_4 , SF_6 , and C_{60} . We plan to implement the calculation of non-dipole contributions to photoabsorption and photoemission spectra, and to study deviations of the angular distribution from the pure dipole pattern in large molecules. Other topics will be the study of cir-

cular dichroism in the photoemission spectra of chiral systems and the analysis of the electronic structure of transition-metal compounds. In particular, the theoretical description of the electronic structure of transition metal compounds is very challenging since the proper treatment of correlation effects at the ab-initio level requires highly sophisticated theoretical approaches. As a result, many problems are still treated at a semiempirical level. We plan to employ highly correlated ab-initio techniques for the bound states, to compute ionization energies and transition amplitudes (also in open shell systems) accounting for multiplet effects and satellite states. At the same time the photoemission dynamics will be treated at the DFT and TDDFT level. We plan to study the TiCl_4 , VOCl_3 , CrO_2Cl_2 compounds that have been experimentally studied at *ELETTRA*, both in absorption and photoemission. Moreover, carbonyl compounds and organometallic sandwich systems will also be considered.

2] Simulating excited-state properties and optical spectroscopic processes is still a major

Figure 3. Initial [IS], transition [TS], and final [FS] states of the reaction of methane dehydrogenation catalyzed by a metal adatom on a metal surface.

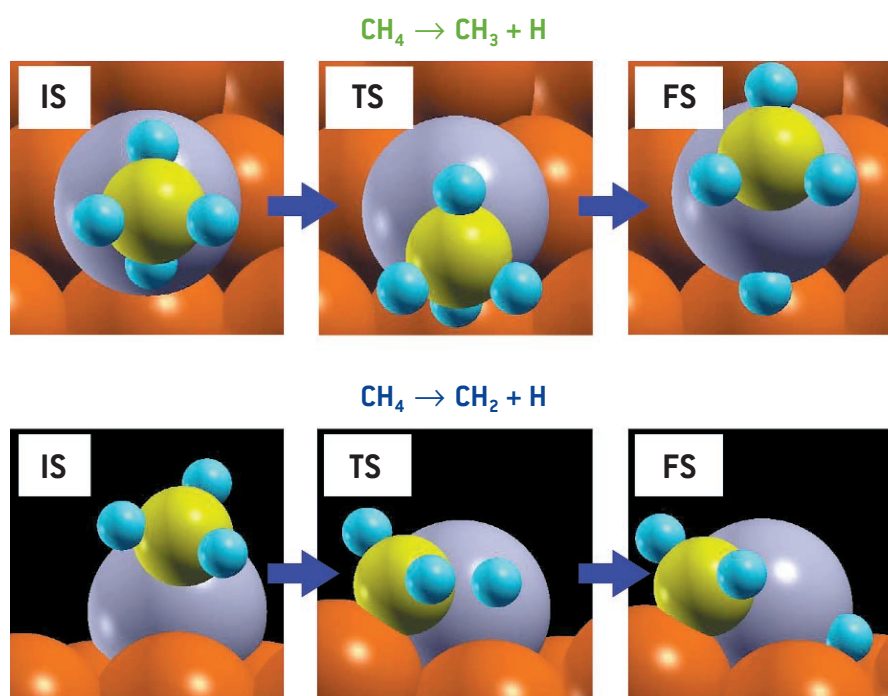
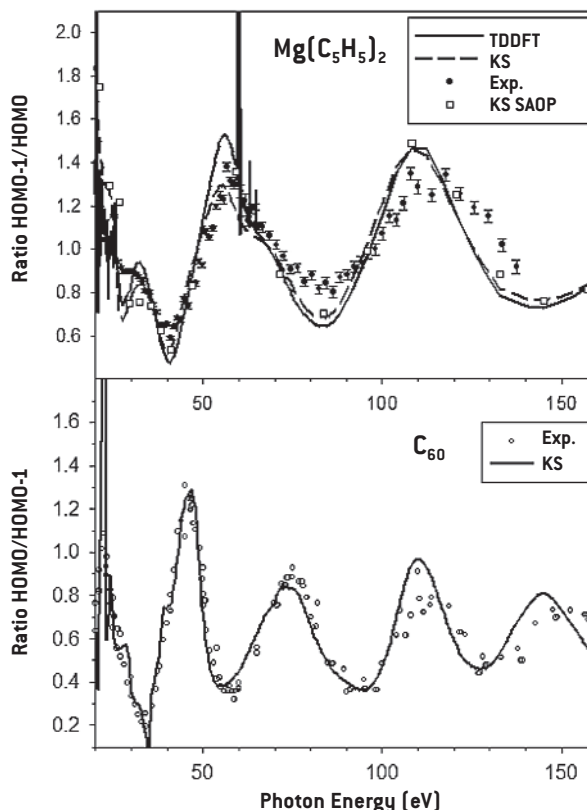


Figure 4. Comparison between the experimental and theoretical HOMO-1/HOMO cross section ratio of $\text{Mg}(\text{C}_5\text{H}_5)_2$ (upper panel) and of C_{60} (lower panel). The calculated values are cluster-assembled film deposited on a

substrate at 100 K) and the theoretical spectrum obtained by means of ab-initio calculations on TBMD-generated configurations. The structures used for the simulations are shown on the right of the insets.



challenge to modern computational physics and chemistry. Traditional quantum-chemistry methods are limited by the small size of the systems they can cope with, and lighter approaches based on TDDFT are becoming popular because of their accuracy and ability to be applied to systems consisting of several tens of atoms. While some of the theory groups active in the Trieste area have a well established expertise in applying these techniques to small molecules in the gas phase (see above), their application to complex molecular systems in the condensed phase will require the development of new theoretical and computational tools. One such new tool has been recently developed [8], based on a super-operator formulation of linearized time-dependent density-functional theory. The new method allows to express the dynamical polarizability of a system of interacting electrons in terms of a matrix continued fraction whose coefficients are obtained from the non-symmetric

block-Lanczos method. The resulting algorithm allows for the calculation of the full spectrum of a system with a computational workload which is only a few times larger than that needed for static polarizabilities within time-independent density-functional perturbation theory, thus opening the way to large-scale excited-state simulations. One of the major projects which will be pursued in the Theory@ELETTRA group concerns the implementation of this new method, its extensive testing, and application to problems and systems of interest at the ELETTRA laboratory.

Theoretical core level spectroscopy

(S. de Gironcoli, in collaboration with L. Bianchettin and A. Baraldi)

A fruitful collaboration has been established with the staff of the ELETTRA superESCA beamline to analyze, with a combined experimental (XPS) and theoretical (ab-initio density functional theory) approach, the effect

of local chemical and geometrical environment on core-level binding energy shifts of surface atoms and adsorbates. In the past, this combined analysis has allowed to provide an independent confirmation of the very large surface thermal expansion of Be(0001) surface [9]; more recently the possibility to identify and monitor the presence of low coordination defects, such as isolated Rh adatom or dimers on a clean Rh (001) surface, has been demonstrated [10]. These studies are being extended to address the local changes in electronic structure induced by molecular species such as nitrogen [11], carbon and sulfur adsorbed on the metallic surface, so that to monitor the molecular species involved in the chemical reactions.

The spin susceptibility of quasi 2D hole gases

[G. Senatore and S. De Palo, in collaboration with L. Sorba and G. Biasiol]

Spin fluctuations are believed to play an important role in the two-dimensional electron gas, near the apparent metal-insulator transition observed at low temperature in clean devices, with lowering the density. In particular, it has been suggested that metallic behavior in 2D should be accompanied by a tendency toward a ferromagnetic instability. Over the last six years several experimental investigation on the spin susceptibility of quasi 2D carriers in solid state devices have been performed. While the results for electron gases are easily reconciled [12] with the available theoretical knowledge on the 2D electron gas model, the results on hole gases are not yet fully understood [13]. We plan to investigate the effects of device details on the spin properties of hole gases, with a joint experimental and theoretical effort, to understand the origin of this apparently different behavior of hole and electron systems in 2D.

References

- [1] F. Esch, S. Fabris, L. Zhou, T. Montini, C. Africh, P. Fornasiero, G. Comelli, R. Rosei, *Science* **309**, 752 (2005)
- [2] Q. Fu, H. Saltsburg, M. Flytzani-Stephanopoulos, *Science* **301**, 935 (2003)
- [3] B.C. Regan, *Nature* **428**, 924 (2004)
- [4] M. Stener and P. Decleva, *J. Chem. Phys.* **112**, 10871 (2000)
- [5] G. Fronzoni, M. Stener and P. Decleva, *Chem. Phys.* **298**, 141-153 (2004)
- [6] D. Toffoli, M. Stener and P. Decleva, *Phys. Rev. A* **66**, 012501 (2002)
- [7] P. Decleva, G. Fronzoni, M. Stener, M. de Simone, M. Coreno, J.C. Green, N. Hazari and O. Plekan, submitted
- [8] B. Walker, A.M. Saitta, R. Gebauer, and S. Baroni, *A new and efficient approach to time-dependent density-functional theory for optical spectroscopy*, submitted for publication
- [9] A. Baraldi, et al., *EPL* **64**, 364 (2003)
- [10] A. Baraldi, et al. unpublished
- [11] L. Bianchettin, et al. in preparation
- [12] S. De Palo, M. Botti, S. Moroni, and G. Senatore, *Phys. Rev. Lett.* **94**, 226405 (2005)
- [13] M. Kumar, G. Mori, F. Capotondi, G. Biasiol, and L. Sorba, *Sol. St. Comm.* **135**, 57 (2005)

* Postdoc

Theory@ELETTRA

** On sabbatical leave
at Theory@ELETTRA



FACTS & FIGURES

ELETTRA BEAMLINE STATUS

(October 2005)

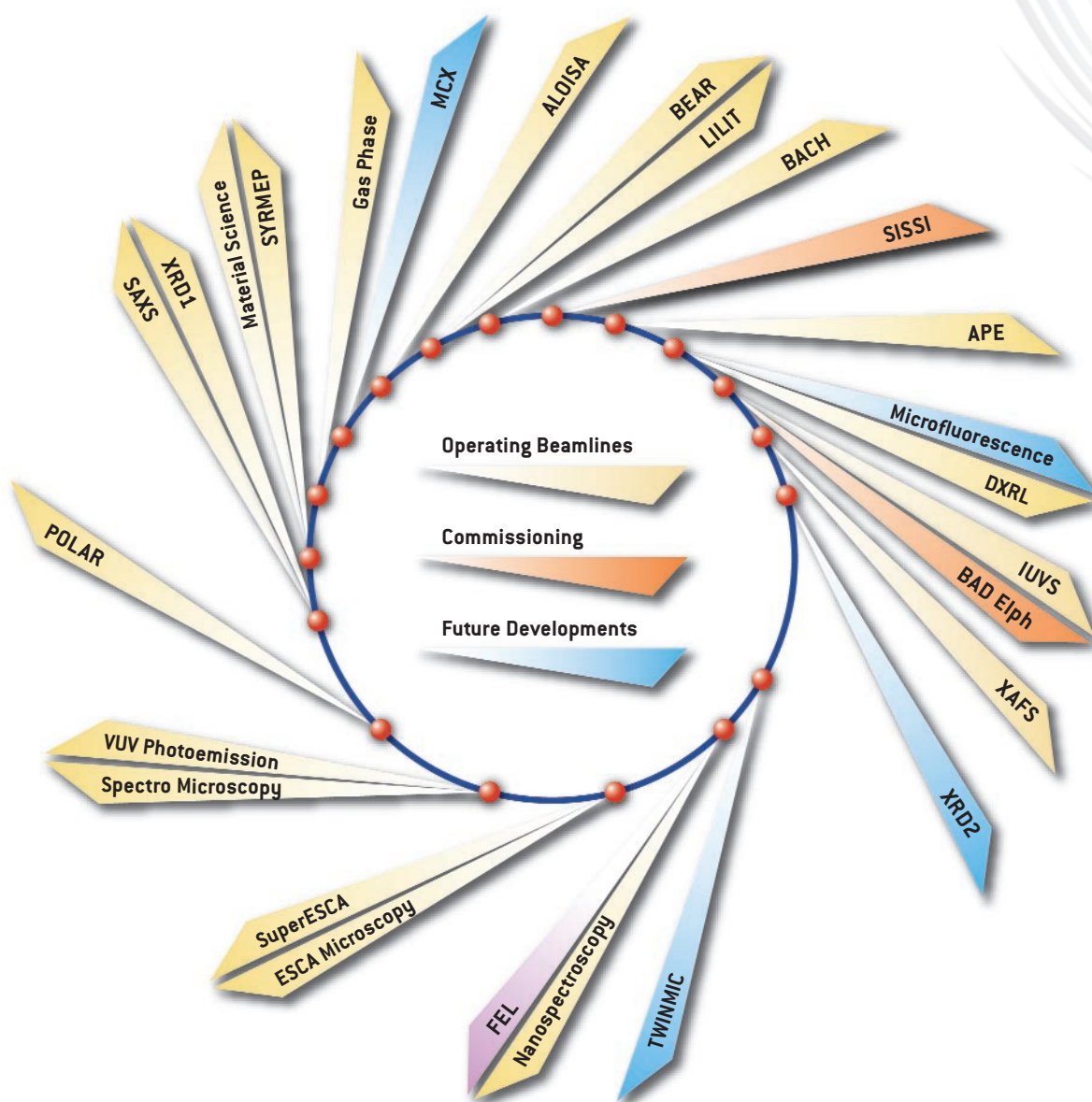
EXIT	BEAMLINE	ACRONYM	PARTNER INSTITUTION
1.1L	TWINMIC		ESRF, PSI, SLS, CNR-INFM, Kings College London, RheinAhrCampus Remagen, Göttingen University, ITPO Ljubljana
1.2L	Nanospectroscopy		
1.2R	Free Electron Laser	FEL	
2.2L	ESCA Microscopy		
2.2R	SuperESCA		
3.2L	Spectromicroscopy		
3.2R	VUV Photoemission		CNR
4.2	Circular Polarized Light	POLAR	CNR
5.2L	Small Angle X-ray Scattering	SAXS	Austrian Academy of Science
5.2R	X-ray Diffraction	XRD1	CNR
6.1L	Materials Science Beamline	MSB	Czech Academy of Science, Charles University, Prague
6.1R	Synchrotron Radiation for MEdical Physics	SYRMEP	University of Trieste
6.2R	Gas Phase		CNR, CNR-INFM, INSTM
7.1	Powder Diffraction Beamline	MCX	University of Trento, INSTM
7.2	Advanced Lights for Overlayer, Interface, and Surface Analysis	ALOISA	CNR-INFM
8.1L	Bending magnet for Emission, Absorption, and Reflectivity	BEAR	CNR-INFM
8.1R	Laboratory for Interdisciplinary LITHography	LILIT	CNR, CNR-INFM
8.2	Beamline for Advanced diCHroism	BACH	CNR-INFM
9.1	Source for Imaging and Spectroscopic Studies in the Infrared	SISSI	CNR-INFM, University of Rome "La Sapienza"
9.2	Advanced Photoelectric effect Experiments	APE	CNR-INFM
10.1L	X-ray Microfluorescence		
10.1R	Deep-etch Lithography	DXRL	
10.2L	Inelastic Ultra Violet Scattering	IUVS	
10.2R	BAD Elph		
11.1	X-ray Absorption Fine Structure	XAFS	ICTP
11.2	X-ray Diffraction	XRD2	

CNR - National Research Council

CNR-INFM - National Institute for the Physics of Matter of the CNR

INSTM - Consortium of Italian Universities for the Science and Technology of Materials

ELETTRA LAYOUT



RESOURCES ALLOCATED AT ELETTRA

PREVISIONALS 2005 - BUDGET ALLOCATIONS (MILLIONS OF EURO)

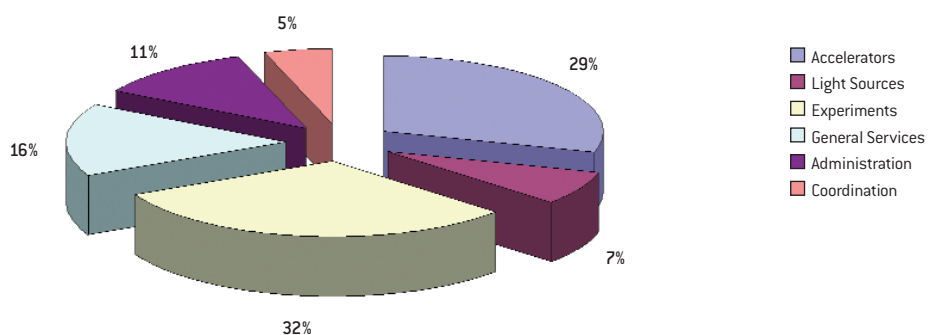
Beamlines, Instruments and In House Research	9.20
Personnel	3.89
Recurrent	0.98
EU Supported Projects	0.90
Special Projects	0.92
Investments (new equipment)	2.51
Accelerators	5.26
Personnel	3.48
Recurrent	1.20
Investments (new equipment)	0.40
Special Projects	0.18
Light Sources	1.58
Personnel	0.90
Recurrent	0.11
Investments (new equipment)	0.05
Special Projects	0.52
Technical Services, Utilitises, Buildings and Administration	14.77
Personnel	3.74
Recurrent	7.01
Taxes, Adm.Costs	2.16
Investments (new equipment)	0.80
Commercial Activities	0.50
Special Projects	0.56
Special Projects of ELETTRA	27.80
Booster	13.30
FERMI@ELETTRA	14.50
Total Budget Allocations	58.61

ELETTRA STAFF

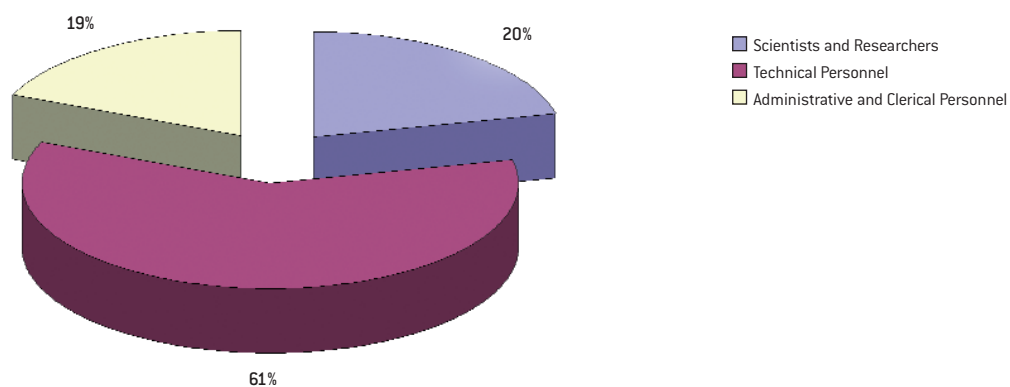
(June 2005)

Sectors	Scientists and Researchers	Technical Personnel	Administrative and Clerical Personnel	TOTAL
Accelerators	11	55	3	69
Light Sources	4	11	2	17
Experiments	31	34	8	73
General Services	0	30	7	37
Administration	0	6	21	27
Coordination	2	6	4	12
TOTAL	48	142	45	235

Staff Distribution per Sector



Staff Distribution per Professional Status

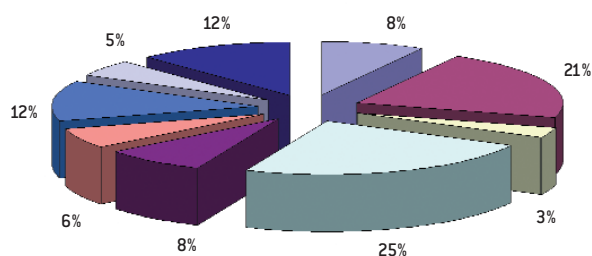


STATISTICS OF PERFORMED MEASUREMENTS

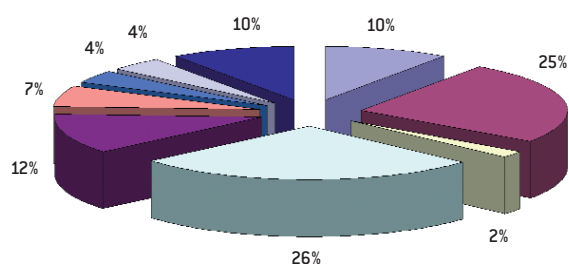
(July 2004 - June 2005)

Research Area	Measurements performed	Shifts used
Atom Molecules and Plasmas	33	577
Catalytic Materials / Surface Sciences	87	1489
Environmental and Earth Science	13	105
Hard Condensed Matter - Electronic and Magnetic Structure	98	1620
Instrumentation and Technological Materials	33	701
Life and Medical Sciences (excluding Crystallography)	25	391
Protein and Macromolecular Crystallography	50	225
Polymers and Soft Matter	20	245
Hard Condensed Matter - Structure	50	577
TOTAL	409	5930

Measurements Performed

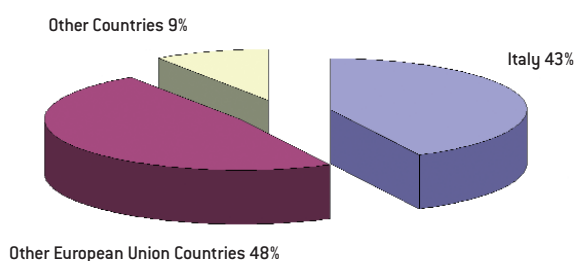


Shifts Used



N. USERS

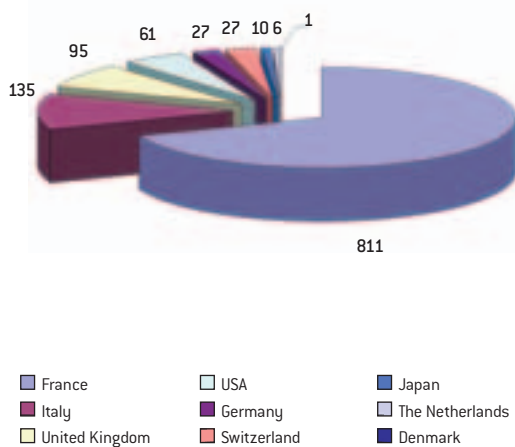
Italy	408
Other European Union Countries	461
Other Countries	90
TOTAL	959



STATISTICS OF THE INDUSTRIAL LIAISON OFFICE

ORDERS 2004 BY CUSTOMER COUNTRY

Country	Number of Orders	Volume (1000 Euro)
France	4	811
Italy	15	135
United Kingdom	4	95
USA	2	61
Germany	4	27
Switzerland	1	27
Japan	1	10
The Netherlands	1	6
Denmark	1	1
Total	33	1,173

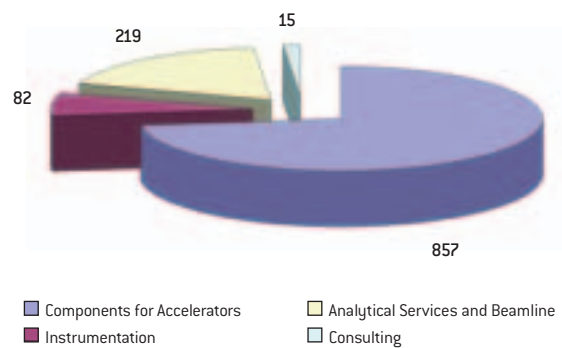


The Industrial Liaison Office team: (from left to right) Claudia Grubissa, Laura Forgiarini, Riccardo Tommasini and Edoardo Busetto.



ORDERS 2004 BY TYPE OF COMMERCIAL ACTIVITY

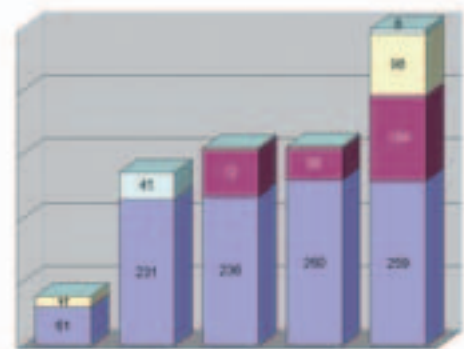
Activity	Number of Orders	Volume (1000 Euro)
Components for Accelerators	6	857
Instrumentation	11	82
Analytical Services and Beamtime	14	219
Consulting	2	15
Total	33	1,173



TREND IN TURNOVER OF COMMERCIAL ACTIVITIES (Thousands of Euro)

Year	2000	2001	2002	2003	2004
Components for Accelerators	61	231	236	260	259
Advanced Scientific Instrumentation	0	0	72	50	134
Analytical Services & Beamtime	17	0	3	3	98
Consulting	0	41	0	0	8
Total	78	272	311	313	499

■ Components for Accelerators ■ Analytical Services & Beamtime
■ Advanced Scientific Instrumentation ■ Consulting



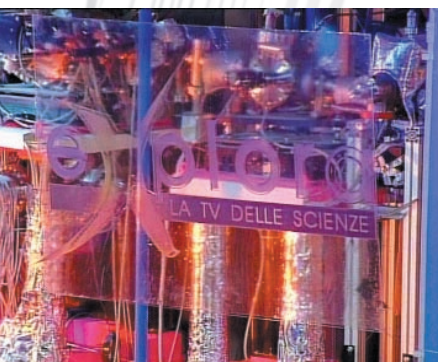


EVENTS

EXPLORA AND OTHERS - SCIENCE TV AT ELETTRA

> G. Paolucci

Sincrotrone Trieste S.C.p.A., S.S. 14 km 163.5, in AREA Science Park, 34012 Trieste, ITALY



Public awareness towards science is becoming an important issue of most scientific institutions. Its relevance is further underlined by the recent promotion of science-society relationships in the European Framework programs.

There are good reasons for the importance of this aspect: on one side education in a broad sense is part of the mission of most research institutions, on the other side people want to be informed of how public money is spent. In particular they want to understand how today's research can influence their lives in order to make up their mind and contribute to the creation of their future. This became evident in the public debates on sustainability, environmental, and ethical issues.

The ELETTRA laboratory is sensitive to these issues and has a long tradition of being open to the general public. Besides our users, more than 4000 visitors come to ELETTRA each year, two third of them being students from upper secondary schools. Also other events, as the annual open days, attract many non-scientific visitors from far and near.

In the last year, ELETTRA has attracted the interest of national and foreign television companies. The Slovenian TV Koper has filmed a series of TV programs on science in our laboratory, which included several interviews with our scientists. The greatest initiative this year has been realized during the week of science organized by the Italian Ministry for Education, University and Research. In that week two issues of the program "Explora - La TV delle scienze" have been filmed in our experimental hall. For this event, the experimental hall was actually transformed into a TV studio, a stage was mounted, and diffuse colorful lights were installed. Extensive noise tests had to be per-

formed before - it is not obvious to make audio recordings in a place as noisy as our experimental hall! A number of scientists working at facilities in Trieste - SISSA, AREA Science Park, the International Center for Genetic Engineering and Biotechnology and ELETTRA - have been interviewed by Luciano Onder, a well known Italian science journalists. Students from the upper secondary school Liceo Scientifico A. Antonelli in Novara attended the debates, where they got the opportunity to ask questions and to discuss with the scientists.

The two issues dealt with themes of the science week: The first one was on recent developments of biomolecular medicine, the second one on the great discoveries in physics during the 20th century was dedicated to the world year of physics 2005. The program is presented in the Italian schools, and we have been informed that the two issues recorded at ELETTRA had quite a good impact on high school students.

RAI EDUCATIONAL, EXPLORA "LA TV DELLE SCIENZE"

TV programs realized within the "15th week of the scientific and technologic culture – MIUR"

**First studio debate:
MOLECULAR MEDICINE**
Debate transmitted on Thursday 17/3/ 2005

Guests in the program:

- **Prof. Giannino Del Sal**
Consorzio Interuniversitario per le Biotecnologie (CIB)
- **Prof. Mauro Giacca**
Centro Internazionale di Ingegneria Genetica e Biotecnologia (ICGEB) - Trieste
- **Dott. Tarcisio Not**
Ospedale Infantile Burlo - Trieste
- **Prof.ssa Maria Cristina Pedicchio**
AREA Science Park - Trieste
- **Ing. Frederic Pérennès**
ELETTRA Laboratorio di Luce di Sincrotrone - Trieste
- Students and teachers from the 4th and 5th classes of the upper secondary school **Liceo Scientifico A. Antonelli in Novara**



FREDERIC PERENNES
Nanotecnologo Sincrotrone ELETTRA

TARCISIO NOT
Pediatra Ospedale Infantile "Burlo" - Trieste



MAURO GIACCA
Direttore ICGEB - Trieste



**RAI EDUCATIONAL, EXPLORA
"LA TV DELLE SCIENZE"**

TV programs realized within the "15th week of the scientific and technologic culture – MIUR"

**Second studio debate:
THE GOLDEN CENTURY OF PHYSICS
Debate transmitted on Friday 18/3/2005**

Guests in the program:

- **Prof. Daniele Amati**

Scuola Internazionale Superiore di Studi Avanzati (SISSA) - Trieste

- **Prof. Stefano Fantoni**

Scuola Internazionale Superiore di Studi Avanzati (SISSA) - Trieste

- **Dott. Gianrossano Giannini**

Università degli Studi di Trieste

- **Dott. Andrea Locatelli**

Laboratorio di Luce di Sincrotrone ELETTRA - Trieste

- **Dott. Giorgio Paolucci**

Laboratorio di Luce di Sincrotrone ELETTRA - Trieste

- Students and teachers from the 4th and 5th classes of the upper secondary school **Liceo Scientifico A. Antonelli in Novara**



PHOTO GALLERY

VISIT OF THE ITALIAN RESEARCH MINISTER LETIZIA MORATTI AT ELETTRA (October, 5th 2004)

Picture 1. Letizia Moratti (Italian Minister of Research) and Riccardo Illy (Governor of the region Friuli Venezia Giulia FVG) arriving at ELETTRA.

Picture 2. Visit to the laboratory. From the left: Giorgio Paolucci, Riccardo Illy (from behind), Carlo Bocchetta, Letizia Moratti, Riccardo Tommasini, Alfonso Franciosi (from behind), Regina Rochow, and Carlo Rizzuto.

Picture 3. Letizia Moratti and Riccardo Illy signing an agreement about the realisation of an area for biomolecular medicine in FVG, the home region of ELETTRA. Between them Luciano Criscuoli (General Director, Italian Research Ministry)

Picture 4. Shakehands after setting the signatures.



1



2



3



4

VISIT OF THE ITALIAN RESEARCH MINISTER LETIZIA MORATTI AT ELETTRA (October, 5th 2004)

Picture 5. Press conference at ELETTRA during the visit.

Picture 6. From the left: Carlo Rizzuto (President of ELETTRA), Roberto Cosolini (Research Councilor of FVG), Riccardo Illy, Letizia Moratti, Guido Possa (Italian Deputy Minister of Research), Roberto Antonione (Under-Secretary of State for External Affairs), Luciano Criscuoli (General Director, Italian Research Ministry), and Maria Cristina Pedicchio (President of AREA Science Park).

Picture 7. Maria Cristina Pedicchio, Letizia Moratti, and Guido Possa during the press conference.

Picture 8. Words of farewell - from left: Carlo Rizzuto, Letizia Moratti, Angelo Baiguera (Chief Press Officer of FVG), Roberto Antonione, Stefano Fantoni (Director of SISSA), and Alfonso Franciosi (Chief Executive Officer of Sincrotrone Trieste SCpA and Director of ELETTRA).



5



6



7



8

ITALIAN-AUSTRALIAN WORKSHOP (February, 9th-11th 2005)

Picture 1. Steve Wilkins (CSIRO Melbourne) during his presentation.

Picture 2. Giancarlo Panaccione (INFN-TASC, APE beamline) during his talk.

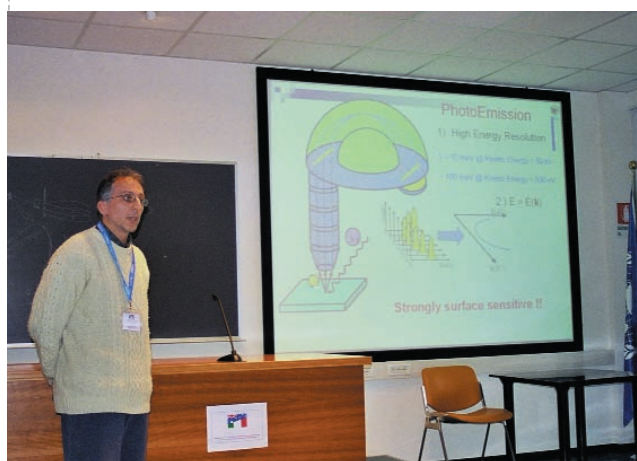
Picture 3. Audience of the Italian-Australian Workshop on Future Directions in Spectroscopy and Imaging with Synchrotron Radiation.

Picture 4. Australians at the Pizzeria Da Furlan, from the left: James Sullivan (ANU Canberra), David Paganin (Monash University Melbourne), Steve Wilkins (CSIRO Melbourne), Alan Buckley (University New South Wales, Sydney), Andrew Peele (La Trobe University, Melbourne), and Mark Ridgway (ANU, Canberra).

Picture 5. Conference Dinner.



1



2



3



4



5

VISIT OF THE EU COMMISSIONER FOR RESEARCH JAN POTOČNIK (April, 8th 2005)

Picture 1. Carlo Rizzuto and Jan Potočnik in the Experimental Hall.

Picture 2. Giorgio Paolucci, Jan Potočnik, and Maria Cristina Pedicchio at the Czech Material Science beamline.

Picture 3. Alfonso Franciosi presents the activities of ELETTRA's Industrial Liason Office to Jan Potočnik.

Picture 4. Carlo Rizzuto outlines goals and contents of the Social Accountability Reporting Project of ELETTRA.



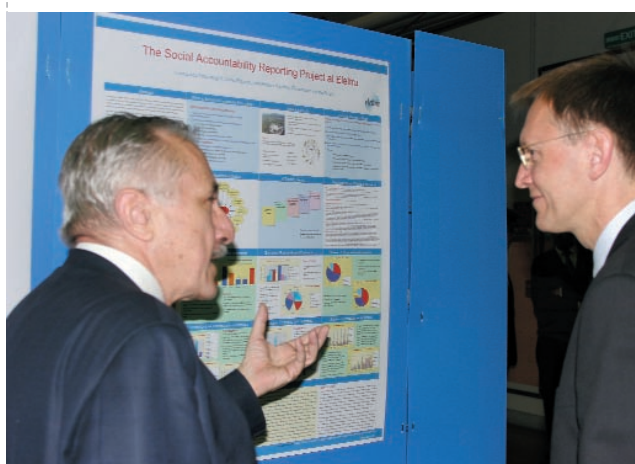
1



2



3



4

VISIT OF THE EU COMMISSIONER FOR RESEARCH JAN POTOČNIK (April, 8th 2005)

Picture 5. Frédéric Pérennès explaining the Deep X-ray Lithography beamline to Jan Potočnik and other visitors.

Picture 6. Jan Potočnik looking at some microstructured material

Picture 7. Jan Potočnik looking at some micromechanic devices manufactured at ELETTRA.

Picture 8. Giorgio Rossi (Director of the INFM-TASC laboratory), Jan Potočnik, Giuseppe Colpani (General Director of AREA Science Park), Carlo Rizzuto, and Maria Cristina Pedicchio on the way from ELETTRA to a visit at the TASC laboratory.



5



6



7



8

THE GRID PROJECT AT ELETTRA (January, 12th 2005 - May, 9th 2005)

Picture 1. Roberto Pugliese (project manager) participating in a video conference. (January, 12th 2005)

Picture 2. Remote injection from DESY (Hamburg) at ELETTRA. (May, 9th 2005)

Picture 3. Participating Institutions in the remote injection: DESY (Ferdinand Willeke on the large screen), ELETTRA (Emanuel Karantzoulis on the upper small screen), and the University of Udine (lower small screen), operator: Lawrence Iviani. (May, 9th 2005)

1



2



3



IAEA AFFILIATION CEREMONY (September, 9th 2005)

Picture 1. Roberto Cosolini (Research Councillor of Region Friuli Venezia Giulia), Maria Cristina Pedicchio (President of AREA Science Park), Werner Burkart (Deputy Director of the International Atomic Energy Agency IAEA), Carlo Rizzuto (President of Sincrotrone Trieste SCpA), Stefano Fantoni (Director of SISSA), and Katepalli R. Sreenivasan (Director of the Abdus Salam International Centre for Theoretical Physics) during the press conference on September 9th, 2005.

Picture 2. Unveiling of the Affiliation Plate by Carlo Rizzuto, Maria Cristina Pedicchio, and Werner Burkart.

Picture 3. The Affiliation Plate at the entrance of the laboratory's main building presenting ELETTRA as a collaborating centre.

Picture 4. Shakehands.



1



2



3



4

ACCELERATOR PHYSICS COURSE - CERN ACCELERATOR SCHOOL & ELETTRA (October, 2nd - 14th 2005)

Picture 1. Opening Lecture by Prof. Sreenivasan, Director of the ICTP

Picture 2. Audience

Picture 3. Lecture by Oliver Bruning from CERN

Picture 4. Visit to the vaults and wine tasting



1



2



3



4

ACCELERATOR PHYSICS COURSE - CERN ACCELERATOR SCHOOL & ELETTRA (October, 2nd - 14th 2005)

Picture 5. Dinner at Milic

Picture 6. Music at Dinner

Picture 7. Dessert

Picture 8. Participants



5



6



7



8

AREA Science Park

A WORLD FOR RESEARCH AND INNOVATION

Situated on the Carso plateau which surrounds Trieste, **AREA Science Park**, one of the leading multi-sector science and technology parks in Europe, is a system that integrates **research and business**. Its valued services, the relations with the main universities and scientific institutions and its dense network of international contacts make AREA the ideal location for companies open to **innovation**.

More than 80 organisations, including private companies and internationally renowned research institutes, have chosen to settle in AREA Science Park to enhance their competitiveness. Alongside basic research in physics, material structures, genomics and biotechnology, there is an ever-broadening range of research aimed at applications in the chemical, pharmaceutical, food, electronics and ICT industries. **Excellence** is the AREA key-word: mostly in Molecular Biomedicine and the relevant Technology District, in technology transfer and hi-level education.

In the strategies of AREA a central role is dedicated to enhance the attractiveness of the Friuli Venezia Giulia Region for foreign direct investment in research, innovation and hi-tech industry as well as to create new technology poles in the Region and to diffuse innovation by means of a network of competence centres. **Internationalization** is in the AREA's business card: fostering the international collaboration in science and technology and promoting the globalization of the regional hi-tech companies are a key issue in the AREA's strategies.

Employing over 1,600 people, boasting on experience of over fifteen years and enjoying uninterrupted growth since its foundation, AREA qualifies as a stimulating powerhouse of ideas and expertise where scientists of different cultures and nationalities work in synergy with enterprises and with financial, economic and business organisations.



AREA
SciencePark



AREA Science Park
Marketing and International Relations
Padriciano 99, 34012 Trieste - Italy
Phone (39) 040 375 5216
Fax (39) 040 226698
www.area.trieste.it
area.sviluppo@area.trieste.it

www.area.trieste.it



Sincrotrone Trieste S.C.p.A.
S.S. 14 Km. 163.5 in AREA Science Park
34012 Trieste ITALY
www.elettra.trieste.it - info@elettra.trieste.it

